공학박사 학위논문

Plastic Deformation Behavior of Magnesium Single Crystals

마그네슘 단결정의 소성변형거동에 대한 연구

2013년 02월

서울대학교 대학원

재료공학부

边 明 哲

Plastic Deformation Behavior of Magnesium Single Crystals

지도 교수 신 광 선

이 논문을 공학박사 학위논문으로 제출함

2013년 02월

서울대학교 대학원

재료공학부

边 明 哲

边 明 哲의 박사 학위논문을 인준함

2013년 02월

위 원 장	김 영 운	(인)
부위원장	신 광 선	(인)
위 원	한 흥 남	(인)
위 원	최 시 훈	(인)
위 원	이 경 훈	(인)

Abstract

Plastic Deformation Behavior of Magnesium Single Crystals

Ming Zhe Bian

School of Materials Science and Engineering

The Graduate School

Seoul National University

Magnesium (Mg) alloys, having a density of about 1.74 g/cm^3, are the lightest structure materials and their superior physical and mechanical properties make Mg alloys extremely attractive for applications requiring light-weight materials. Especially, in the automotive industry, magnesium alloys have become the key materials for increasing the fuel efficiency due to their low density, excellent specific strength and stiffness, exceptional dimensional stability, high damping capacity, and high recycle ability. Magnesium alloys can be divided into cast magnesium alloys and wrought magnesium ones in terms of difference in processing. At present, the casting magnesium alloys are utilized to produce the majority of magnesium alloy products. However, the cast magnesium alloys fail to meet most of the requirements and the wrought Mg alloys show both better strength and toughness. Unfortunately, there are several fundamental and technical issues preventing the development of high performance of wrought Mg alloys. For example, Mg alloys usually develop strong basal texture during rolling, resulting in anisotropic mechanical properties and poor formability. Additionally, fundamental observations such as temperature and orientation

dependency on the slip and twinning modes, as well as interactions between deformation modes are still rarely reported.

The first objective of this study is to determine the critical resolved shear stress (CRSS) values for various major slip and twin systems, by preparing single crystal specimens with different orientations and deformed at various temperatures. The deformed samples were systematically examined by optical microscopy and electron microscopy. The single slip oriented specimens were used to directly derive the CRSS values for the corresponding deformation modes by using Schmid factor (SF) criterion. Viscoplastic self-consistent (VPSC) simulations were utilized to obtain the best fitted CRSS and hardening parameters for various deformation modes when more than one deformation mode was involved due to the loading direction of the single crystal specimens. From experimental and simulated results, it was found that the CRSS for basal <a> slip and $\{10\bar{1}2\}$ twin showed a weak temperature dependence, whereas the CRSS for prismatic <a>, <c+a> slip and $\{10\bar{1}1\}$ twin exhibited a strong temperature dependence. The resolved shear stresses that activate the prismatic <a>, <c+a> slip and $\{10\bar{1}1\}$ twin modes are much greater than those required to initiate the basal <a> slip and $\{10\bar{1}2\}$ twin in magnesium at room temperature. Therefore, the predominant deformation modes of magnesium at room temperature are the basal slip and $\{10\bar{1}2\}$ twin. It was generally known that the $\{10\bar{1}2\}$ twin strongly affects plastic deformation of the Mg alloys since twining can accommodate the c-axis strain, but large strains require additional deformation by slip. The interactions between dislocations and twin boundaries are, therefore matters of practical interest because the deformation-induced twins may play as barriers to further slip, the source of the slip, and twin dislocations at the twin boundaries. The second objective of this study is investigate systematically the effects of the $\{10\bar{1}2\}$ twin on the deformation and the recrystallization behavior of

magnesium single crystals.

To date, there are so many works that have been carried out to modify the strong basal texture, which means spreading the basal planes from the sheets normal direction. However, there is still a lack of understanding of what kind of textures are desired textures because systematic research regarding the effects of the initial orientation on the mechanical behaviors has been rarely reported. The third objective of this study is to characterize the initial orientation effects on the deformation behavior of magnesium single crystals. The results show relative activity of slip and twinning modes changed dramatically due to different orientations. The <c+a> slip plays a dominant roles in the 0° rotated specimen. Basal slip is a main deformation mode in the range of 10 to 60° and the $\{10\bar{1}2\}$ twin mode dominates from 70 to 90° in the rotated samples from the C-axis.

The second objective of this study is to examine the limited interactions between the basal slip and $\{10\bar{1}2\}$ twin. In this study, the effects of $\{10\bar{1}2\}$ twin on various slip and twinning behavior were observed in a systematic manner. The Mg single crystals with various crystallographic orientations from [0001] and $[10\bar{1}0]$ were prepared for two-step compression (TSC) tests. It was found that $\{10\bar{1}2\}$ twin has limited hardening effects on yield strength for the 0° rotated specimen owing to a high CRSS value for the <c+a> slip. In case of 10 ~ 60° specimens, the incorporation of basal dislocation into a $\{10\bar{1}2\}$ twin reveals that basal dislocations in the matrix cross-slip onto the basal plane in the twinned crystal. The percentage increase of yield strength for the 70 ~ 90° rotated specimens is relatively higher than other specimens because the Hall-Petch slop for the twinning-dominated flow is frequently greater than that for the slip-dominated flow.

Keywords:
Student Number: 2006-23703

Contents

List of Tables

List of Figures

Chapter 1. Introduction

Die-casting magnesium (Mg) alloys are fulfilling the essential demands for electronic and automobile parts due to a high damping capacity and excellent machinability. However, structural applications normally require energy absorption materials with reasonable ductility, high yield strength and corrosion resistance. In recent years, significant efforts have been made to develop new Mg alloys for high strength and high temperature applications, as well as advanced manufacturing processes for reliable mechanical properties and corrosion resistance. The cast magnesium alloys fail to meet most of these requirements and the wrought Mg alloys show both better strength and ductility.

General properties in the wrought Mg and its alloy polycrystalline aggregates have a more sharply developed texture, which underlies strong anisotropy in mechanical behavior. The limited ductility can be traced back to a lack of the independent slip modes [1]. In order to overcome the weakness of Mg as a structure material, alloy elements are inevitably added to the Mg matrix to increase the strength and ductility [2]. Compositions predominantly based upon mixtures of aluminum, zinc, tin, and rare earths (RE) are used as alloying additions, together with the now environmentally unattractive elements cadmium and thorium. The alloy additions can be divided into three categories: (1) Elements that can improve both strength and ductility of Mg alloys. Ranging in increasing strength: Al, Zn, Ca, Ag, Ce, Ni, Cu, Th. Ranging in increasing ductility: Th, Zn, Ag, Ce, Ca, Al, Ni, Cu. (2) Elements that can only improve the ductility, but with little effect on the strength of the Mg alloys. Ranging in increasing ductility: Cd, Tl, and Li. (3) Elements that

decrease the ductility but increase the strength of the Mg alloys. In increasing strength: Sn, Pb, Bi, and Sb [3].

Recently the RE elements have been shown to have a wide range of benefits for the Mg alloys, ranging from grain refinement in wrought processed Mg alloys to improved high temperature strength and creep resistance, improved corrosion resistance, and weakening texture. The yield strength of RE-containing alloys can exceed 600 MPa when they are produced by rapid solidification processing, and very recently, an impressive value of over than 400 MPa has been obtained for the yield strength in an Mg–Gd alloy produced by conventional process [4-6]. From these alloy developments, the new technology that can control the texture and mechanical properties of magnesium alloy can be seen.

1.1 Independent slip modes in hexagonal close-packed structures and Mg crystals

The deformation mechanism of the hexagonal close-packed materials are more complicated and less understood than those of face-centered cubic and body-centered cubic materials. The primitive hexagonal unit-cell has 3 axes (a1=a2≠c) with corresponding angles ($\alpha = \beta = 90^o, \gamma = 120^o$). If atoms are assumed to be hard spheres, the hexagonal close-packed structures are usually described in terms of stacking of close-packed triangular lattice layers with ABABAB and the ideal axial ratio is $\gamma = {}^{c}/_{a} = \sqrt{{}^{8}/_{3}} = 1.633$. No pure metal has this ideal c/a ratio, although cobalt and Mg are close to this value [7]. Detailed information about lattice parameters, preferred slip mode

and ductility is given in Table 1.1. If the c/a ratio is less than $\sqrt{3}$, then the prismatic plane is more densely packed than the basal plane. According to the Peierls-Nabarro equation, a change in slip plane from (0001) to $\{10\bar{1}0\}$ may take place [8]. However, this assumption only accounts for titanium and zirconium; it fails to explain the predominance of basal slip in Mg, cobalt, and beryllium.

Figure 1.1 illustrated theoretically possible slip modes in Mg and Mg alloys. Table 1.2 shows detailed information about vector energies for the possible dislocation types. The basal slip was observed to be the prevalent deformation mode as it was found to be uniformly distributed all over the crystal surface in case of Mg single crystal. Traces of slip on the prismatic planes have been observed only in parts of the grain which may have been subjected to higher stresses such as near corners [9]. Since the basal slip has the lowest CRSS value, some works have performed tensile tests with a basal plane parallel with the loading direction. This orientation is favorable for the non-basal slip and suppressed the basal slip based upon geometric conditions. The results showed the prismatic <a> glide to be the deformation mode at room temperature in these conditions with [10-11]. Plastic deformation characteristics of Mg and Mg-Li single crystals deformed in the hard orientation were reported by Stohr and Poirier, Obara, and Ando et al. [12-14]. The information obtained from these investigations was the stress–strain curves, slip-trace and slip-step height analyses on the surface, and post-mortem transmission electron microscopy (TEM) characterization of dislocation structures. A possible source mechanism for the non-basal <c+a> slip dislocations is proposed by Yoo based on the formation of an attractive junction between glissile <a> and sessile <c> dislocations from the prismatic plane into a pyramidal plane [15].

Table 1.1 Physical properties of HCP metals [1, 7].

Metal	Be	Ti	Zr	Mg	Co	Zn	Cd
a (nm)	0.229	0.295	0.323	0.321	0.251	0.266	0.298
c (nm)	0.359	0.468	0.515	0.521	0.409	0.494	0.562
c/a ratio	1.568	1.587	1.593	1.623	1.628	1.856	1.886
Preferred slip	basal	prism	prism	basal	basal	basal	basal
Ductility	Poor	Good	Good	Fair	Fair	Poor	Fair

There must be other deformation mechanisms present to fulfill the von-Mises compatibility criterion for the fine grained Mg alloys that exhibit a high ductility. Since the basal slip and twinning are considered to be insufficient, due to their limited contributions to the deformation, prismatic slip with <c+a> type Burgers vectors has been repeatedly employed to explain the observed high ductility. Koike reported that grain refinement is effective for the activation of prismatic slip at grain boundary, because grain refinement promotes stress concentration at grain boundary, resulting in activation of prismatic slip, as shown in Fig. 1.2 (a). Detailed analysis in his research shows that dislocation cross-slip to non-basal planes. Additionally, it reported that the activity of non-basal dislocation slip systems and the dynamic recovery were considered to be responsible for the large tensile ductility in the ECAE-processed AZ31 magnesium alloys, as shown in Fig. 1.2 (b).

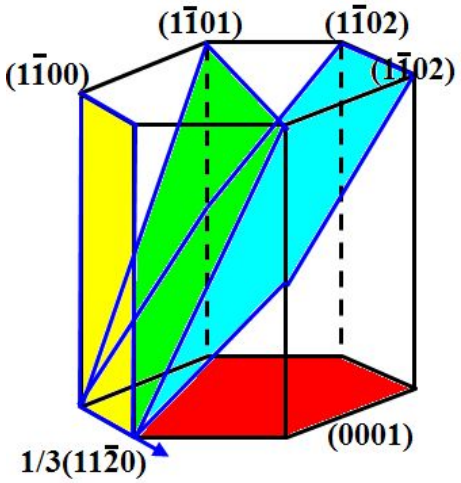

(a)

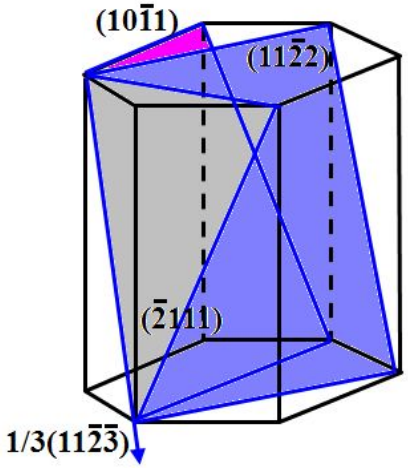

(b)

Figure 1.1 Theoretically possible slip modes in magnesium, colored surfaces represent each slip planes, arrows represent slip direction Burgers vectors. (a) <a> type slip systems, (b) <c+a> type slip systems.

Table 1.2 Vector energies for the possible dislocation types in Mg metals.

Type of dislocations	Number of systems	Burgers vector	Magnitude of Burgers vector	Slip system	
a	3 (2)	1/3<11$\bar{2}$0>	$\|a\| = 3.209$	Basal	{0001}<11$\bar{2}$0>
	3 (2)			Prism-I	{10$\bar{1}$0}<11$\bar{2}$0>
	6 (4)			Pyramidal-I	{10$\bar{1}$1}<11$\bar{2}$0>
c	3 (2)	<0001>	$\|c\| = 5.211$	Prism-I	{10$\bar{1}$0}<0001>
	3 (2)			Prism-II	{11$\bar{2}$0}<0001>
c+a	3 (2)	1/3<11$\bar{2}$3>	$\{\|a\|^2 + \|c\|^2\}^{1/2} = 6.120$	Pyramidal-II	{11$\bar{2}$2}<11$\bar{2}$3>

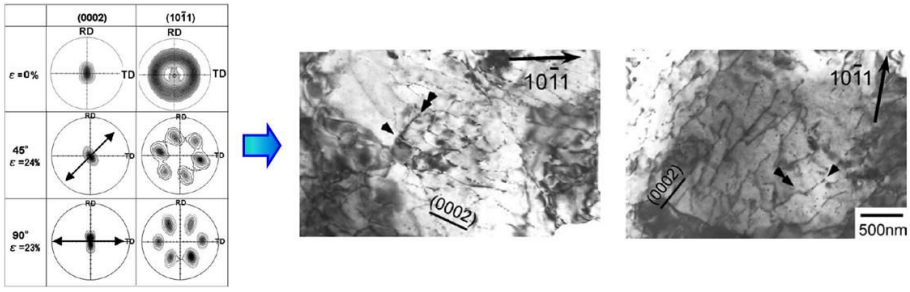

(a)

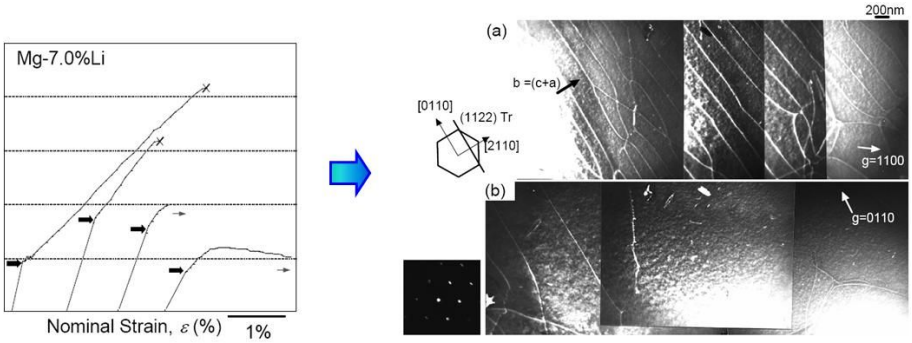

(b)

Figure 1.2 (a) Prismatic slip dislocation observations in the fine grained AZ61 rolled sheets [16] (b) <c+a> slip observations in Mg-Li single crystals [17].

1.2 Twinning in HCP metals and Mg crystals

In the classical theory of deformation twinning, the original lattice is reoriented by atom displacements, which are equivalent to a simple shear of the lattice points. An important difference between twinning and slip deformation is that twinning is polarized. In HCP metals, twinning (on pyramidal planes of different orders and modes) is usually employed to explain deformation with c components. The invariant plane of this shear is called K_1 and the shear direction η_1; the second undistorted plane is K_2, the plane containing η_1 and the normal to K_1 and K_2 is the plane of shear. The crystallographic elements, K_1, K_2, η_1 and η_2, the four compound twin systems are well established [18]. Figure 1.3 shows Yoo's plot of twinning shear s vs c/a ratio for six possible twin modes. For primary twin modes, a twin mode showing a positive slope represents contraction along the c-axis, and other showing a negative slope represents extension [1].

The basic symmetry of Mg and Mg alloys has the effect of limited number of independent slip systems. A minimum of five independent slip modes are required for an arbitrary shape change, and giving rise to twinning modes play important deformation mechanism. Thus in plastic deformation, slip and twinning are competitive and interdependent deformation modes at low temperature. Several types of twin modes were reported in Mg single crystals including the $\{10\bar{1}1\}$, $\{10\bar{1}2\}$, $\{10\bar{1}3\}$, $\{10\bar{1}5\}$, $\{30\bar{3}2\}$, and $\{30\bar{3}4\}$ type [19-20]. Double twinning of the $\{10\bar{1}1\}$-$\{10\bar{1}2\}$, $\{10\bar{1}2\}$-$\{10\bar{1}2\}$ and $\{10\bar{1}3\}$-$\{10\bar{1}2\}$ types were found to be a particular feature of twins with $\{10\bar{1}2\}$ re-twinning in the primary twin interior and the preferential alignment of primary twins [21-22]. Table 1.3 lists detailed information about

misorientation between the matrix and the corresponding twin types. Among them, the $\{10\bar{1}2\}$ twin and $\{10\bar{1}1\}$ twin have been far the most observed twinning mode in Mg metals. A unit cell with the base vectors η_1 and η_2 are shown in Figure 1.4 for the $\{10\bar{1}2\}$ tensile and $\{10\bar{1}1\}$ compression twin modes. d is the interspacing of the twin habit planes K_1, $\emptyset$ is the acute angle between η_1 and η_2, e is a numerical factors, and q is the number of K_1 lattice planes intersected by η_2. It was reported that the $\{10\bar{1}2\}$ tensile twining requires only 2 to 3 MPa, while the $\{10\bar{1}1\}$ compressive twin requires 70 to 140 MPa [23]. Reed–Hill and Robertson reported the onset of twinning at a tensile stress of 4 MPa, which corresponds to the resolved shear stress of 2 MPa, i.e. reversal of the η_1 direction will not produce a twin [24]. This means that for a single crystal of given orientation with respect to a uni-axially applied stress, some variants of particular twin mode should operate only in tension, whereas others should operate only in compression. It is generally known that the $\{10\bar{1}2\}$ twin is most commonly observed in Mg alloys and relatively easily activated by compression direction perpendicular to, or tension parallel to the c-axis from the geometric reason (Figure 1.5) [25]. In the opposite case, when contraction along the c-axis is accommodated by the formation of contraction twins on the $\{10\bar{1}1\}$ planes, the basal planes are reoriented by 56^o around a $<11\bar{2}0>$ axis. The origin of the small CRSS for the twins is not clear at the moment. The lenticular shape of twins is generally attributed to a twinning shear strain. However, the twinning shear strain is nearly the same for both $\{10\bar{1}1\}$ and $\{10\bar{1}2\}$ twins. Twins are generated when compressed along the c-axis and frequently appear in complex twinning modes.

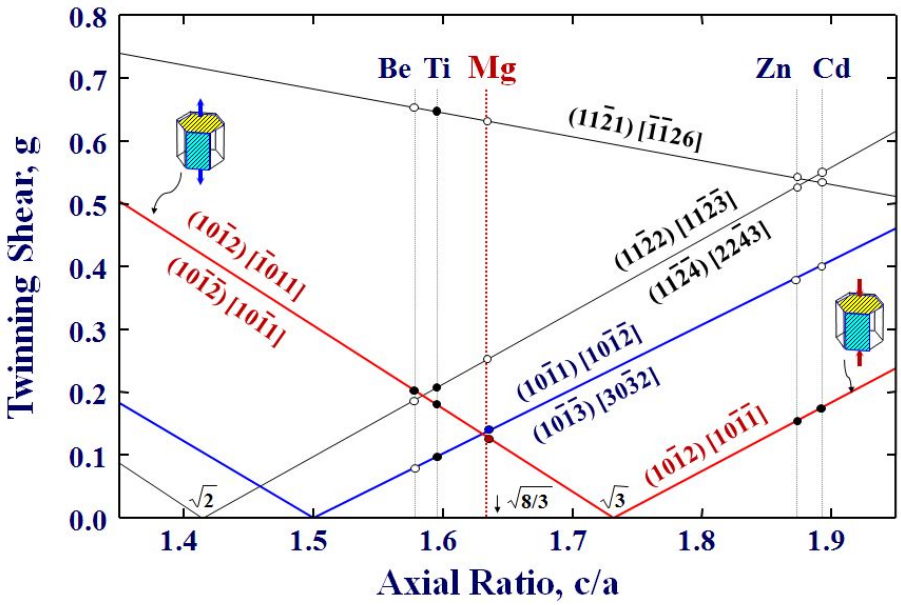

Figure 1.3 Variation of twinning shear with the axial ratio for the hexagonal metals. A filled symbol indicates that the twin mode is an active mode [1].

Table 1.3 Twin type and corresponding misorientation angle in Mg crystal.

Type of Twin	Misorientation Angles/Axis
$10\bar{1}1\}$	56.2^{o} $<1\bar{2}10>$
$\{10\bar{1}2\}$	86.3^{o} $<1\bar{2}10>$
$\{10\bar{1}3\}$	64^{o} $<1\bar{2}10>$
$\{10\bar{1}5\}$	41^{o} $<1\bar{2}10>$
$\{30\bar{3}2\}$	39.2^{o} $<1\bar{2}10>$
$\{30\bar{3}4\}$	70.8^{o} $<1\bar{2}10>$
$\{10\bar{1}1\}$-$\{10\bar{1}2\}$	37.5^{o} $<1\bar{2}10>$
$\{10\bar{1}1\}$-$\{10\bar{1}2\}$	30.1^{o} $<1\bar{2}10>$
$\{10\bar{1}1\}$-$\{10\bar{1}2\}$	66.5^{o} $<5\bar{9}43>$
$\{10\bar{1}1\}$-$\{10\bar{1}2\}$	69.9^{o} $<2\bar{4}21>$
$\{10\bar{1}2\}$-$\{10\bar{1}2\}$	7.4^{o} $<1\bar{2}10>$
$\{10\bar{1}2\}$-$\{10\bar{1}2\}$	60^{o} $<10\bar{1}0>$[a]
$\{10\bar{1}2\}$-$\{10\bar{1}2\}$	60.4^{o} $<\bar{8}170>$[b]
$\{10\bar{1}3\}$-$\{10\bar{1}2\}$	22.2^{o} $<1\bar{2}10>$

[a]Actual axis is 3.7^{o} off $<10\bar{1}0>$

[b]Actual axis is 3.7^{o} off $<\bar{8}170>$

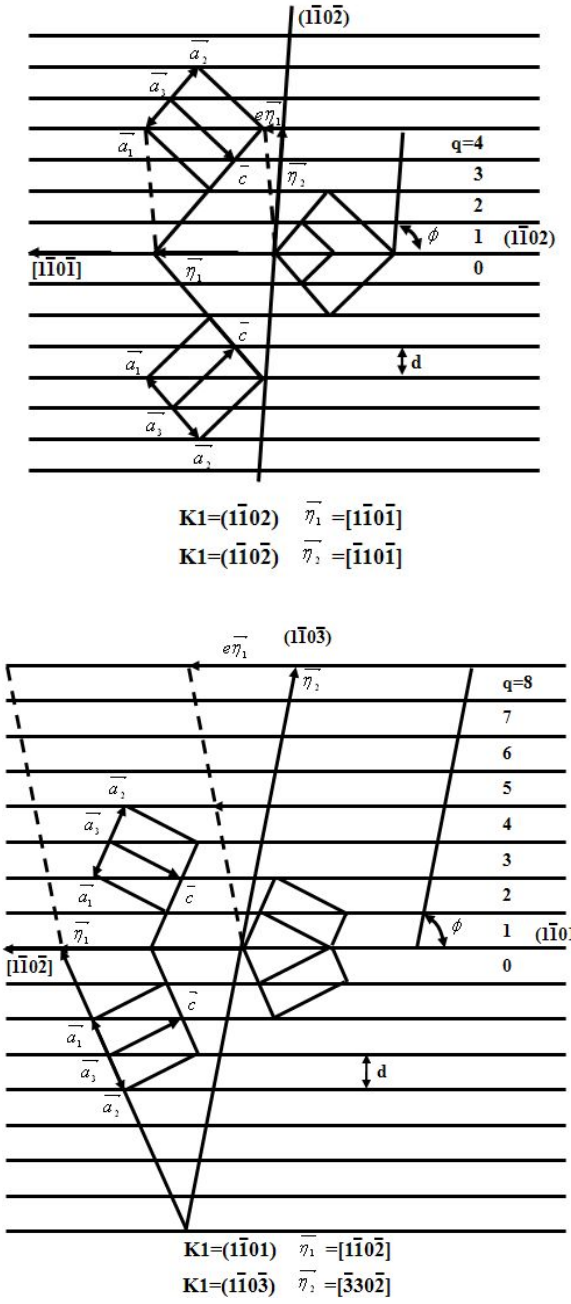

Figure 1.4 Crystallographic relations of (a) {10$\bar{1}$2} tensile and (b) {10$\bar{1}$1} compression twin modes.

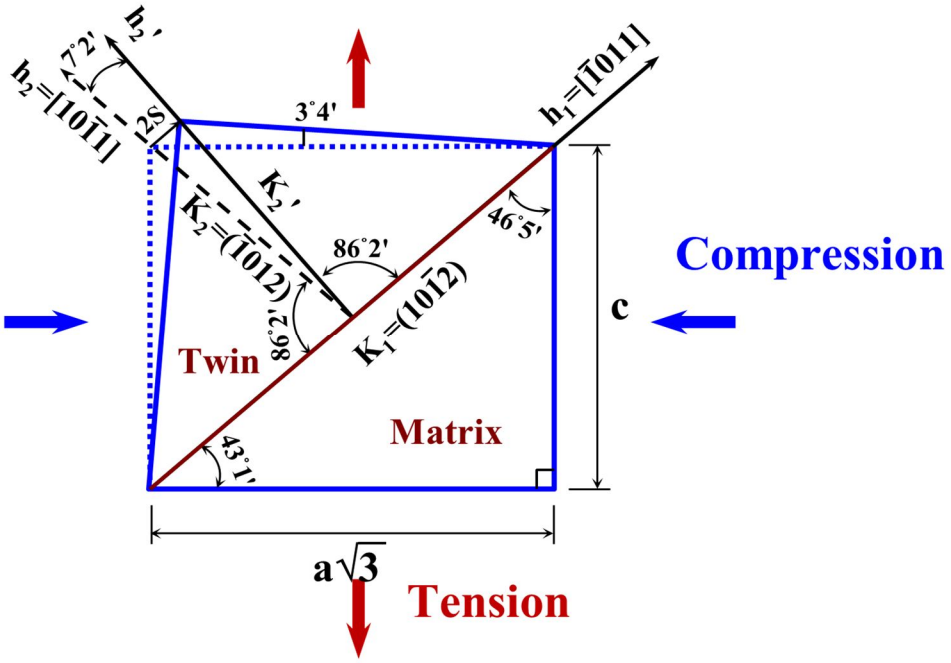

Figure 1.5 Shape changes produced by the $\{10\bar{1}2\}$ twin in Mg crystal [7].

1.3 Twinning on deformation behavior of Mg alloys

It has recently been reported that the $\{10\bar{1}2\}$ twinning plays an important role in the deformation of wrought Mg alloys: (1) texture evolutions by 86.3^{o} reorientation; (2) accommodation of plastic strain, causing a low flow stress and strain hardening rate; (3) twin induced recrystallization. These facts suggest that a change in twinning characteristics, caused by plastic deformation, would have a significant effect on the deformation behavior of wrought materials and the production process of final products.

Recently some works focus on the influence of deformation twinning on texture and microstructure evolution. Brown et al. used an in-situ neutron diffraction technique to reveal the texture evolution induced by deformation twinning [26]. Jiang et al. chose different strain paths and different temperatures to study the deformation twinning behaviors [27]. Later, they further studied the evolution of $\{10\bar{1}2\}<10\bar{1}1>$ twinning during the uni-axial compression tests, and found that certain twinning events coincided with specific stages of the flow curve [22]. Ma et al. presented EBSD inverse pole figure (IPF) maps of ED samples before deformation and at ε=-0.036 and ε=-0.088 true plastic strain, respectively by using prismatic textures in an AM30 magnesium alloy [28]. It has been reported that the intense basal texture of wrought Mg alloys can be weakened or tilted through the addition of rare earth and calcium elements [29]. Various process methods such as cold rolling, equal channel angular extrusion, asymmetric rolling and differential speed rolling could also be utilized to change the harmful basal texture [30-32].

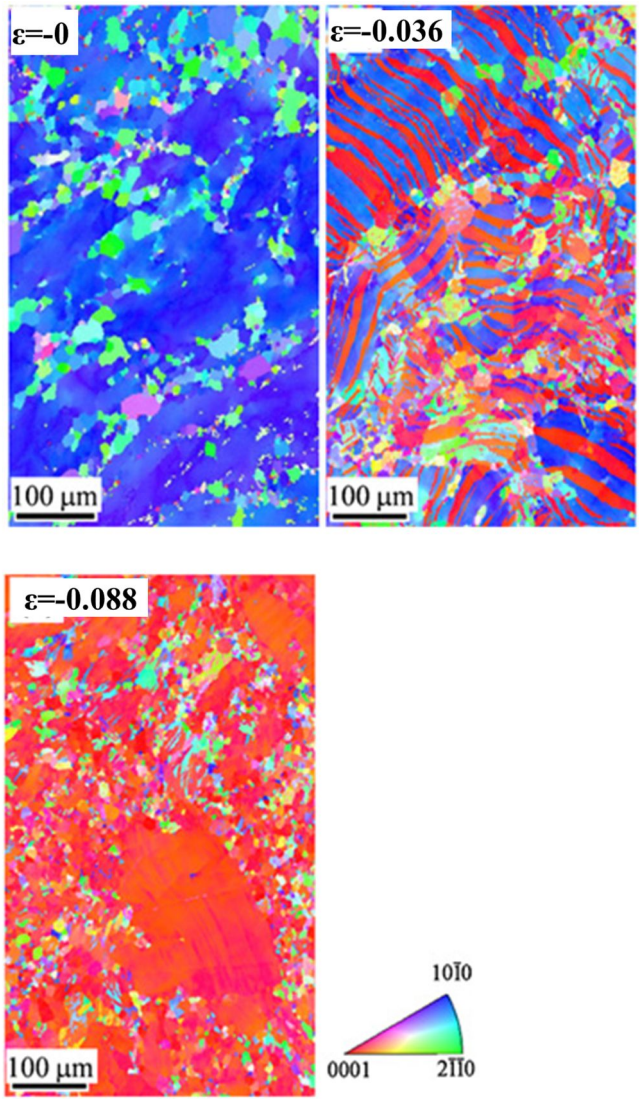

Figure 1.6 Texture evolutions by compression tests, $\varepsilon = 0$, $\varepsilon = -0.036$ and $\varepsilon = -0.088$, showing $\{10\bar{1}2\}\langle 10\bar{1}\bar{1}\rangle$ twin development [28].

For wrought Mg alloys with this changed texture, it is possible for the $\{10\bar{1}2\}$ twinning to occur by tension parallel to the c-axis. The twin morphologies developed under both activation modes and their evolution characteristics with increasing plastic strain would be different because the active twin variants are different, and they will finally have a significantly different effect on the texture evolution and deformation behavior [33]. As mentioned before, profuse twinning in the first 6–8% strain in textured polycrystals has relatively high strengthening effects due to the large volume fraction of grains undergoing twinning. Twin boundaries may act as obstacles to slip and it is generally accepted that twinning reduces effective grain size. Thus, twinning can be expected to strengthen the material by a quasi Hall–Petch effect [34]. For a Cu–8%Al alloy, Basinski et al. proposed that twinning shear converts close-packed planes into {100} type of planes, rendering part of the glissile dislocation population sessile [35]. Other crystallographic effects of twinning affecting different amounts of the dislocation population include increased length of Burgers vectors and decreased dislocation mobility. Hence, twinned crystals are expected to be harder for subsequent slip, adding to the hardening caused by grain segmentation. Typical stress–strain curves along both loading directions exhibited a downwards concave shape in the early stage of deformation, which is known to be a typical feature of the twinning-dominated flow curve, as seen in Figure 1.7. A strain hardening rate rapidly increased around 4% for the RD, but increased gradually for the ND. These differences in deformation characteristics appear to result from the differences in the $\{10\bar{1}2\}$ twinning characteristics, which are dependent on the strain path.

Recently, the DRX behavior in twin, such as $\{10\bar{1}2\}$ tension twin, $\{10\bar{1}1\}$ and $\{10\bar{1}3\}$ compression and double twin has been analyzed in Mg

and Mg alloys. Al-Samman et al. worked to gain information on the orientation of the recrystallized areas in a twin with respect to the neighboring twins and the parent grains by a detailed EBSD analysis [37]. A sample area with recrystallized twins is shown in Figure 1.8 (a). The twin boundaries revealed 86^{o} $<11\bar{2}0>$ misorientation relationship with the matrix and therefore, were identified as $\{10\bar{1}2\}$ tension twin which showed no DRX were free of low angle boundaries. The reason that they did not undergo recrystallization is still unknown. He suggested that the twin was unfavorably oriented for deformation so that no dislocation structure was formed. The presence of some low angle boundaries in the recrystallized twin ($\{10\bar{1}1\}$ twin) structure is apparently due to the dynamics of the process, that is low angle boundaries are first formed inside the twin and with progressing deformation they increasingly incorporate dislocations and eventually convert to high angle boundaries. He described that this will fragment the original twin and creates a new structure of fine grains and also neighboring twins. Li et al. described that the dominant recrystallization nucleation site of hexagonal magnesium is compression twins or the shear bands evolved from them in AZ31 Mg alloy during static recrystallization, as shown in Figure 1.8 (b) [38]. Xu et al. also reported that CDRXed grains in original grains are formed firstly by formation of twin-walled grains divided by mutual intersection of the deformation twins or formation of $\{10\bar{1}1\}$-$\{10\bar{1}2\}$ double twins and then by the in situ evolution of the sub-grains with the growth of low-angle boundaries in double twins to high-angle grain boundaries with increasing compressive strain [39]. Therefore, $\{10\bar{1}1\}$ twin and $\{10\bar{1}1\}$-$\{10\bar{1}2\}$ double twin provide the effective nucleation sites for the DRX during hot deformation, but the $\{10\bar{1}2\}$ tension twin in magnesium alloys may not provide the effective nucleation sites.

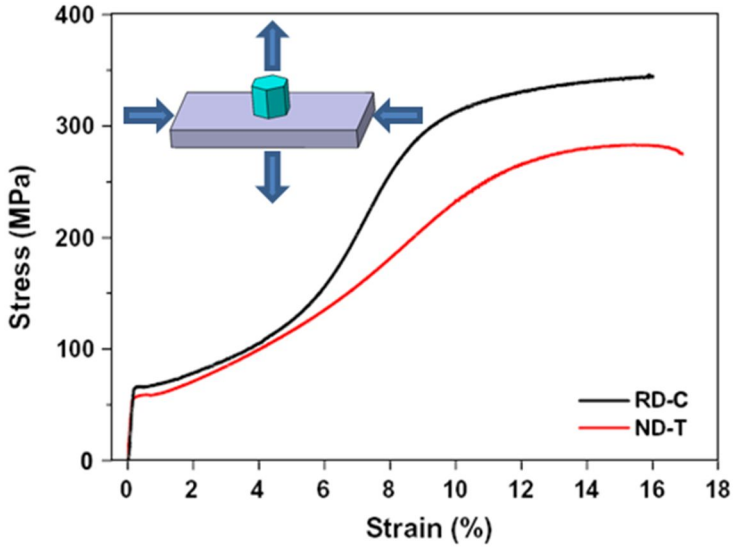

(a)

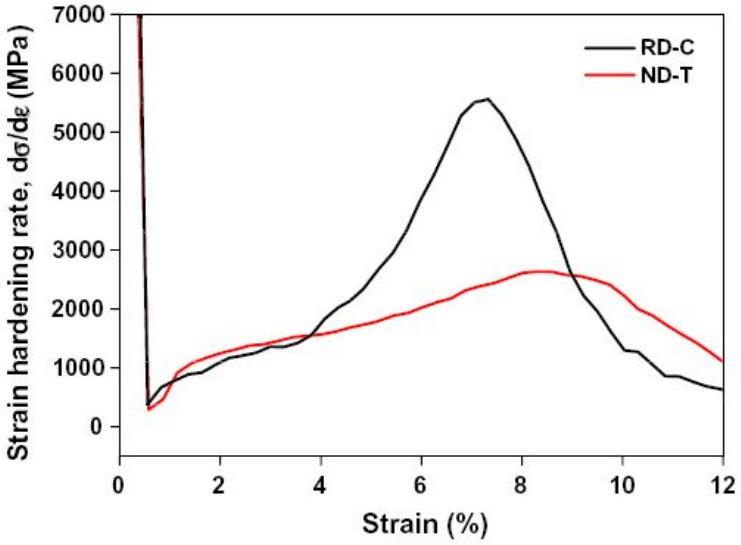

(b)

Figure 1.7 Deformation characteristics of compressed along the RD and stretched along ND: (a) stress–strain curve and (b) strain hardening rate [37].

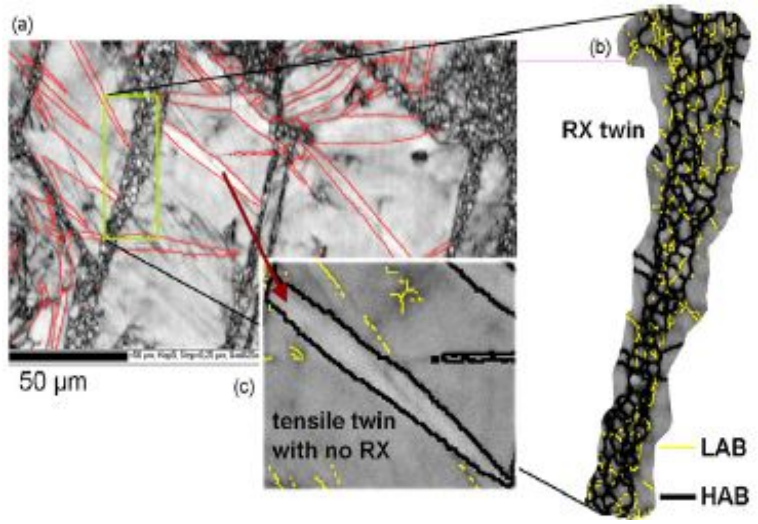

(a)

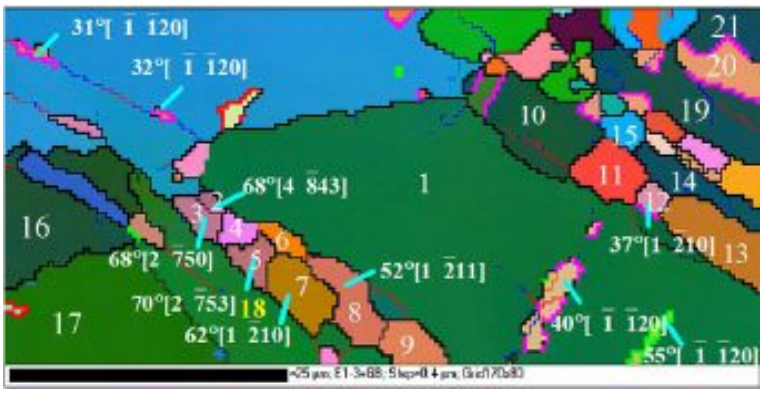

(b)

Figure 1.8 (a) EBSD-Kikuchi band contrast map revealing recrystallized twins and $\{10\bar{1}2\}$ tensile twins [37]; (b) Orientation map of the nucleation at compression twins, 12% cold rolled and annealed at 350 ^{o}C for 1 s [38].

1.4 Stacking faults energies

The theoretically possible Burgers vectors in HCP metals can be represented by means of a double tetrahedron, which is derived from the Thompson tetrahedron for FCC metals in Figure 1.9. There are various types of perfect dislocations and partial dislocation. Detailed examples of the dislocation Burgers vectors are listed in Table 1.4, with the conventional Miller-Bravais notation [40]. The partials lie in the basal plane; their glide on the basal plane produces the shears. In the basal plane, perfect dislocations of the type AB can dissociate into two Shockley partials bounding an intrinsic fault. There are two kinds of intrinsic fault, I_1 and I_2, and one extrinsic fault E and twin like T_2 fault in HCP structures;

I_1: ABABABCBCBCB…

The intrinsic fault I_1 in the structure can be formed by removing an A plane above the B plane, and then shearing the remaining planes above the B plane by the displacement $1/3[1\bar{1}00]$. Similarly, the intrinsic fault I_2, or deformation fault, can be formed by directly shearing the lattice by the displacement $1=3[1\bar{1}00]$

I_2: ABABABCACACA…

The intrinsic fault I_2 can be formed by directly shearing the lattice by the displacement $1/3[1\bar{1}00]$

The extrinsic stacking fault E is generated by inserting an extra C plane into the stacking

E: ABABABCABABAB

The extrinsic fault E is generated by inserting an extra C plane into the stacking

T_2: ABABABCBABAB…

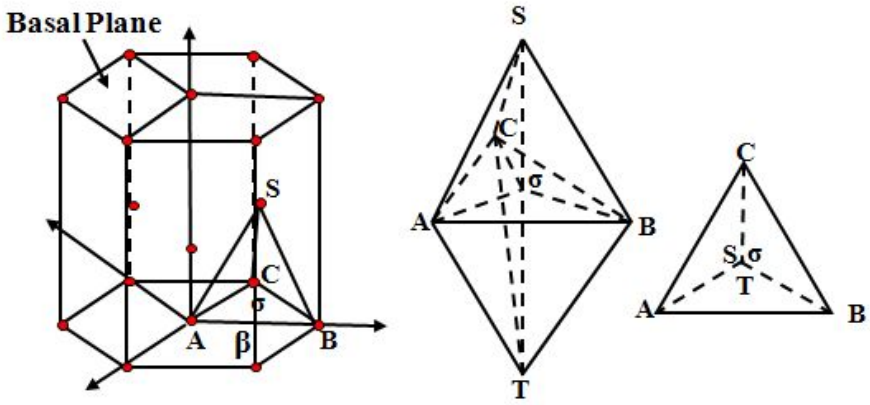

Figure 1.9 Theoretically possible Burgers vectors in the HCP lattice [7].

Table 1.4 Perfect and partial dislocations in HCP metals [40]

Burgers vector or glide plane	Standard Miller-Bravais notation
Perfect-dislocation Burgers vector	$\frac{1}{3}[\bar{1}2\bar{1}0]$
	$[0001]$
	$\frac{1}{3}[\bar{1}\bar{1}23]$
Glissile partials (Shockley partial)	$\frac{1}{3}[\bar{1}100]$
	$\frac{2}{3}[\bar{1}100]$
Sessile partials (Frank partial)	$\frac{1}{2}[0001]$
	$\frac{1}{3}[\bar{2}203]$
	$\frac{1}{6}[\bar{2}023]$
	$\frac{1}{3}[\bar{1}103]$
Partials on $[\bar{1}100]$	$\frac{1}{18}[42\bar{6}3]$
Glide planes	(0001)
	$(\bar{1}100)$
	$(\bar{1}101)$
	$(11\bar{2}2)$

The T_2 fault is a competing low energy defect structure and is twin like since it has mirror symmetry about the faulted plane

In terms of the ψ_i notation, the fault energies are

$$\gamma_{I1} = \sum_{N=1}^{\infty} N\psi_{2N} = \psi_2 + 2\psi_4 + \ldots$$

$$\gamma_{I2} = \sum_{N=1}^{\infty} (2N\psi_{2N} + N\psi_{2N+1}) = 2\psi_2 + \psi_3 + 4\psi_4 + \ldots$$

$$\gamma_E = \sum_{N=1}^{\infty} [(2N+1)\psi_{2N} + 2N\psi_{2N+1}] = 3\psi_2 + 2\psi_3 + 5\psi_4 + \ldots$$

The ribbon width is inversely proportional to the stacking fault energy, γ, that is either known for a dislocations in basal or prismatic planes for several HCP metals (Table 1.5). Experimental works are not the only method used to efficiently determine missing information for Mg alloy, recently, first principles calculations based on density functional theory (DFT) have been used for this matter [41-42]. Recently properties of Pure Mg and Mg alloys have been calculated for bulk, surface, stacking faults and twin boundary energies [43-44]. In order to test the reliability of the simulation model, equilibrium lattice parameters of various metals compare to the experimental value that is in good agreement with the corresponding experimental value. The key dominant method for studying mechanical properties was captured in a more comprehensive approach by Vitek, who introduced the concept of the generalized stacking fault (GSF) energy surface [45]. The GSF energy is crucial to describing accurately the dislocation core structure. There are computational materials science and engineering approaches in alloy development by using thermodynamic and first principles modeling. Shin and Wolverton describe three examples of how electron density functional theory can be used to provide valuable input to the CALPHAD approach, as well as the data necessary for kinetic modeling [46].

Table 1.5 Stacking fault energy, γ, for a dislocations in the basal plane[a] and prismatic plane[b] of various HCP metals [47].

Materials	Stacking fault energy, erg/cm^2
Cd	250 ~ 300[a]
	170[a]
	150[a]
Zn	250 ~ 300[a]
	300[a]
Co	25[a]
	26[a]
Mg	250 ~ 300[a]
	300[a]
	60[a]
Zr	250 ~ 300[a]
	56[b]
Ti	250 ~ 300[a]
	300[a]
	145[b]
Be	250 ~ 300[a]
	180[a]
	190[a]

1.5 Factors affecting the deformation modes

1.5.1 Orientation factor

The Schmid factor (SF) is a geometrical relationship between the corresponding deformation mode and the direction of force. If specimens of given substance are deformed in uni-axial loading, the values of the normal stress F at which slip or twin is first detected can be measured as a function of the orientation of slip system. And define $\emptyset$ is angle between the normal to the slip or twinning plane; λ is angle between the slip direction. It has frequently been found that the product $\frac{F}{A}.\cos\emptyset\cos\lambda$ is constant at the onset of slip or twin as exemplified by the data from anthracene crystals. This has led to the important conclusion that: In crystals of a given substance under constant conditions, extensive glide occurs when the resolved shear stress attains a critical value, the critical resolved shear stress. Therefore

$$\tau_c = \sigma_y.\cos\emptyset\cos\lambda$$

Where τ_c and σ_y are the critical resolved shear stress (CRSS) and the uni-axial yield strength, respectively. In HCP metals, the resolved shear stresses of the various deformation modes are strongly dependent on the direction of force, especially with respect to the c-axis. Since low offer of deformation modes, the HCP metals with certain orientation show a pronounce tendency to geometrical hardening or softening.

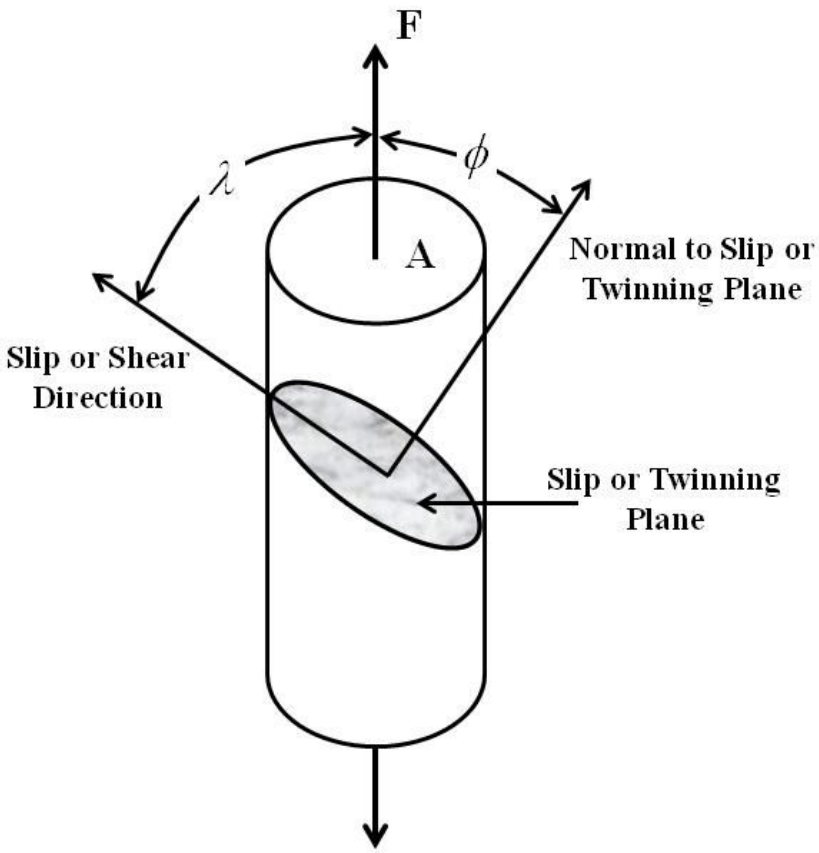

Figure 1.10 Schematic diagram of relationship between the shearing stress acting in the slip and twinning modes and the force applied externally on the specimen.

1.5.2 Critical resolved shear stress

For a given deformation mode, slip takes place if the resolved shear stress exceeds a critical value. CRSS value constitutes of material properties that are mainly influenced by temperature, impurities, and strain rate et.al. [48]. The deformation mechanisms of Mg have been studied in the middle stage of twentieth century in a wide temperature range from approximately 83 K to above 623K [49-51]. The activation modes of magnesium at low homologous temperatures were found to be mainly basal slip and twinning due to their relatively low CRSSs compare with other slip and twin modes [52]. The previously discussed results apply to temperatures near room temperature. However, prismatic or <c+a> slip modes may not operate in regions above or below the room temperature. Generally, twinning is preferred to slip at low temperatures; at elevated temperatures, however, slip is favored.

The CRSS required to initiate the corresponding deformation mode may be influenced by impurities or alloy elements inserted into interstitial or substitutional positions in a solution, and thus affects strength. The impurity atoms cause lattice strain that can "anchor" dislocations [53]. This occurs when the strain caused by the alloying element compensates that of the dislocation, thus achieving a state of low potential energy. It costs strain energy for the dislocation to move away from this state. The scarcity of energy at low temperatures is why the slip is hindered. Pure metals are almost always softer than their alloys. On the other hand, the concept of solute softening, rather than strengthening, was reported by Akhtar and Teghtsoonian who showed that the CRSS for prismatic slip of Mg single

crystals decreased with the addition of Zn [52].

1.6 Research objectives

In the current study, 3 different orientations were prepared and deformed at various temperatures. The CRSS values for the major slip and twinning modes were systematically derived by using tensile tested flow curves. For the single slip condition, the SF was used, and in case of multiple slip, the viscoplastic self-consistent (VPSC) model was utilized. From the CRSS derivation, the resolved shear stresses that activate the prismatic, pyramidal and <c+a> slip modes are much greater than those required to initiate the basal slip and tensile twin at room temperature. Therefore, the predominant deformation modes of magnesium at room temperature are the basal slip and tensile twin. The interactions between the dislocations and twin boundaries are important because the deformation-induced twins could act as obstacles to dislocation motion. The effects of twin on deformation and recrystallization behavior of Mg single crystals were systematically investigated by scanning electron microscopy (SEM) and electron backscattering diffraction (EBSD) analysis.

Additionally, the effects of the initial orientation on the mechanical behaviors and subsequently the major slip and twin modes with corresponding orientations were evaluated in systematic manner. Furthermore, we extended understanding of the interactions between slip dislocations and the $\{10\bar{1}2\}$ tensile twin. Up to date, there have been few works on the interactions between twinning modes, especially in the case of Mg and Mg alloys. By using single crystals, we systematically investigate the twinning effects on the mechanical properties through two-step compression (TSC) tests.

Bibliography

1. M. H. Yoo, "Slip, Twinning, and Fracture in Hexagonal Close-Packed Metals", Metal. Trans. A, 12 (1981), pp. 409-418.
2. C.J. Bettles and M.A. Gibson, "Current Wrought Magnesium Alloys: Strengths and Weaknesses", JOM., 57 (2005), pp. 46-49.
3. Z. Yang, J.P. Li, J.X. Zhang, G.W. Lorimer and J. Robson, "Review on Research and Development of Magnesium Alloys", Acta Metall. Sin., 21 (2008), pp. 313-328.
4. A. Inoue, Y. Kawamura, M. Matsushita, K. Hayashi and J. Koike, "Novel Hexagonal Structure and Ultrahigh Strength of Magnesium Solid Solution in the Mg–Zn–Y System", J. Mater. Res., 16 (2001), pp. 1894-1900.
5. T. Homma, N. Kunito and S. Kamado, "Fabrication of Extraordinary High-strength Magnesium Alloy by Hot Extrusion", Scripta Mater., 61 (2009), pp. 644-647.
6. C. Xu, M.Y. Zheng, S.W. Xu, K. Wu, E.D. Wang, S. Kamado, G.J. Wang and X.Y. Lv, "Ultra High-strength Mg–Gd–Y–Zn–Zr Alloy Sheets Processed by Large-strain Hot Rolling and Ageing", Mater. Sci. Eng. A, 547 (2012), pp. 93-98.
7. P.G. Partridge, "The Crystallography and Deformation Modes of Hexagonal close-packed Metals", Met. Rev., 12 (1967), pp. 169-194.
8. G. Lu, N. Kioussis, V.V. Bulatov and E. Kaxiras, "The Peierls-Nabarro Model Revisited", Phil. Mag. Lett., 80 (2000), pp. 675-682.
9. E.C. Burke and W.R Hibbard, "Plastic Deformation of Magnesium Single Crystals", Metal. Trans. A, 194 (1952), pp. 295-303.

10. R.E. Reed-Hill and W.D. Bobertson, “Deformation of Magnesium Single Crystals by Nonbasal Slip”, Trans. Metall. Soc. AIME., 209 (1957) pp. 496-502.
11. H. Yoshinaga and R. Horiuchi, “On the Nonbasal Slip in Magnesium Crystals”, Trans. JIM., 5 (1963), pp. 14-21.
12. J.F. Stohr and J.P. Poirier, “Electron Microscope Study of Pyramidal Slip. $\{11\bar{2}2\}$ $<11\bar{2}3>$ in Magnesium”, Phil. Mag., 25 (1972), pp. 1313-1329.
13. T. Obara, H. Yoshinga and S. Morozumi, “$\{11\bar{2}2\}$ $<11\bar{2}3>$ Slip System in Magnesium”, Acta Metall., 21 (1973), pp. 845-853.
14. S. Ando, N. Harada, M. Tsushida,H. Kitahara and H. Tonda, “Temperature Dependence of Deformation Behavior in Magnesium and Magnesium Alloy Single Crystals”, Key Eng. Mater., 345-346 (2007), pp. 101-104.
15. M.H. Yoo, S.R. Agnew, J.R. Morris and K.M. Ho, “Non-basal Slip Systems in HCP Metals and Alloys: Source Mechanisms”, Mater. Sci. Eng. A, 319-321 (2001), pp. 87-92.
16. J. Koike, T. Kobayashi, T. Mukai, H. Watanabe, M. Suzuki, K. Maruyama and K. Higashi, “The Activity of Non-basal Slip Systems and Dynamic Recovery at Room Temperature in Fine-grained AZ31B Magnesium Alloys”, Acta Mater., 51 (2003), pp. 2055-2065.
17. T. Mukai, M. Yamanoi, H. Watanabe and K. Higashi, “Ductility Enhancement in AZ31 Magnesium Alloy by Controlling Its Grain Structure”, Scripta Mater., 45 (2001), pp. 89-94.
18. J.W. Christian and S. Mahajan, “Deformation Twinning”, Prog. Mater. Sci., 39 (1995), pp. 1-157.
19. H. Yoshinaga and R. Horiuchi, “Deformation Mechanisms in Magnesium Single Crystals Compressed in the Direction Parallel to

Hexagonal Axis", Trans. JIM., 4 (1963), pp. 1-8.

20. L. Jiang, J.J. Jonas, A.A. Luo, A.K. Sachdev and S. Godet, "Twinning-induced Softening in Polycrystalline AM30 Mg Alloy at Moderate Temperatures", Scripta Mater., 54 (2006), pp. 771-775.
21. M.R. Barnett, Z. Keshavarz, A.G. Beer and X. Ma, "Non-Schmid Behaviour during Secondary Twinning in a Polycrystalline Magnesium Alloy", Acta Mater., 56 (2008), pp. 5-15.
22. L. Jiang, J.J. Jonas, A.A. Luo, A.K. Sachdev and S. Godet, "Influence of $\{10\bar{1}2\}$ Extension Twinning on the Flow Behavior of AZ31 Mg Alloy", Mater. Sci. Eng. A, 445-446 (2007), pp. 302-309.
23. J. Koike, "Enhanced Deformation Mechanisms by Anisotropic Plasticity in Polycrystalline Mg Alloys at Room Temperature", Metall. Mater. Trans. A, 36 (2005), pp. 1689-1696.
24. R.E. Reed-Hill and W.D. Robertson, "Additional Modes of Deformation Twinning in Magnesium", Acta Metal., 5 (1957), pp. 717-727.
25. Y.N. Wang and J.C. Huang, "The Role of Twinning and Untwinning in Yielding Behavior in Hot-extruded Mg–Al–Zn Alloy", Acta Mater., 55 (2007), pp. 897-905.
26. D. W. Brown, S. R. Agnew, M. A. M. Bourke, T. M. Holden, C. N. Tome and S. C. Vogel, "Internal Strain and Texture Evolution during Deformation Twinning in Magnesium", Mater. Sci. Eng. A, 399 (2005), pp. 1-12.
27. J. Jiang, A. Godfrey, W. Liu and Q. Liu, "Identification and Analysis of Twinning Variants during Compression of a Mg–Al–Zn Alloy", Scripta Mater., 58 (2008), pp. 122-125.
28. Q. Ma, H.E. Kadiri, A.L. Oppedal, J.C. Baird, M.F. Horstemeyer and M. Cherkaoui, "Twinning and Double Twinning Upon Compression of

Prismatic Textures in an AM30 Magnesium Alloy", Scripta Mater., 64 (2011), pp. 813–816.

29. K. Hantzsche, J. Bohlen, J. Wendt, K.U. Kainer, S.B. Yi and D. Letzig, "Effect of Rare Earth Additions on Microstructure and Texture Development of Magnesium Alloy Sheets", Scripta Mater., 63 (2010), pp. 725–730.
30. M.R. Barnett, M.D. Nave and C.J. Bettles, "Deformation Microstructures and Textures of Some Cold Rolled Mg Alloys", Mater. Sci. Eng. A, 386 (2004), pp. 205–211.
31. S. Suwas, G. Gottstein and R. Kumar, "Evolution of Crystallographic Texture during Equal Channel Angular Extrusion (ECAE) and Its Effects on Secondary Processing of Magnesium", Mater. Sci. Eng. A, 471 (2007), pp. 1–14.
32. W.J. Kim, J.D. Park and W.Y. Kim, "Effect of Differential Speed Rolling on Microstructure and Mechanical Properties of an AZ91 Magnesium Alloy", J. Alloys Compd., 460 (2008), pp. 289–293.
33. S.H. Park, S.G. Hong and C.S. Lee, Scripta Mater., 62 (2010), pp. 202–205.
34. M.A. Meyers, O.Vohringer and V.A. Lubarda, "The Onset of Twinning in Metals: A Constitutive Description", Acta Mater., 49 (2001), pp. 4025–4039.
35. Z.S. Basinski, M.S.Szczerba, M. Niewczas, J.D.Embury and S.J. Basinski, "The Transformation of Slip Dislocations during Twinning of Copper-aluminum Alloy Crystals", Rev. Metall., 94 (1997), pp. 1037-1043.
36. S.G. Hong, S.H. Park and C.S. Lee, "Role of $\{10\bar{1}2\}$ twinning characteristics in the deformation behavior of a polycrystalline

magnesium alloy", Acta Mater., 58 (2010), pp. 5873–5885.

37. T. Al-Samman and G. Gottstein, "Dynamic Recrystallization during High Temperature Deformation of Magnesium", Mater. Sci. Eng. A, 490 (2008), pp. 411–420.
38. X. Li, P. Yang, L.N. Wang, L. Meng and F. Cui, "Orientational Analysis of Static Recrystallization at Compression Twins in a Magnesium Alloy AZ31," Mater. Sci. Eng. A, 517 (2009), pp. 160–169.
39. S.W. Xu, S. Kamado, N. Matsumoto, T. Honma and Y. Kojima, "Recrystallization Mechanism of As-cast AZ91 Magnesium Alloy during Hot Compressive Deformation", Mater. Sci. Eng. A, 527 (2009), pp. 52–60.
40. J.P. Hirth and J. Lothe, "Theory of Dislocations", 2nd Edition (1982), pp. 354-357.
41. X.Z. Wu, R. Wang and S.F Wang, "Generalized-stacking-fault Energy and Surface Properties for HCP Metals a First-principles Study", App. Surf. Sci., 256 (2010), pp. 3409-3412.
42. J.A Yasi, T. Nogaret, D.R. Trinkle, Y. Qi, L.G. Hector Jr and W.A. Curtin, "Basal and Prism Dislocation Cores in Magnesium: Comparison of First-principles and Embedded-atom-potential Methods Predictions", Model. Simul. Mater. Sci. Eng., 17 (2009), pp. 1-13.
43. A. Datta, U.V. Waghmare and U. Ramamury, "Structure and Stacking Faults in Layered Mg–Zn–Y Alloys: A first-principles Study", Acta Mater., 56 (2008), pp. 2531-2539.
44. A.E. Smith, "Surface, Interface and Stacking Fault Energies of Magnesium from First Principles Calculations", Surf. Sci., 601 (2007), pp. 5762-5765.
45. V. Vitek, "Intrinsic Stacking Faults in Body-centred Cubic Crystals",

Phil. Mag., 18 (1968), pp. 773-786.

46. D.W. Shin and C. Wolverton, “First-principles Density Functional Calculations for Mg Alloys: A Tool to Aid in Alloy Development”, Scripta Mater., 63 (2010), pp. 680-685.
47. E. Tenckhoff, “Deformation Mechanisms in Zirconium and Zircaloy”, (1988), pp. 9-9.
48. H.L. Fotedar and T.G. Stoebe, “Effect of Temperature, Strain Rate and Impurity Content on the Work Hardening Characteristics of Lif Single Crystals”, Phil. Mag., 23 (1971), pp. 859-867.
49. A.Akhtar and E.Teghtsoonian, “Solid Solution Strengthening of Magnesium Single Crystals-I Alloying Behaviour in Basal Slip”, Acta Metall., 17 (1969), pp. 1339-1349.
50. A.Akhtar and E.Teghtsoonian, “Solid Solution Strengthening of Magnesium Single Crystals-II The effects of Solute on the Ease of Prismatic Slip”, Acta Metall., 17 (1969), pp. 1351-1356.
51. A.Akhtar and E.Teghtsoonian, “Substitutional Solution Hardening of Magnesium Single Crystals”, Phil. Mag., 25 (1972), pp. 897-916.
52. P.B. Hirsch and J.S. Lally, “The Deformation of Magnesium Single Crystals”, Phil. Mag., 12 (1965), pp. 595-648.
53. M. Bocek, P. Kratochvil and P. Lukac, “On the Effect of Impurities on the Critical Resolved Shear Stress of Zinc Single Crystals”, Czechoslovak J. Phys., 11 (1961), pp. 674-678.

Chapter 2. Experimental procedure

2.1 Single crystal growth and sample preparation

A large single crystal of pure magnesium was grown by the modified vertical Bridgman method as shown in Figure 2.1. A graphite mold filled with a pure magnesium ingot placed into a vertical furnace and lowered at the speed of less than 5mm/hr under a protective environment. Figure 2.2 shows schematic illustration of the graphite mold. This procedure consistently produced good quality single crystals. Large single crystal of dimensions 14 x 30 x 190 mm was produced in one run. Fig. 2.3 shows picture of schematic illustration of large single crystal. The crystallographic orientation of a single crystal was determined by the Laue back reflection method. X-rays were generated by MWL110 X-ray generator with 15kV voltage at -5mA current. The crystals whose misorientations among three Laue patterns were less than 2° were selected for the experiments. The Laue patterns from parent crystals were indexed using Orient Express 3.4. Test specimens with pre-determined orientations were machined from the as-grown single crystals using a wire spark erosion machine. These as-grown single crystals were mechanically polished with silicon carbide (SiC) papers and annealed in an evacuated Pyrex tube at 420^{o}C for 4 hours to eliminate dislocations that were introduced during the sample preparation. Finally, the oxides on the specimen surface were carefully removed by chemical polishing using a solution of CH_3OH and HNO_3 (volume ratio of 2:1).

Figure 2.1 Crystal growing apparatus.

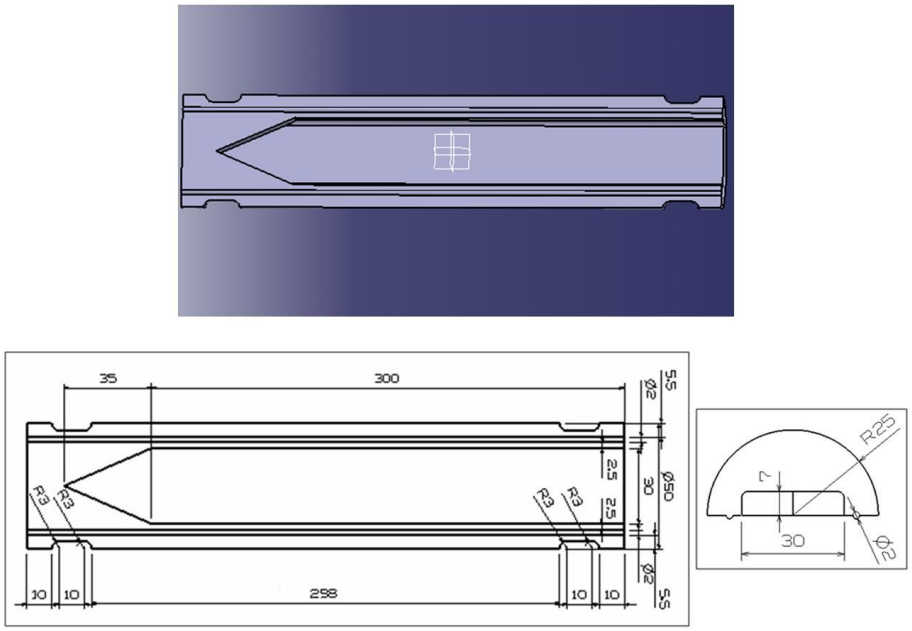

Figure 2.2 Schematic illustration of the graphite mould used for the crystal growth.

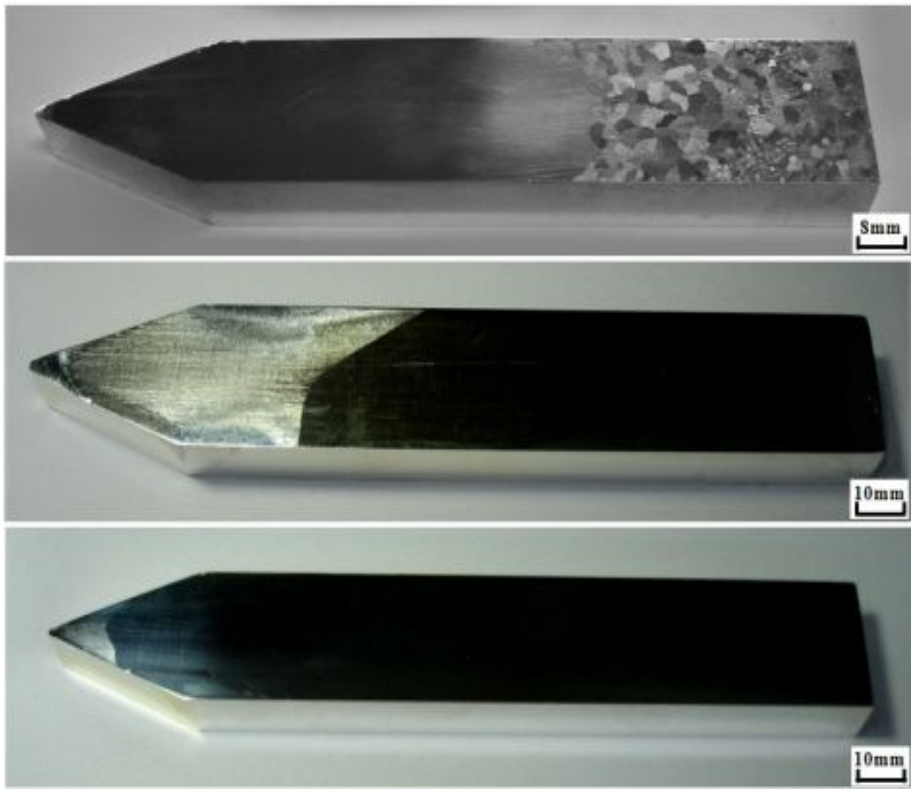

Figure 2.3 Large single crystal of pure magnesium was grown by the modified vertical Bridgman method.

2.2 Characterization of single crystals

2.2.1 Mechanical property

Tensile, compression, and two-step compression (TSC) tests were employed to evaluate mechanical behaviors of Mg single crystals with an initial strain rate of $1x10^{-4}$/sec. Rectangular tensile specimens (3x2x12 mm), compressive and TSC (4x4x6 mm) specimens were cut from the original crystals. A special gripping system was designed for the testing specimen to ensure an accurate alignment of the loading axis for tensile test (Figure 2.4).

2.2.2 Microstructure

The microstructure was examined by optical microscopy. Specimens for microstructure observation were mechanically polished with sandpapers from #600 to #4000 and then polished with 0.3, 0.05㎛ alumina powder. These specimens were then etched with a solution of CH_3OH and HNO_3 (volume ratio of 2:1). For the defect analysis, samples were cut into 800 μm slices using MTI precision wire saw, and then ground to 130 μm in thickness using a series of sandpapers down to a 2000 grit number. 3 mm disks were mechanically punched from those slices and twin-jet electro-polished using a Tenupol-5 in a solution of 20 ml perchloric acid, and 980 ml ethanol. TEM observations were then carried out on a Tecnai F20 operating at 200 kV to obtain various two-beam bright-field images and weak-beam dark-field (WBDF) images. High-resolution TEM (HRTEM) was performed on a JEM-3000F microscope with an accelerating voltage of 300 kV.

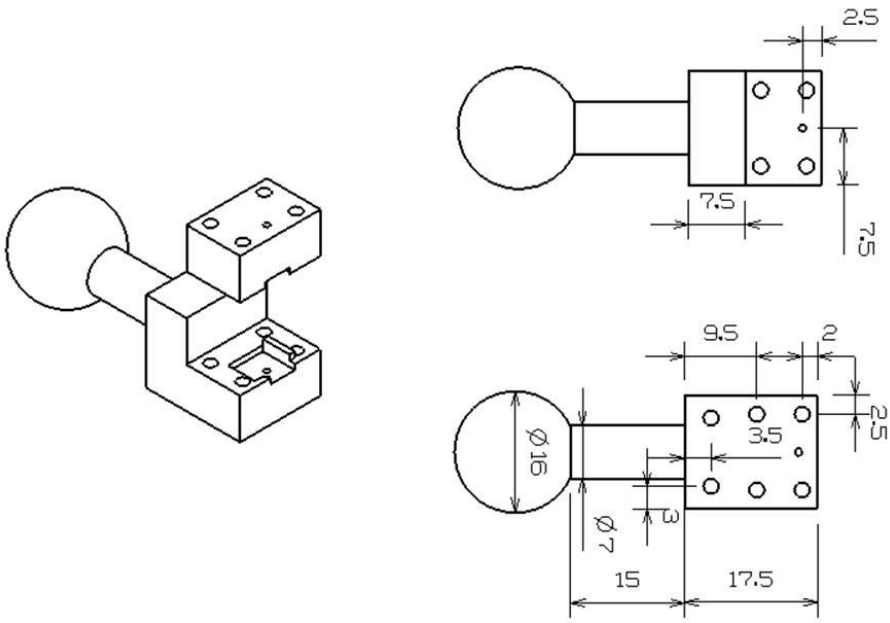

Figure 2.4 Design for tensile test jig.

2.2.3 Texture

Macrotextures were measured by X-ray diffraction (XRD) using a PANalytical X'Pert PRO X-ray diffractometer with a Cu Kα source. The pole figures of initial orientations were taken from the surface and compressed specimens were measured at the mid-thickness plane. Complete pole figures were acquired from the orientation distribution function (ODF) calculated using the arbitrarily defined cells (ADC) method in the LaboTex 3.0 software. Local textures were measured by electron backscatter diffraction (EBSD) using FE-SEM (SU70, HITACHI) fitted with a TSL EBSD camera operating at 20 kV, 70^{o} tilting angle. Samples were prepared by mechanical polishing using alumina powder, followed by chemical etching in an etchant of acetic – picral (4.2 g picric acid, 10 ml acetic acid, 10 ml H_2O, and 70 ml ethyl alcohol). Automated EBSD scans were measured in the stage-control mode using TSL data acquisition software at a step size of 0.2~0.5 μm, and the data with a confidence index >0.1 were used for texture and twin analysis.

2.2.4 Simulation

Simulation of deformation behavior and texture has been shown to be a powerful tool to investigate deformation mechanisms and texture formation. Based on these experimental results, deformation simulations were carried out using the viscoplastic self-consistent (VPSC) implemented into a genetic optimization algorithm (GA) theory in order to predict the contributions of various deformation modes to the deformation behavior. The calculations have included the {0001} <11$\bar{2}$0>, {10$\bar{1}$0} <11$\bar{2}$0>, {11$\bar{2}$2} <11$\bar{2}$3> slip and {10$\bar{1}$2} <10$\bar{1}$1> and {10$\bar{1}$1} <10$\bar{1}$2> twinning modes.

Chapter 3. Effects of orientation and temperature on slip and twin behavior of Mg single crystals

3.1 Introductions

The HCP structure has a limited number of independent slip systems, and profuse twinning modes on pyramidal planes taking place in the plastic deformation of Mg and its alloys [1]. The basal slip and $\{10\bar{1}2\}$ twin are prevalent deformation modes of Mg and its alloys because their CRSS values are much lower than that of other deformation modes, such as the prismatic, pyramidal and <c+a> slip modes [2]. Because of the large differences between the activation energies of each deformation mode, the mechanical behavior shows strong anisotropic characteristics [3-4].

In the mid-twentieth century, there were a few papers related to CRSS for various deformation modes of Mg single crystals. Burke and Hibbard carried out a tensile test at room temperature using several orientations [5]. Read-Hill and Robertson suggested that pyramidal-1 was an active system at room temperature in a particular condition [6]. On the other hand, Wonsiewicz and Kelly carried out a plane-strain compression test along the c-axis and reported that neither the prismatic slip nor pyramidal slip accommodated a significant amount of strain in pure magnesium at room temperature [7-8]. However, the literature lacks significant data regarding the critical resolved shear stresses for the various slip systems. Obara et.al carried out extensive works and evaluated CRSS values for the slip and twinning modes by using the Schmid criterion even in multiple slip conditions [9]. It was generally known that in single slip cases, the Schmid criterion was used to derivate

CRSS values for corresponding deformation modes. However, the usefulness of the Schmid criterion has recently been questioned for multiple slip conditions [10-12]. In order to further evaluate the CRSS values in multiple slip conditions, Chapuis and Driver adopted a rate-insensitive model to calculate the stress state and active slip and twinning modes under channel die compressive deformation [2]. Unfortunately, the calculated value was much larger than the value measured in tensile tests because of the channel die effects. Due to the importance of Mg alloys, many works studies have been performed to look at the fundamental properties by using Mg single crystals [13-20].

In the current study, 3 different orientations were prepared and deformed at various temperatures. The CRSS values for the major slip and twinning modes were systematically derived by using tensile and compressive tested flow curves. For the single slip condition, the Schmid criterion was used, and in case of the multiple slip, the viscoplastic self-consistent (VPSC) model was utilized. For accuracy, the displacement was measured using the machine's linear variable displacement transducer (LVDT) even in elevated temperatures.

3.2 Results and discussion

In order to study the influence of the initial orientation on the deformation behavior of Mg single crystals, it is essential to choose a proper sample state. Table 3.1 shows the SF values for the major slip and twinning modes for the 3 different orientations.

Table 3.1 SF calculations for the slip twinning modes in the 3 different orientations.

Orientation	Basal	Prismatic	<c+a>	$\{10\bar{1}2\}$ Tensile Twin	$\{10\bar{1}1\}$ Compressive Twin
A	0.5	0.22	0.28	0.25	0.29
B	0	0.5	0.42	0.47	0.39
C	0	0.43	0.33	0.5	0.42

3.2.1 Orientation A

In case of orientation A, basal plane is inclined 45° to loading direction ($\overline{40}$ 20 20 37]). SF values for the basal slip is 0.5 and thus the sample A will be mainly deformed by the single basal slip. The flow stress (Figure 3.1) does not change enormously with temperatures for the A orientated specimen. After deformation, the microstructures were directly taken without further treatments including polishing and etching, since they can remove any trace of the slip steps. The surface steps were clearly presented at the $(0\bar{1}10)$ plane as shown in Figure 3.2. Trace predictions for the active basal slip mode is located in the left corner of Figure 3.2 that are based on the SF calculation. It is easily known that the basal slip traces were consistent with the theoretical geometric prediction and crystals mainly deformed by the basal slip at all temperatures.

3.2.2 Orientation B

Orientation B, the prismatic plane is inclined 45° and the basal plane is parallel to loading direction ([90 $\overline{123}$ 33 0]). The prismatic slip has maximum SF value 0.5 and the basal slip has minimum SF value 0, therefore the basal slip was suppressed and the prismatic slip supposed to be a main deformation mode by the geometric state. The stress-strain curves for the various temperatures are presented in Figure 3.3. Typically, the flow stresses exhibit limited strain hardening with the exception of the RT deformed specimen.

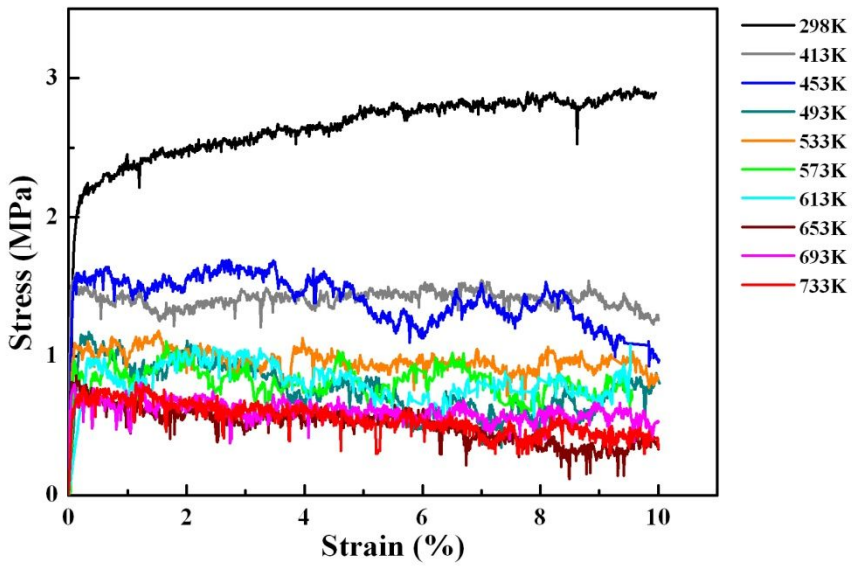

Figure 3.1 Typical stress-strain curves of orientation A from 298K to 733K.

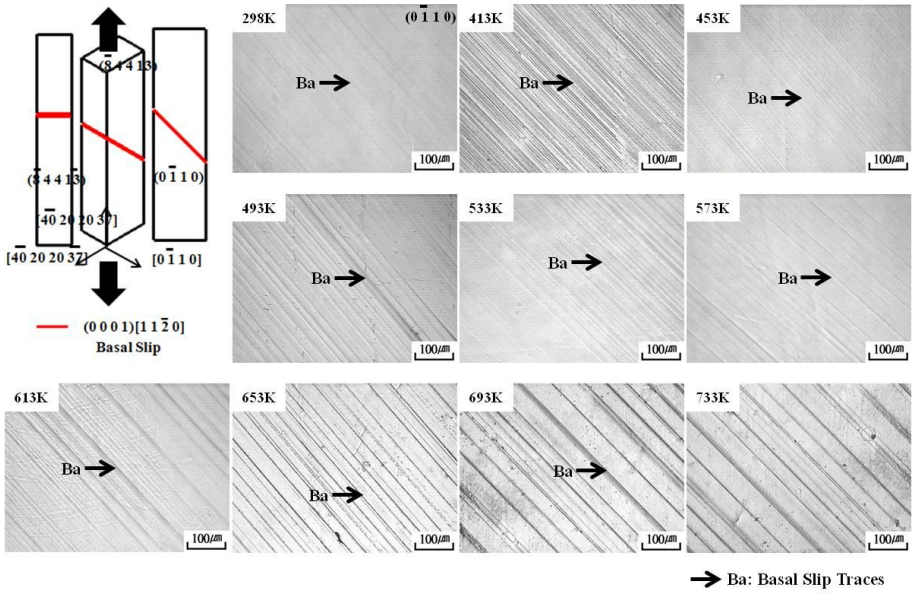

Figure 3.2 Microstructures taken from the sections of the $(01\bar{1}0)$ plane for orientation A.

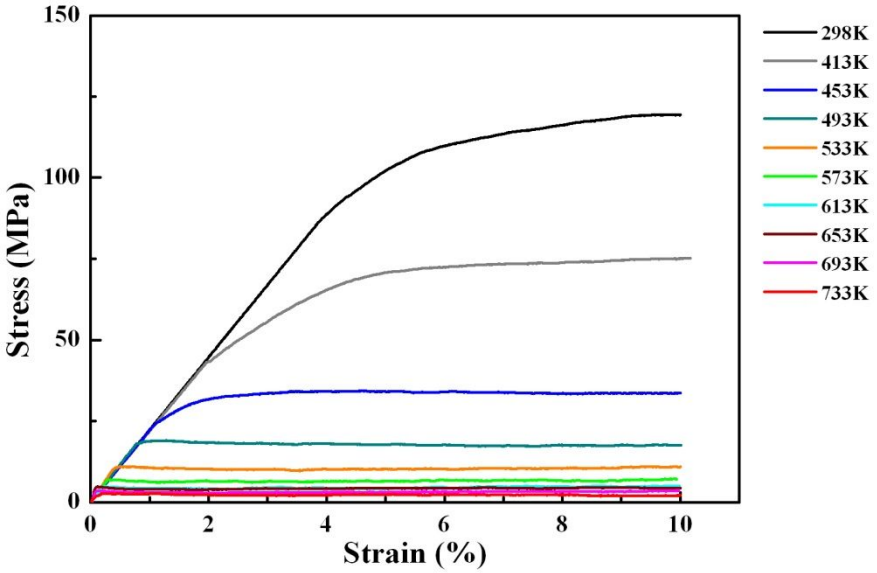

Figure 3.3 Typical stress-strain curves of orientation B from 298K to 733K.

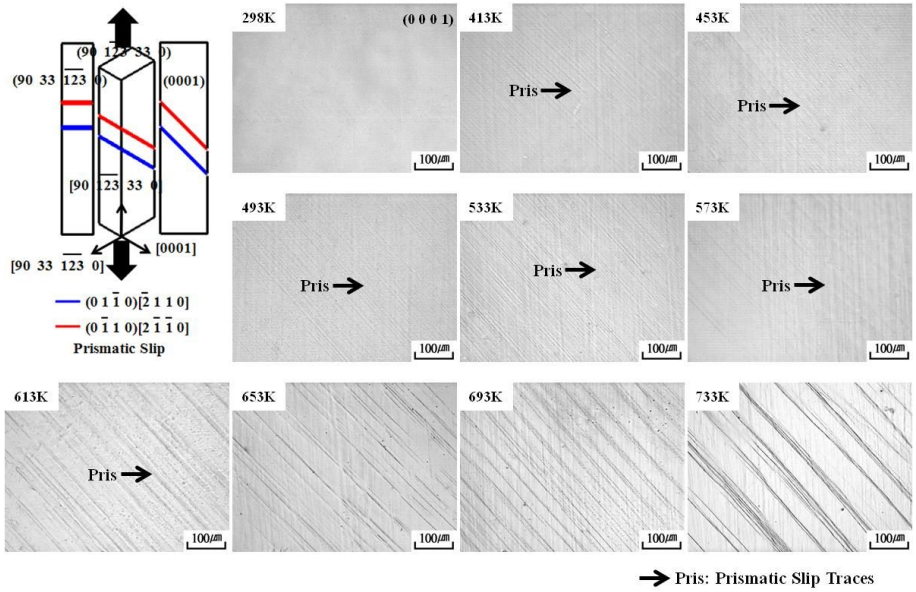

Figure 3.4 Microstructures are taken from the sections of the (0001) plane for orientation B.

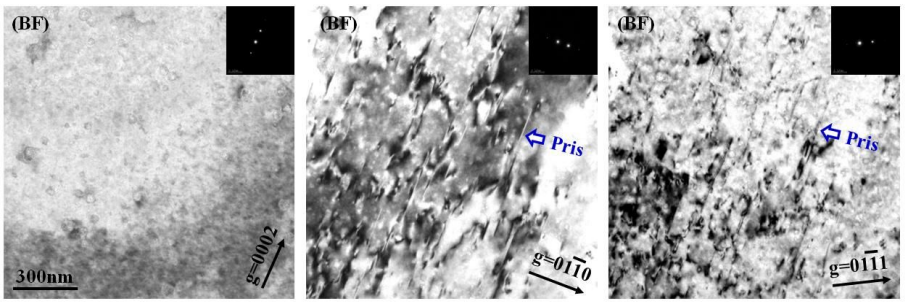

Figure 3.5 TEM bright-field image from RT deformed B type specimen, taken under two beam conditions using diffraction vector g= 0002 (a), g= 01$\bar{1}$0 (b), and g= 01$\bar{1}$1 (c).

Table 3.2 The g . b values for perfect dislocations in Mg crystals.

Zone Axis	Operating Reflection (±g)	Burgers Vectors										
		<a> Slip			<c+a> Slip						<c> Slip
		1/3[11-20]	1/3[1-210]	1/3[-2110]	1/3[11-23]	1/3[1-213]	1/3[-2113]	1/3[11-2-3]	1/3[1-21-3]	1/3[-211-3]	[0001]
[-2110]	[0002]	0	0	0	2	2	2	-2	-2	-2	2
	[01-10]	1	-1	0	1	-1	0	1	-1	0	0
	[01-11]	1	-1	0	2	0	1	0	-2	-1	1

Figure 3.4 shows the microstructures of the samples from the (0001) surface. The prismatic slip lines started to appear at 413K, and with an increase in temperature the prismatic slip lines gradually became distinct. Figure 3.5 images were taken with an incident electron beam direction of $<11\bar{2}0>$ under two-beam diffraction conditions for the RT deformed specimen, using reflections of g = 0002, g = $01\bar{1}0$, and g = $01\bar{1}1$, respectively. Based on the g . b criterion [21], dislocations having the <a> type Burgers vector are out of contrast and only <c> and <c + a> type dislocations are visible in Figure 3.5 (a). Table 3.2 shows the g . b values for all the perfect dislocations observed in Mg crystals. No dislocations appeared under a two-beam diffraction condition with g = 0002, indicating dislocations in the Figure 3.5 (b) and (c) belonging to the <a> type dislocations. Furthermore, almost all the dislocation segments are perpendicular to the basal plane. These results indicate that a major deformation mechanism in this orientation is the prismatic slip dislocation for the B type specimen even in room temperature, which concurs with the OM data.

3.2.3 Orientation C

Orientation C is used to activate the <c+a> slip when stretched along a-axis. Some of studies already proved the existence of the <c+a> dislocations by the TEM analysis and the $\{10\bar{1}2\}$ twin is dominant when compressed perpendicular to c-axis [22-24]. Evidence for the increased <c+a> slip activity is also given by the texture simulations that were carried out by different authors [25-27]. In this study, 2 different specimens were utilized and stretched and compressed along the $[0\bar{1}10]$ direction. The tensile and compressive flow curves decreased rapidly with increasing temperature.

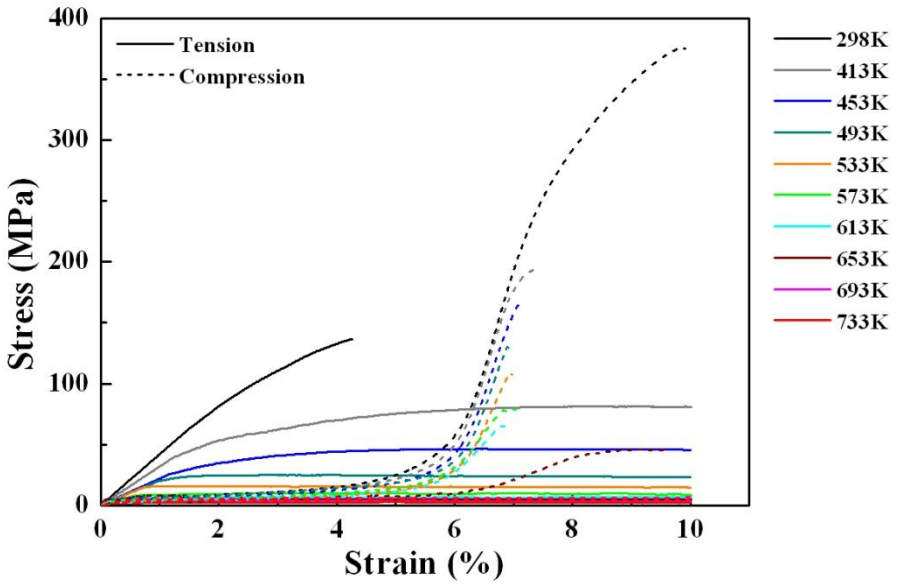

Figure 3.6 (a) Typical tensile and compressive flow curves of orientation C from 298K to 733K. (b) Enlargement of the marked box in the bottom left corner in (a).

Both orientation A and B were deformed by the single basal and prismatic slips according to the SF value and experimental data. In crystals of a given substance under constant conditions, the Schmid criterion ($\tau_c = \sigma_y * \cos\emptyset * \cos\lambda$) can be used to derive the CRSS values for the single slip condition [29]. The CRSS values for the basal slip were found insensitive to test temperatures, but the prismatic slip exhibited much higher CRSS compared to the basal slip and showed the strong temperature dependent behavior, as shown in Figure 3.7.

Recently, the usefulness of Schmid criterion for the multiple slip conditions has been questioned for the crystal plasticity modeling of Mg or its alloys. In order to solve this problem and derive reasonable CRSS values for the other deformation modes in multiple slip condition, computer simulations were carried out using the visco-plastic self-consistent (VPSC) theory [30-31]. The present calculations have included the major slip and twinning modes to analyze the tensile data of orientation C; the basal slip {0002} <11$\bar{2}$0>, second-order pyramidal slip {11$\bar{2}$2} <11$\bar{2}$3>, tensile twinning {10$\bar{1}$2} <10$\bar{1}$1> and compressive twinning {10$\bar{1}$1} <10$\bar{1}$2>. The Voce-type hardening rule is used to describe the evolution of the threshold stress as a function of accumulated shear strain in the grain, Γ :

$$\tau_c^s = \tau_0^s + (\tau_1^s + \theta_1^s\Gamma)[1 - \exp(-\theta_0^s\Gamma / \tau_1^s)] \qquad (3.1)$$

where Γ is the accumulated shear in the grain; τ_0^s, θ_0^s, θ_1^s and τ_1^s are the initial CRSS, the initial hardening rate, the asymptotic hardening rate and back-extrapolated stress, respectively. In order to fulfill the twin reorientation problem during plastic deformation, the predominant twin reorientation (PTR) scheme [32] was implemented in the VPSC code. At each incremental step, the accumulated twin fraction in the individual twinning systems of each grain

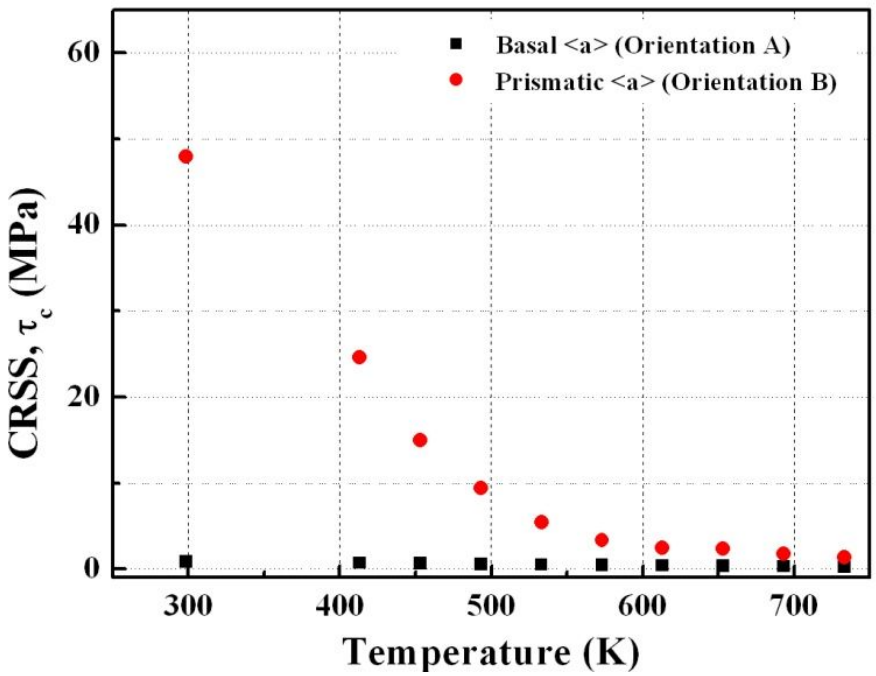

Figure 3.7 The CRSS values for the basal and prismatic <a> slip were derived by SF criterion.

is compared with a threshold fraction, $V^{th,mode}$, defined as follows:

$$V^{th,mode} = A^{th1} + A^{th2} \frac{V^{eff,mode}}{V^{acc,mode}} \quad (3.2)$$

where $V^{acc,mode}$ and $V^{eff,mode}$ are the accumulated twin fraction and the effective twinned fraction, respectively. The threshold values, A^{th1} and A^{th2}, determine the evolution of the twin volume fraction during plastic deformation. The parameters of the PTR-model are set as A^{th1} = 0.1 and A^{th2} = 0.8 for $\{10\bar{1}2\}$ twin; A^{th1} = 0.1 and A^{th2} = 0.5 for $\{10\bar{1}1\}$ twin. It is generally accepted that slip is rate sensitive, twinning is usually considered to be rate-insensitive. Since the derivation of twin stress and an evolution of twinning with temperatures are the main focus of this study, we have chosen to adopt a rate-insensitive model. The parameters obtained from the above procedure are listed in Table 3.3. The simulated tensile and compressive stress-strain curves were in good agreement with the experimental results for C oriented samples, as shown in Figure 3.8 (a). High magnification of the rectangular box located at the bottom left of the graph in Figure 3.8 (a) is illustrated in Figure 3.8 (b). After optimization of the model results, the absolute values of CRSS can be extracted. The CRSS values of the major deformation modes for the Mg crystals are summarized as a function of the testing temperature in Figure 3.9. At room temperature, the basal slip and $\{10\bar{1}2\}$ twin dominate the deformation mechanism because the CRSS for the other deformation modes such as the prismatic slip, <c+a> slip and $\{10\bar{1}1\}$ twin is considerably higher than that of the basal slip and $\{10\bar{1}2\}$ twin. The CRSS values of the prismatic slip, <c+a> slip and $\{10\bar{1}1\}$ twin are seen to decrease significantly as the test temperature increases, whereas the basal slip and $\{10\bar{1}2\}$ twin are insensitive to the test temperature. Figure 3.10 represents the evolution of the relative activities of various deformation modes during the tensile and compressive

Table 3.3 Best-fit model parameters describing the CRSS and hardening responses of the four deformation behavior as a function of temperature.

Mode	Voce Hardening	298K	413K	453K	493K	533K	573K	613K	653K	693K	733K
Basal <a>	τ_0	0.740	0.670	0.556	0.528	0.489	0.405	0.368	0.324	0.270	0.250
	τ_1	0.703	0.482	0.335	0.296	0.106	0.081	0.020	0.074	0.015	0.0004
	θ_0	415.530	409.990	208.840	159.560	58.410	25.414	11.712	8.714	2.790	1.527
	θ_1	100.040	46.593	35.341	11.326	5.644	3.909	2.218	1.290	0.476	0.284
	h^{ss}	1	1	1	1	1	1	1	1	1	1
Prism. <a>	τ_0	37.731	20.185	12.889	9.410	6.515	3.806	2.585	2.002	1.262	0.950
	τ_1	23.458	14.886	8.029	1.645	0.741	0.484	0.277	0.156	0.118	0.099
	θ_0	664.490	317.000	252.200	157.580	73.663	31.443	17.204	9.490	5.966	2.957
	θ_1	197.390	19.795	6.235	3.010	1.555	1.034	0.891	0.406	0.240	0.088
	h^{ss}	1	1	1	1	1	1	1	1	1	1
<c+a>	τ_0	54.990	30.823	23.929	17.074	10.188	6.256	3.243	2.156	1.339	0.954
	τ_1	48.896	17.076	17.222	8.887	3.204	1.130	0.842	0.693	0.310	0.190
	θ_0	996.950	434.750	329.550	232.890	144.950	32.359	24.823	18.925	8.541	5.919
	θ_1	173.720	96.325	76.454	42.974	15.411	11.712	4.111	2.959	1.444	0.712
	h^{ss}	1	1	1	1	1	1	1	1	1	1
$\{10\bar{1}2\}$ Twin	τ_0	1.710	1.664	1.639	1.579	1.556	1.526	1.510	1.499	1.323	1.199
	τ_1	1.084	1.066	0.955	0.891	0.875	0.562	0.421	0.394	0.254	0.062
	θ_0	45.575	27.154	22.803	18.099	15.343	13.233	6.314	5.887	2.520	1.284
	θ_1	20.508	19.574	12.130	8.277	6.678	6.268	3.059	2.899	0.203	0.068
	h^{ss}	3	3	3	3	3	3	3	3	3	3
$\{10\bar{1}1\}$ Twin	τ_0	93.521	62.865	51.381	40.272	30.418	24.700	16.700	11.784	6.041	2.939
	τ_1	36.258	22.006	19.617	9.749	8.942	4.254	2.746	1.075	0.661	0.478
	θ_0	1353.700	495.860	357.020	205.350	146.400	48.945	30.195	23.355	12.631	6.933
	θ_1	180.230	112.510	61.333	38.752	25.524	13.803	7.992	4.186	2.689	1.618
	h^{ss}	1	1	1	1	1	1	1	1	1	1

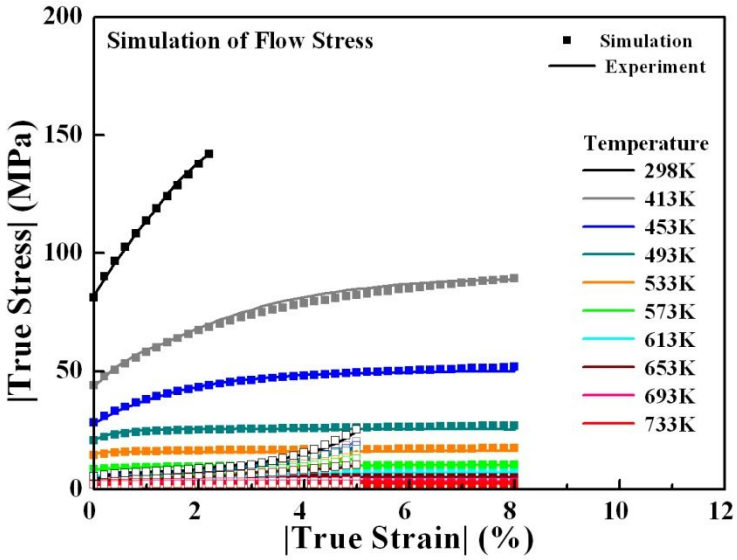

(a)

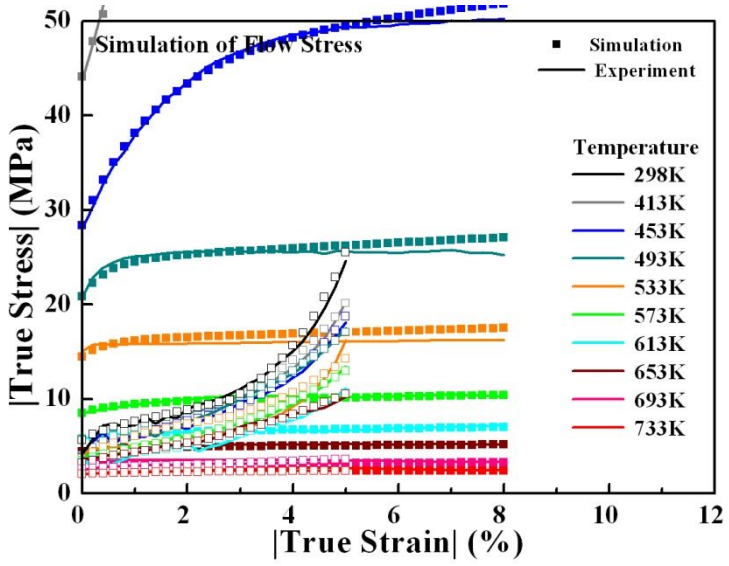

(b)

Figure 3.8 (a) Experimental and simulated stress-strain curves of C oriented samples. (b) Enlargement of the marked box in the bottom left corner in (a).

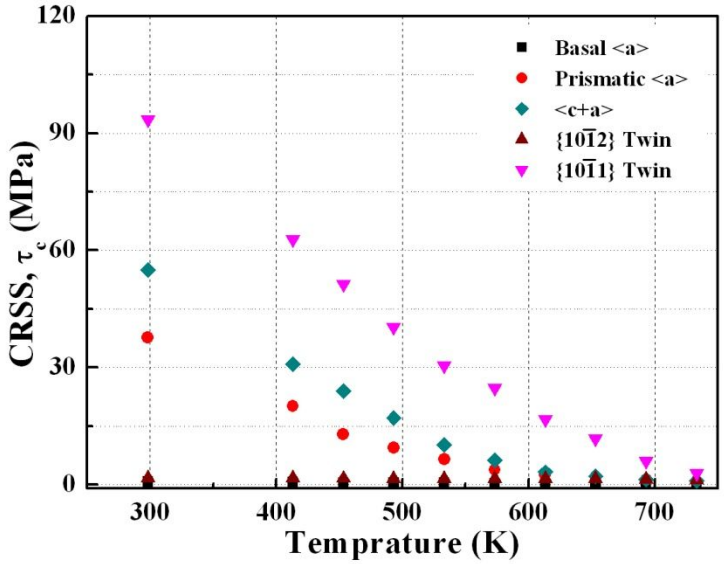

Figure 3.9 Derived CRSS values for the basal, prismatic, <c+a> slip, {10$\bar{1}$2} twin and {10$\bar{1}$1} twin modes from VPSC simulations.

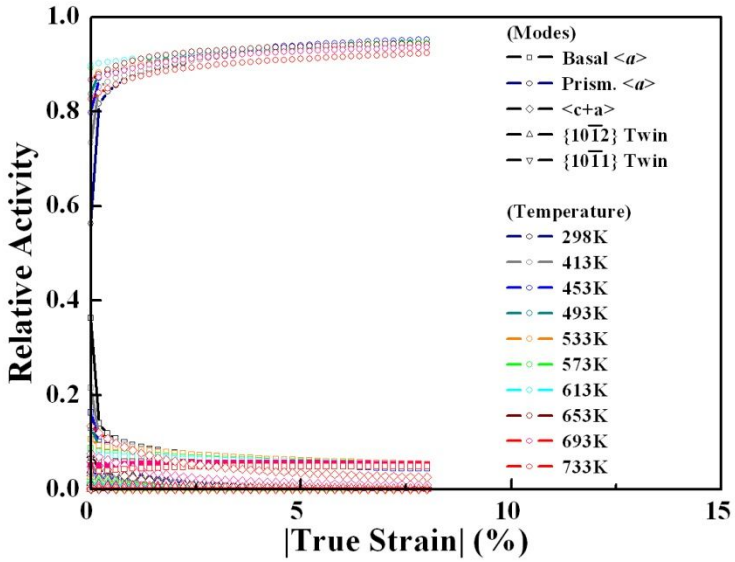

(a)

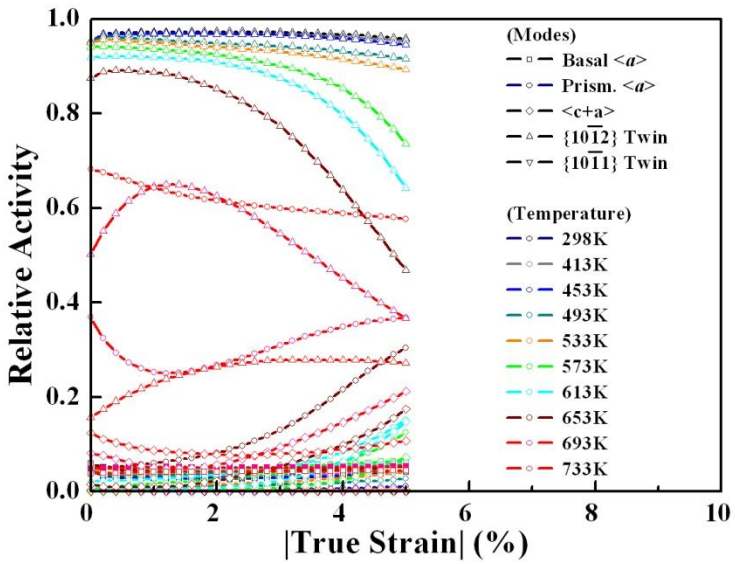

(b)

Figure 3.10 (a) and (b) show relative activities of the five deformation modes during uni-axial tension and compressive deformation, respectively.

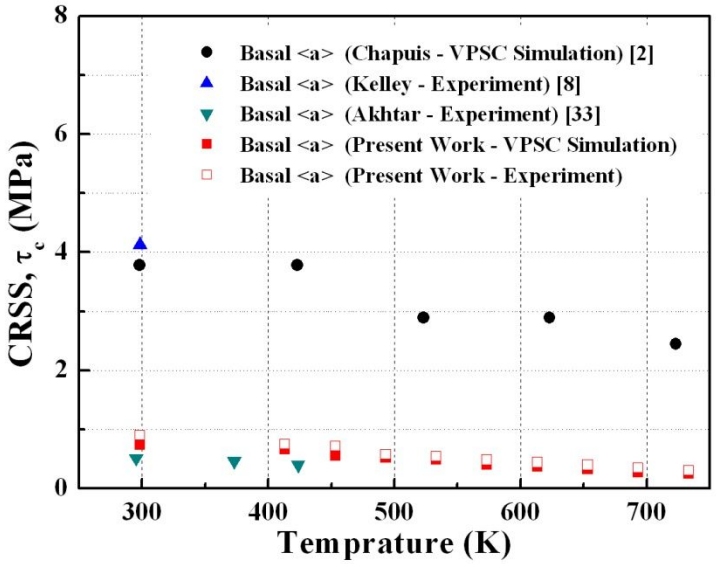
Basal <a> (Chapuis - VPSC Simulation) [2]
Basal <a> (Kelley - Experiment) [8]
Basal <a> (Akhtar - Experiment) [33]
Basal <a> (Present Work - VPSC Simulation)
Basal <a> (Present Work - Experiment)
CRSS, τ_c (MPa)
Temprature (K)
0
2
4
6
8
300
400
500
600
700

(a)

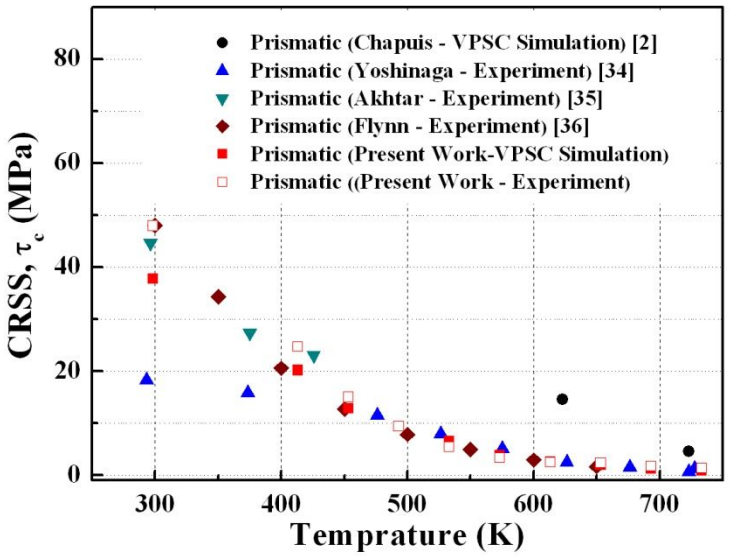
Prismatic (Chapuis - VPSC Simulation) [2]
Prismatic (Yoshinaga - Experiment) [34]
Prismatic (Akhtar - Experiment) [35]
Prismatic (Flynn - Experiment) [36]
Prismatic (Present Work-VPSC Simulation)
Prismatic ((Present Work - Experiment)
CRSS, τ_c (MPa)
Temprature (K)
0
20
40
60
80
300
400
500
600
700

(b)

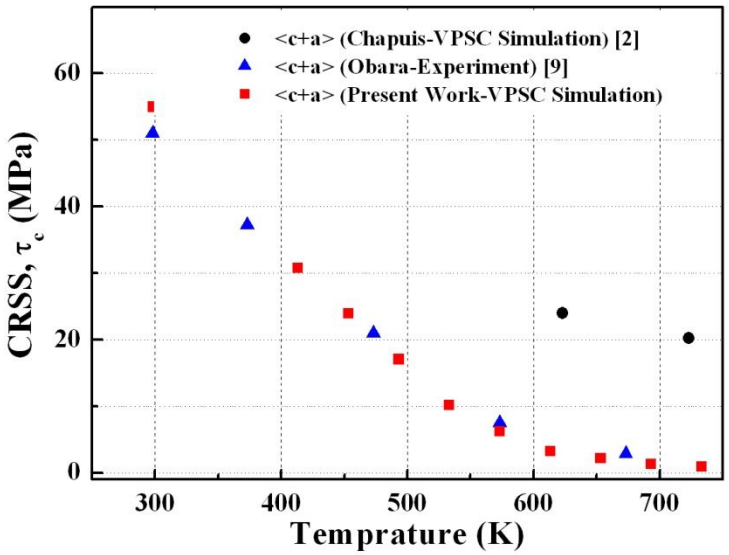

(c)

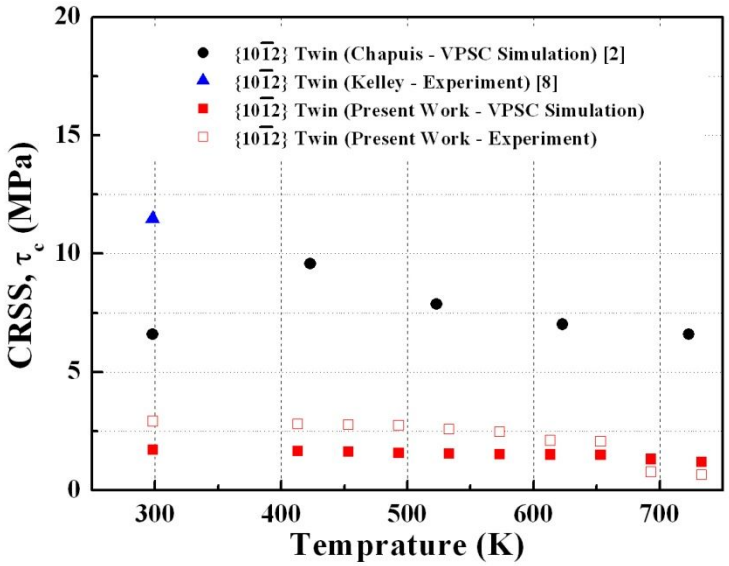

(d)

Figure 3.11 Comparison of CRSS values between present work and previously published data; (a) basal slip, (b) prismatic slip, (c) <c+a> slip and (d) {10$\bar{1}$2} twin.

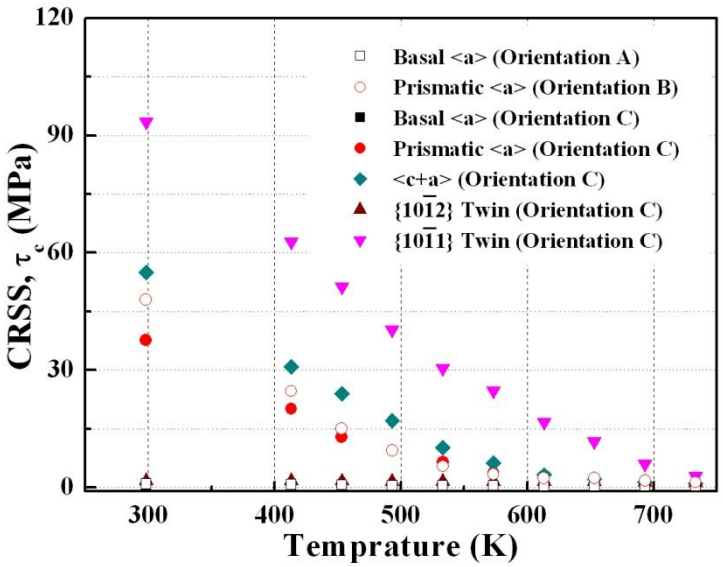

Figure 3.12 Temperature dependency of slip and twin modes.

deformations with various temperatures. During the tensile deformation, the prismatic slip is mainly activated. On the other hand, the contribution of the <c+a> slip is negligible from 298K to 573K deformation since there is noticeable difference between the prismatic and <c+a> slips. Furthermore, the Schmid factors for the prismatic slip is 0.43, and the <c+a> slip is 0.33, respectively, which may lead to the prismatic slip that plays an important role in this temperature region. It can be observed that the activity of the prismatic slip decreased with increasing temperature and there was a gradual increase in the activity of the <c + a> slip mode from 613 - 733K deformation. The contribution of the $\{10\bar{1}2\}$ twin decreased with testing temperature during the compression deformation. On the other hands, the prismatic and <c+a> slips increased with testing temperature.

The values obtained from the experiment and VPSC simulations were also compared with previously published CRSS values at various temperatures. The red fill symbols derived from the VPSC simulation results utilized C oriented specimen and the red hollow symbols are determined from experiment results by using the SF criterion, as shown in Figure 3. 11. It can be easily known that the simulated results showed similar values with the experimental results. Kelley and Chapuis's data [2] is much higher than the present study since they carried out plane-strain compression tests. The data published by Akhtar et al. [33] is relatively smaller which may due to impurity effects to the deformation behavior. In case of prismatic slip (Figure 3.11 (b)), simulated values are slightly lower than experimental values from 298 – 453 K, and well matched above than 493 K. The present values have similar values with Akhtar and Flynn published results [35-36]. In case of the <c+a> slip and $\{10\bar{1}2\}$ twin, there is no such orientation to activate the single <c+a> slip or single twin variant only, therefore experimental results are

missing in Figure 3.11 (c) and (d). In comparison, values of <c+a> slip have the similar trend with Obara et al. published data and values of $\{10\bar{1}2\}$ twin are much lower than Chapuis and Kelly [9,2,8] reported data, which may due to the friction force from constraint die, as mentioned previously. Despite the large difference in the magnitude of deformation modes, the dramatic decrease in the CRSS values of thermally activated prismatic and <c+a> slip mechanisms is similar to that published for single crystals over the observed temperature range. At these moderate temperatures, the basal slip and tensile twin are observed to behave athermally, such that further increases in temperature have no marked effect on the critical stress for activation. The basal slip is also the main deformation mechanism at elevated temperature.

Figure 3.12 summarized the values of major slip and twinning modes in this work. The CRSS of prismatic slip is lower than the <c+a> slip and confirmed as the second easiest slip mode. Recently, the recrystallization nucleation at the $\{10\bar{1}1\}$ twin was observed to be more effective than that of the parent matrix or tensile twins. Li and Xu investigated that the $\{10\bar{1}1\}$ twin induced recrystallization behavior in poly-crystalline AZ31 and AZ91 alloys [37-38]. Al-Samman et al. carried out the plane strain compression test by using Mg single crystals and tried to investigate the $\{10\bar{1}1\}$ twin induced DRX mechanisms [19]. However there is no reliable stress that has been established on the $\{10\bar{1}1\}$ twin which plays an effective recrystallization site in Mg and its alloys [18]. In this work, we derived the $\{10\bar{1}1\}$ twin stress by using VPSC simulation code. It was found that the $\{10\bar{1}1\}$ twin stress decreased rather steeply with increasing in test temperature and stress value was higher than other deformation modes. The $\{10\bar{1}1\}$ twin is readily observed during hot rolling process even the $\{10\bar{1}1\}$ twin stress is higher than

other deformation modes which may because of geometric condition. It is generally known that the $\{10\bar{1}1\}$ twin is easily activated by compression direction parallel to the c-axis. In this case, the <a> type slip modes are forbidden and the only possible active mode is the <c+a> slip among the slip modes. Unfortunately, the <c+a> slip was not enough to accommodate the large deformation, and thus the $\{10\bar{1}1\}$ twin became the active deformation mode at elevated temperature.

3.3 Conclusions

The CRSS value of the major slip and twinning modes for Mg single crystals undergoing tensile and compressive deformation have been systematically analyzed as a function of temperature. The orientation A and B are oriented for single basal and prismatic slip, and thus SF criterion is used to derive the CRSS values of basal and prismatic slip experimentally. In case of C oriented specimen, multiple deformation modes (unfavorable slip and twin mode) are contributed to the plastic deformation mode. VPSC code is adopted to derive other main deformation modes in Mg single crystals.

It is shown that the basal slip and the $\{10\bar{1}2\}$ twin remain essentially independent of temperature. The temperature dependence of the prismatic and <c+a> slip are very remarkable below 613 K, while above this temperature the CRSS values for both modes do not so much depend on the test temperature. Deformation activity of the prismatic slip decreased and the activity of the <c + a> slip increased from 613 - 733K deformation, since there is not much difference between the CRSS values of the prismatic and <c+a> slip. In case of the $\{10\bar{1}1\}$ twin, it is observed that the stress values decreases steeply with increasing the test temperature over all range.

Bibliography

1. P.G. Partridge, “The Crystallography and Deformation Modes of Hexagonal close-packed Metals”, Met. Rev., 12 (1967), pp. 169-194.
2. A. Chapuis and J.H. Driver, “Temperature Dependency of Slip and Twinning in Plane Strain Compressed Magnesium Single Crystals”, Acta Mater., 59 (2011), pp. 1986-1994.
3. S.R. Agnew, M.H. Yoo and C.N. Tome, “Application of Texture Simulation to Understanding Mechanical Behavior of Mg and Solid Solution Alloys Containing Li or Y”, Acta Metall., 49 (2001), pp. 4277-4289.
4. N.V. Dudamell, I. Ulacia, F. Galvez, S. Yi, J. Bohlen, D. Letzig, I. Hurtado and M.T. Perez-Prado, “Twinning and Grain Subdivision During Dynamic Deformation of a Mg AZ31 Sheet Alloy at Room Temperature”, Acta Mater., 59 (2011), pp. 6949–6962.
5. E.C. Burke and W.R Hibbard, “Plastic Deformation of Magnesium Single Crystals”, Metal. Trans. A, 194 (1952), pp. 295-303.
6. R.E. Reed-Hill and W.D. Bobertson, “Deformation of Magnesium Single Crystals by Nonbasal Slip”, Trans. Metall. Soc. AIME., 209 (1957) pp. 496-502.
7. B.C. Wonsiewicz and W.A. Backofen, “Plasticity of Magnesium Crystals”, Trans. AIME., 239 (1967), pp. 1422-1431.
8. E.W. Kelley and W.F. Hosford, Jr, “Pland Strain Compression of Magnesium and Magnesium Alloy Crystals”, Trans. AIME., 242 (1968), pp. 5-13.
9. T. Obara, H. Yoshinga and S. Morozumi, “$\{11\bar{2}2\}$ $<11\bar{2}3>$ Slip System

in Magnesium", Acta Metall., 21 (1973), pp. 845-853.

10. M.R. Barnett, C.H.J. Davies and X. Ma, "An Analytical Constitutive Law for Twinning Dominated Flow in Magnesium", Scripta Mater., 52 (2005), pp. 627-632.
11. S.R. Agnew and O. Duygulu, "Plastic Anisotropy and The Role of Non-basal Slip in Magnesium Alloy AZ31B", Int. J. Plasticity, 21 (2005), pp. 1161–1193.
12. W.B. Hutchinson and M.R. Barnett, "Effective Values of Critical Resolved Shear Stress for Slip in Polycrystalline Magnesium and Other HCP Metals", Scripta Mater., 63 (2010), pp. 737-740.
13. H. Miura, X. Yang, T. Sakai, H. Nogawa, S. Miura, Y. Watanabe and J. J. Jonas, "High Temperature Deformation and Extended Plasticity in Mg Single Crystals", Phil. Mag., 85 (2005), pp. 3553-3565.
14. M.Z. Bian and K. S. Shin, "Twin Interactions in Magnesium Single Crystals", DGM., 8 (2009), pp. 781-787.
15. A. Ostapovets, P. Seda, A. Jagera and P. Lejcek, "Characteristics of Coincident Site Lattice Grain Boundaries Developed during Equal Channel Angular Pressing of Magnesium Single Crystals", Scripta Mater., 64 (2011), pp. 470–473.
16. B. Bhattacharya and M. Niewczas, "Work-hardening Behaviour of Mg Single Crystals Oriented for Basal Slip", Phil. Mag., 91 (2011), pp. 2227–2247.
17. Q. Yu, J.X. Zhang and Y.Y. Jiang, "Direct Observation of Twinning–detwinning–retwinning on Magnesium Single Crystal Subjected to Strain-controlled Cyclic Tension–compression in [0 0 0 1] Direction", Phil. Mag. Lett., 91 (2011), pp. 757–765.
18. H.L. Kim, J.S. Park and Y.W. Chang, "Effects of Lattice Parameter

Changes on Critical Resolved Shear Stress and Mechanical Properties of Magnesium Binary Single Crystals", Mater. Sci. Eng. A, 540 (2012), pp. 198– 206

19. T. Al-Samman, K.D. Molodov, D.A. Molodov, G. Gottstein and S. Suwas, "Softening and Dynamic Recrystallization in Magnesium Single Crystals during C-axis Compression", Acta Mater. 60 (2012) 537-545.
20. P. Seda, A. Ostapovets, A. Jager and P. Lejcek, "Texture Evolution in Oriented Magnesium Single Crystals Processed by Equal Channel Angular Pressing", Phil. Mag., 92 (2012), pp. 1223–1237.
21. B. Fultz and J. Howe, "Transmission Electron Microscopy and Diffractometry of Materials", Springer-Verlag Berlin Heidelberg New York, 2nd Edition (2002), pp. 360-370.
22. J.F. Stohr and J.P. Poirier, "Electron Microscope Study of Pyramidal Slip. $\{11\bar{2}2\}$ $<11\bar{2}3>$ in Magnesium", Phil. Mag., 25 (1972), pp. 1313-1329.
23. S. Ando and H. Tonda, "Non-basal Slip in Magnesium-lithium Alloy Single Crystals", Trans. JIM., 41 (2000), pp. 1188-1191.
24. S. Ando, N. Harada, M. Tsushida, H. Kitahara and H. Tonda, "Temperature Dependence of Deformation Behavior in Magnesium and Magnesium Alloy Single Crystals", Key Eng. Mater., 345-346 (2007), pp. 101-104.
25. A. Styczynski, C. Hartig, J. Bohlen and D. Letzig, "Cold Rolling Textures in AZ31 Wrought Magnesium Alloy ", Scripta Mater., 50 (2004), 943-947.
26. S.R. Agnew, D.W. Brown and C.N. Tome, "Validating a Polycrystal Model for the Elastoplastic Response of Magnesium alloy AZ31 using in Situ Neutron Diffraction", Acta Mater. 54 (2006) 4841-4852.
27. J. Bohlen, M.R. Nurnberg, J.W. Senn, D. Letzig and S.R. Agnew, "The

Texture and Anisotropy of Magnesium–zinc–rare Earth Alloy Sheets", Acta Mater., 55 (2007), pp. 2101-2112.

28. Y.N. Wang and J.C. Huang, "The Role of Twinning and Untwinning in Yielding Behavior in Hot-extruded Mg–Al–Zn Alloy", Acta Mater., 55 (2007), pp. 897-905.
29. E. Schmid and W. Boas, "Plasticity of Crystals", (1950) P. Hughes, London.
30. R.A. Lebensohn and C. N. Tome, "A Self-consistent Anisotropic Approach for the Simulation of Plastic Deformation and Texture Development of Polycrystals: Application to Zirconium Alloys", Acta Metall., 41 (1993), pp. 2611-2624.
31. B. Clausen, C.N. Tome, D.W. Brown and S.R. Agnew, "Reorientation and Stress Relaxation Due to Twinning: Modeling and Experimental Characterization for Mg", Acta Mater., 56 (2008), 2456-2468.
32. C.N. Tome and R.A. Lebensohn, U.F. Kocks, "A Model for Texture Development Dominated by Deformation Twinning: Application to Zirconium Alloys", Acta Metall. Mater., 39 (1991), pp. 2667-2680.
33. A.Akhtar and E.Teghtsoonian, "Substitutional Solution Hardening of Magnesium Single Crystals", Phil. Mag., 25 (1972), pp. 897-916.
34. H. Yoshinaga and R. Horiuchi, "On the Nonbasal Slip in Magnesium Crystals", Trans. JIM., 5 (1964), pp. 14-21.
35. A. Akhtar and E. Teghtsoonian, Acta Metall., 17 (1969), pp. 1351-1356.
36. P. W. Flynn, J. Mote and J.E. Dorn, "On the Thermally Activated Mechanism of Prismatic Slip in Magnesium Single Crystals", Trans. AIME., 221 (1961), pp. 1148-1154.
37. X. Li, P. Yang, L.N. Wang, L. Meng and F. Cui, "Orientational Analysis of Static Recrystallization at Compression Twins in a Magnesium Alloy

AZ31," Mater. Sci. Eng. A, 517 (2009), pp. 160–169.

38. S.W. Xu, S. Kamado, N. Matsumoto, T. Honma and Y. Kojima, "Recrystallization Mechanism of As-cast AZ91 Magnesium Alloy during Hot Compressive Deformation", Mater. Sci. Eng. A, 527 (2009), pp. 52–60.

Chapter 4. Effects of twin on deformation behavior of Mg single crystals

4.1 Introductions

The deformation behavior of face centered cubic (FCC) and body centered cubic (BCC) metals has been studied in detail from experimental and theoretical approaches. In the case of hexagonal close-packed (HCP) metals, many fundamental problems still remain, while metals with HCP crystal structures, particularly Mg and Ti, have received a rapidly increasing attention because of their high specific-strength compared to other engineering materials [1-2]. It is known that deformation twinning occurs more frequently in HCP metals than in cubic materials and this strongly affects plastic deformation of the HCP alloys since twining can accommodate the c-axis strain, but large strains require additional deformation by slip [3]. The interactions between dislocations and twin boundaries are, therefore matters of practical interest because the deformation-induced twins may play as barriers to further slip and the source of the slip and twin dislocations at twin boundaries [4]. The criteria that a particular twin system should be operative and its crystallography; nucleation and growth mechanism of a twin lamella; interaction for twinning with crystal defects remain poorly understood. Grain refinement by recrystallization is essential for the development of the Mg alloys with high strength and good ductility [5-6]. In addition, recrystallization is often utilized to alter the detrimental strong basal texture of Mg alloys and proceed by nucleation of strain free grains and their subsequent growth until complete impingement [7-8].

The main focus of this study is to analyze the interaction between the basal slip dislocations and the $\{10\bar{1}2\}$ tensile twins and investigate the static recrystallization behavior of the $\{10\bar{1}2\}$ twins in Mg single crystals.

4.2 Results and discussion

Mg and its alloys are deformed by a combination of slip and twinning, and plastic deformations strongly influenced by mechanical twinning [9]. The activation of slip and twinning modes depend on their relative critical resolved shear stress, temperature and the orientation of the crystal with respect to the loading direction. The basal slip and $\{10\bar{1}2\}$ tensile twin are competitive and interdependent deformation modes at room temperature. The $\{10\bar{1}2\}$ twin stress is only 2~3 times greater than that of basal slip, therefore the choice depends on the loading direction. In order to study the $\{10\bar{1}2\}$ twin and basal slip interaction mechanism, two-step compression (TSC) tests were carried out on an Instron 5582 with the initial strain rate of 10^{-4}/s at room temperature as shown in Figure 4.1. The specimen was first compressed along the $[0\bar{1}10]$ direction to generate the $\{10\bar{1}2\}$ tensile twin with the crystal based upon the SF law from Table 4.1. Figure 4.2 shows typical flow curves when compression direction is along the $[0\bar{1}10]$ direction with 5MPa, 10MPa and 20MPa pre-deformation. After that, the sample was rotated 90^{o} which indicates that the compression direction is inclined 45^{o} to the [0001] axis as shown in Figure 4.1. The FLD and SLD represent the first loading direction and the second loading direction. The basal slip is known to be the dominant slip system and has the largest SF of 0.5 among those major slip systems and twinning modes as indicated in the Table 4.1. In such a case, all plastic strain can be accommodated by the single

Table 4.1 SF values for the major slip and twinning modes with first and second loading direction.

Loading Direction	Basal	Prismatic	Pyramidal I	<c+a>	$\{10\bar{1}2\}$ Tensile Twin	$\{10\bar{1}1\}$ Compressive Twin
[0 $\bar{1}$ 1 0]	0	0.43	0.38	0.33	0.50	0.42
[$\overline{40}$ 20 20 37]	0.50	0.22	0.31	0.28	0.25	0.29

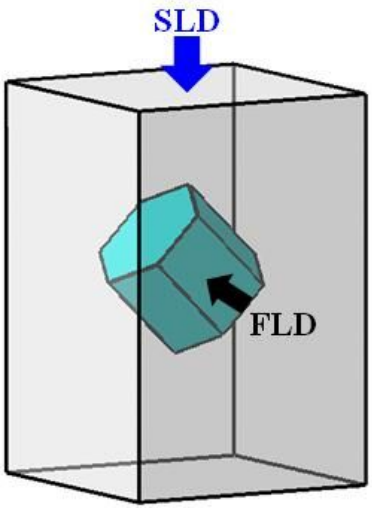

Figure 4.1 TSC test sequence. First loading direction is along the $[0\bar{1}10]$ direction to generate the $\{10\bar{1}2\}$ twin and rotated 90^{o} which indicates that the compression direction is inclined 45^{o} to the [0001] axis.

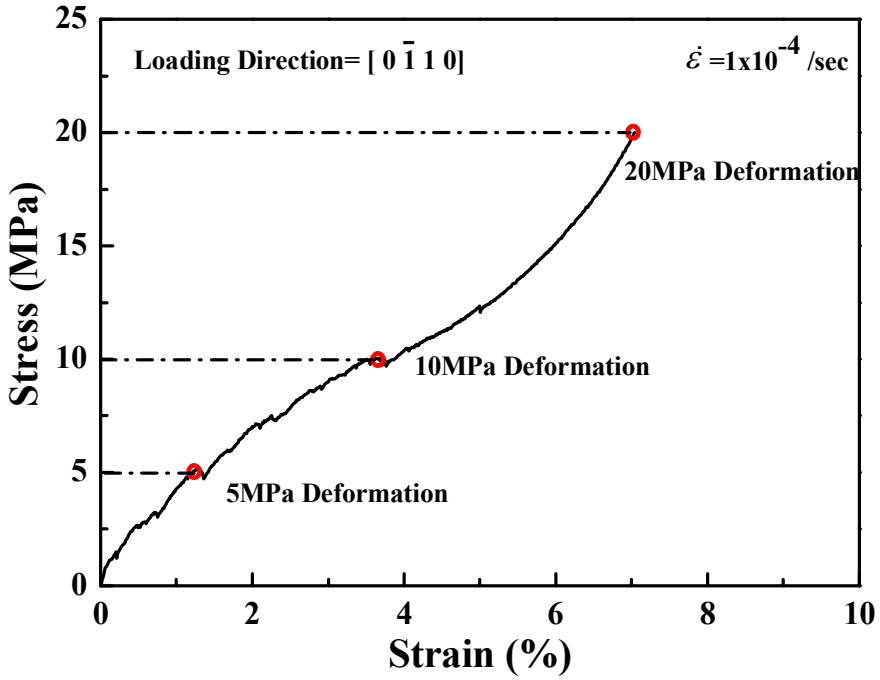

Figure 4.2 Typical flow curves when compression direction is along the [0$\bar{1}$10] direction with 5MPa, 10MPa and 20MPa pre-deformation.

active basal slip. The interaction phenomena between basal slip dislocations within the matrix and advanced $\{10\bar{1}2\}$ tensile twins is also examined.

After deformation, $\{10\bar{1}2\}$ twin traces were observed with an optical microscopy on the polished surface of the samples. Figure 4.3 (a), (b), and (c) illustrate the microstructures corresponding to the progressive deformation when compressive stress is 5MPa, 10MPa and 20MPa. The presence of twins can be clearly seen. The matrix, primary and secondary twinned crystals are labeled M, PT and ST, respectively. It is well known that the tensile twin is most commonly observed in Mg alloys and relatively easy to be activated by compression direction perpendicular to, or tension parallel to the c-axis [10]. From the Figure 4.3, the $\{10\bar{1}2\}$ twin traces were consistent with the theoretical geometric prediction when the compression direction along the $[0\bar{1}10]$ direction and all the optical micrographs presented here are taken from the sections of $(\bar{8}\ 4\ 4\ \overline{13})$ plane. In the microstructure of 5MPa deformed specimen, two wide tensile twin bands were activated. It is interesting that some very narrow secondary twins nucleated at the primary twin boundaries, which means that the primary twin boundaries act as nucleation sites for the secondary twins. When the crystal was deformed up to 20MPa, a number of the $\{10\bar{1}2\}$ twins increased dramatically, indicating that the significant twinning had begun to take place. The intersection of twins can easily be observed. When a twin is impinged by another twin, the second order twinning within the first twin is generated. Therefore, the total plastic strain can be increased considerably by the secondary twinning within the primary twinning, for example, the $\{10\bar{1}1\}$ twinning followed by the $\{10\bar{1}2\}$ twinning in Mg. In the 20MPa deformed sample, twins are impinged by other twins, however, the secondary twins within the primary twins rarely take place, which may be due to small plastic deformation.

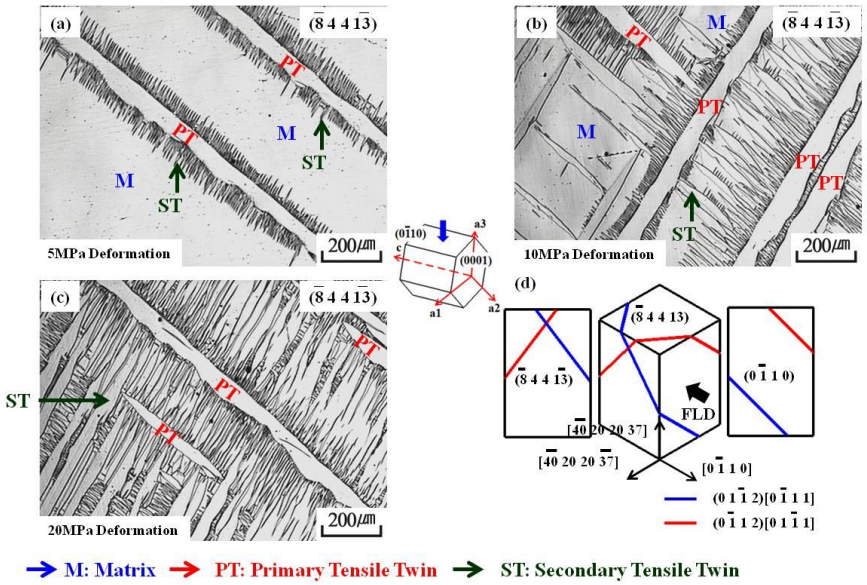

Figure 4.3 (a), (b) and (c) are corresponding to a compressive stress of 5MPa, 10MPa and 20MPa along the $[0\bar{1}10]$ direction respectively. (d) Theoretical geometric prediction of the $\{10\bar{1}2\}$ tensile twin traces.

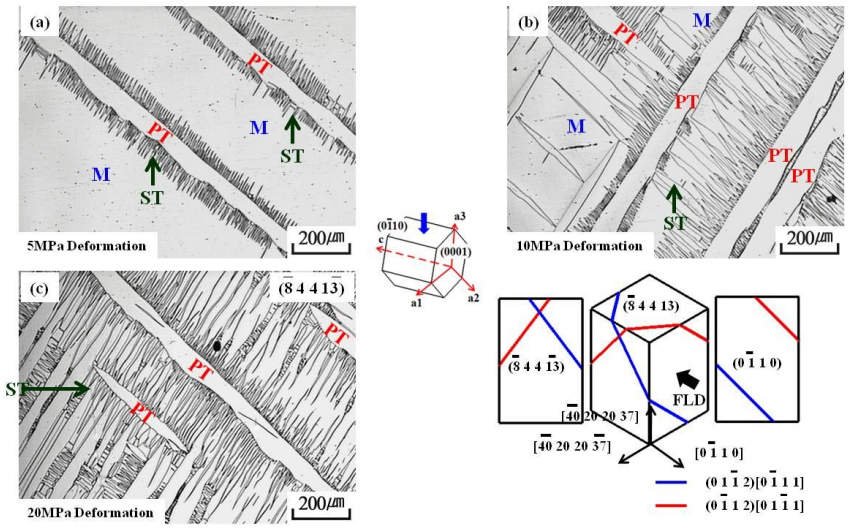

Figure 4.4 (a), (b) and (c) are corresponding to a compressive stress of 5MPa, 10MPa and 20MPa for annealed specimens. (d) Theoretical geometric prediction of the $\{10\bar{1}2\}$ tensile twin traces.

The theoretical geometric prediction of these $\{10\bar{1}2\}$ twin modes were identified from the twin trace analyses in Figure 4.3 (d). Fig. 4.4 (a), (b), and (c) show typical microstructures resulting at an early stage in sample 5MPa, 10MPa, and 20MPa pre-deformed and annealed at 623K for 2 minutes in salt bath. New grains didn't form at the $\{10\bar{1}2\}$ twins, therefore, this indicates that the tensile twins are very resistant to nucleation, which means the $\{10\bar{1}2\}$ twins are not effective in static recrystallization sites for Mg single crystals.

The effect of pre-deformation on mechanical behavior of Mg single crystal during subsequent reloading of sample (compression direction is inclined 45^o to the [0001] axis) is illustrated in Figure 4.5 (a). It can be seen that the 5MPa deformed sample caused a negligible increase of flow stress due to small volume fraction of the $\{10\bar{1}2\}$ twin. However, the 20MPa pre-deformed sample lead to dramatic increase in the flow curve that corresponds to the large $\{10\bar{1}2\}$ twin volume fraction. The strengthening from twins has generally been attributed to the apparent grain refinement effect of deformation twinning with the twin boundaries acting as obstacles to dislocations. Due to the $\{10\bar{1}2\}$ twin, the matrix was subdivided and twin boundaries played as barriers to the glide dislocations. In Figure 4.5 (b), the strain hardening rate for the without and 5MPa pre-deformed samples displays similar magnitudes, decreases continuously with strain, and plateaus at large strains, indicative of the extremely low work hardening rate, suggesting and approach to saturation stress value. In case of the 20MPa pre-deformed sample, the work hardening rate is greater than without and 5MPa pre-deformed samples, suggesting that this sample has not reached its saturation stress and has the potential for further strain hardening due to the $\{10\bar{1}2\}$ twin. These TSC results are in good agreement with slip dislocations impinging on the twin boundary and incorporated into the obstacle twin and give rise to an

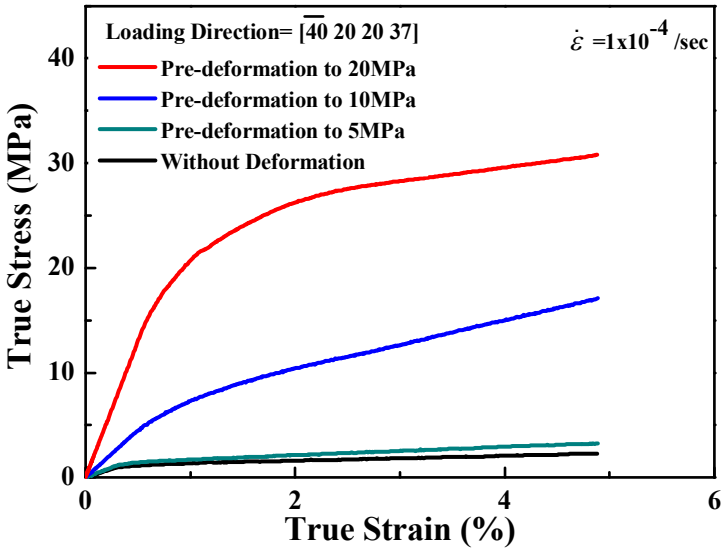

(a)

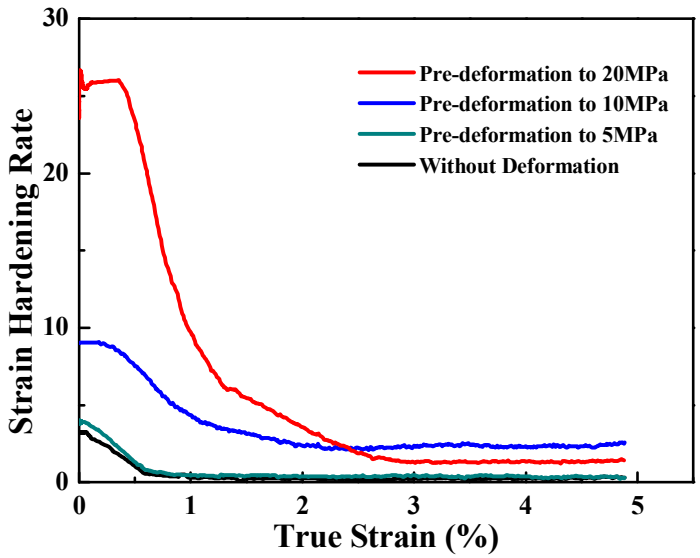

(b)

Figure 4.5 (a) Two-step compressive flow curves when compression direction is inclined 45^{o} to the [0001] axis with 5MPa, 10MPa and 20MPa deformed and no pre-deformed crystals. (b) The dependence of the strain hardening rate on imposed strain.

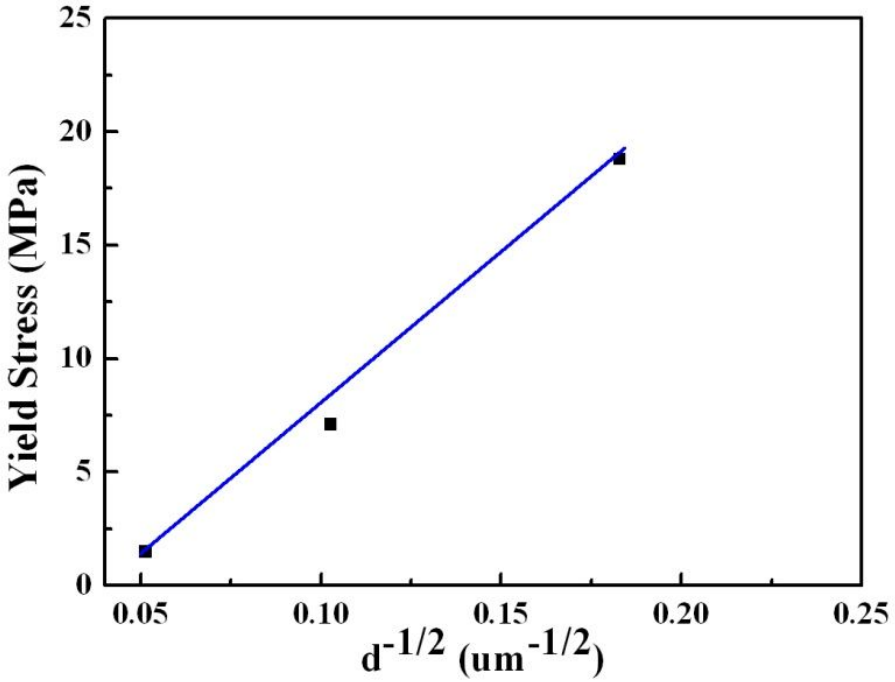

Figure 4.6 Hall-Petch plots (yield strength versus reciprocal square root of twin boundary spacing).

Table 4.2 Comparison between Hall-Petch coefficient of previously published data for polycrystalline and present work.

Material	Grain size control	Grain size (μm)	K (MPa $\mu m^{1/2}$)
Pure Mg (Poly Crystal)	Extrusion	4-63	158.11 [21]
Pure Mg (Poly Crystal)	Extrusion	10-450	126.49 [21]
Pure Mg (Single Crystal)	$\{10\bar{1}2\}$ Twin Activation	30-380	132.70 (In This Work)

increase of the flow stress. It is actually responsible for the royal mechanical properties such as nano-twinned copper and aluminum alloys [11-12]. The classical Hall–Petch relationship has been used for several decades to describe the effect of grain size on the yield stress [13–20] of polycrystalline materials as

$$\sigma_y = \sigma_0 + kd^{-1/2} \qquad (4.1)$$

where σ_y is the yield stress of a polycrystalline metal, σ_0 is often identified with yield stress relating to materials of infinite grain size, which is similar to the single crystal, k is a constant often referred to as Hall–Petch slope and it is material dependent, and d is the mean grain size. The strengthening contribution of the grain refinement by the $\{10\bar{1}2\}$ twin can also be deduced from the Hall–Petch relation, as shown in Figure 4.6. To obtain Hall–Petch slope, the yield strength values of the present work have been compared with the values available in literatures for polycrystalline pure magnesium and are presented in Table 4.2. It is clearly observed that the value of the Hall–Petch slope for Mg single crystals by the $\{10\bar{1}2\}$ twin fragmentation is similar to that of a polycrystalline pure magnesium, which implies that the strengthening mechanism in the pre-deformed specimen is due to grain refinement by the $\{10\bar{1}2\}$ twin subdivision.

The $\{10\bar{1}2\}$ twin not only acts as a barrier to slip, but also reorients matrix domains into the orientations that may or may not be favorable for the slip or twinning dislocations from experimental results. Figures 4.7 (a), (b) and (c) show the basal slip and $\{10\bar{1}2\}$ twin traces observed on the $(\bar{8}\ 4\ 4\ \bar{13})$ plane of a Mg single crystal, which was subjected to the compression direction inclined 45^o to the [0001] axis for the 5MPa, 10MPa and 20MPa pre-deformed crystals. The basal slip traces were well match with theoretical predictions in matrix regions as shown in Figure 4.7 (d). It is interesting to

notice that traces were rotated almost 90° in $\{10\bar{1}2\}$ twin regions for 5MPa and 10MPa pre-deformed specimens. On the other hand, basal slip traces were observed continuously across the $\{10\bar{1}2\}$ twin boundary in case of 20MPa pre-deformed sample. The matrix and primary twinned crystals are indicated by M and PT respectively and the line of intersection of these traces lies in the twin boundary.

For the pre-deformed specimens, the yield strength can be expressed in terms of the rule of mixture when the twin reoriented part is accommodated by the basal slip:

$$\sigma_Y = f^M \sigma_Y^M + f^T \sigma_Y^T = f^M \frac{CRSS_{Basal<a>}}{M^M} + f^T \frac{CRSS_{Basal<a>}}{M^T} \qquad 4.2$$

where σ_Y, f^M and f^T are yield strength, volume fractions of the matrix and $\{10\bar{1}2\}$ twin, respectively. Subscripts represent different types of structures: M, matrix; T, $\{10\bar{1}2\}$ twin. The M^M and M^T are Tayloy factor values of the matrix and $\{10\bar{1}2\}$ twin, respectively. The SF values of the major slip and twinning modes for reoriented regions by the $\{10\bar{1}2\}$ twin are shown in Table 4.3 and SF values for the basal slip are relatively lower than other deformation modes. Table 4.4 gives the area fractions of the matrix and twins obtained experimentally. Because it was difficult to measure the volume fractions, and thus the area fractions were used in equation 4.2. The predicted yield stress for the pre-deformed specimens using equation 4.2 is compared with the experimental measurement in Table 4.5. It should be noted that the measured yield strength is lower than predicted one for 5MPa and 10MPa pre-deformed specimens, which means the twin interfaces can be the sources of dislocations and easily activate the basal slip dislocations within the $\{10\bar{1}2\}$ twin bands. In order to identify the slip traces in the twin bands, a small region focused on the 5MPa, 10MPa pre-deformed samples were examined through the EBSD

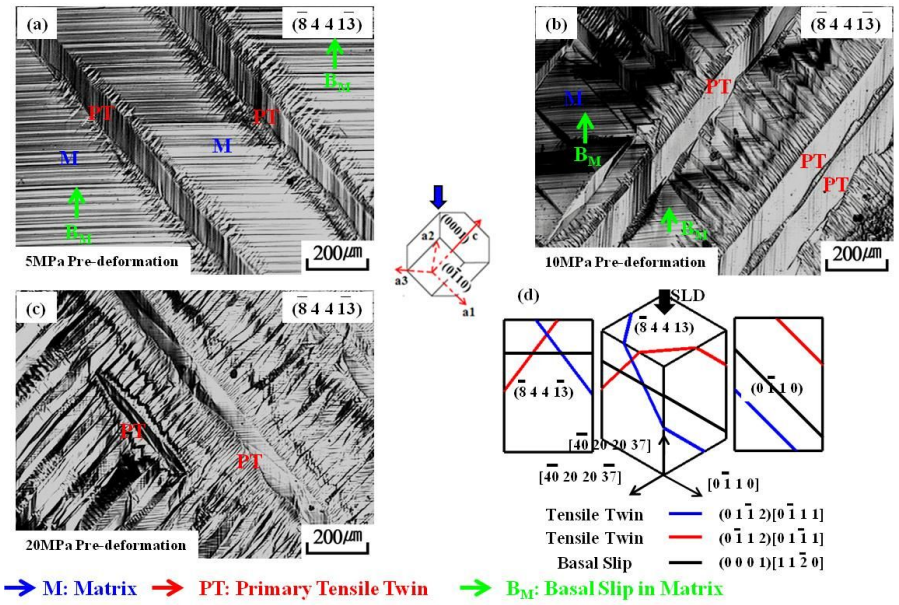

Figure 4.7 (a), (b) and (c) are microstructures taken from the sections of common ($\bar{8}$ 4 4 $\overline{13}$) plane after TSC tests. (d) Theoretical geometric prediction of the $\{10\bar{1}2\}$ tensile twin and basal slip traces.

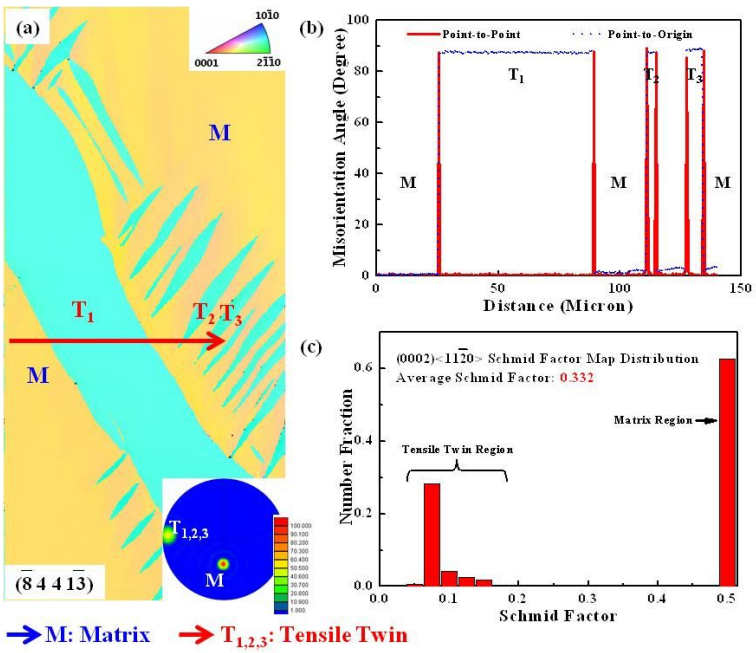

Figure 4.8 (a) Crystallographic orientation map obtained from the 5MPa pre-deformed specimen when the specimen was subjected to second loading; (b) line profile of the misorientation angle along the direction indicated as an arrow in (a). Here, M, T1, T2 and T3 represent a parent matrix and twin bands, respectively. (c) (0002) <11$\bar{2}$0> basal slip SF distribution histogram

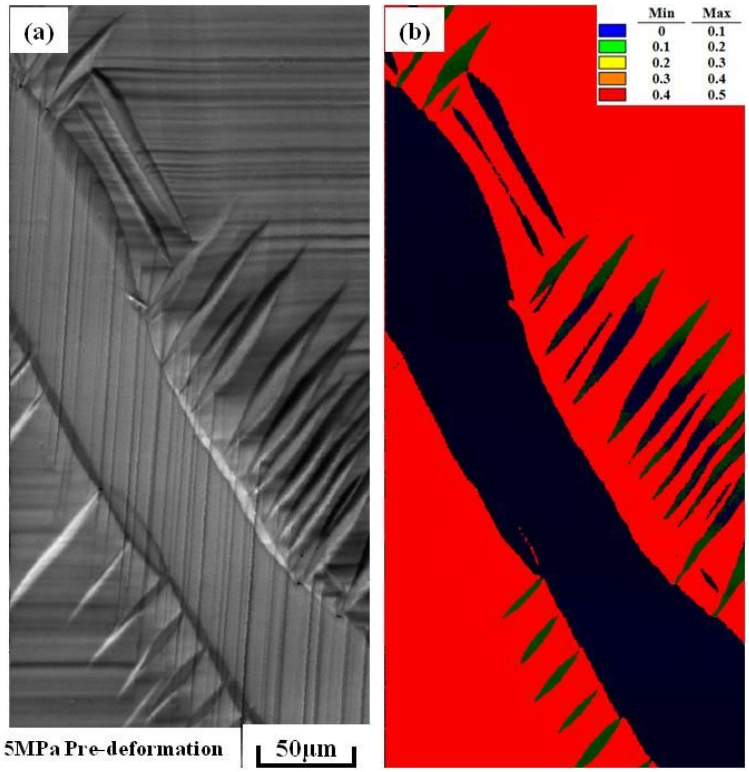

Figure 4.9 EBSD-Kikuchi band contrast map from the sections of the ($\bar{8}$ 4 4 $\overline{13}$) plane in the 5MPa pre-deformed specimen when the specimen was subjected to second loading. (b) SF map distribution for (0002) <11$\bar{2}$0> basal slip.

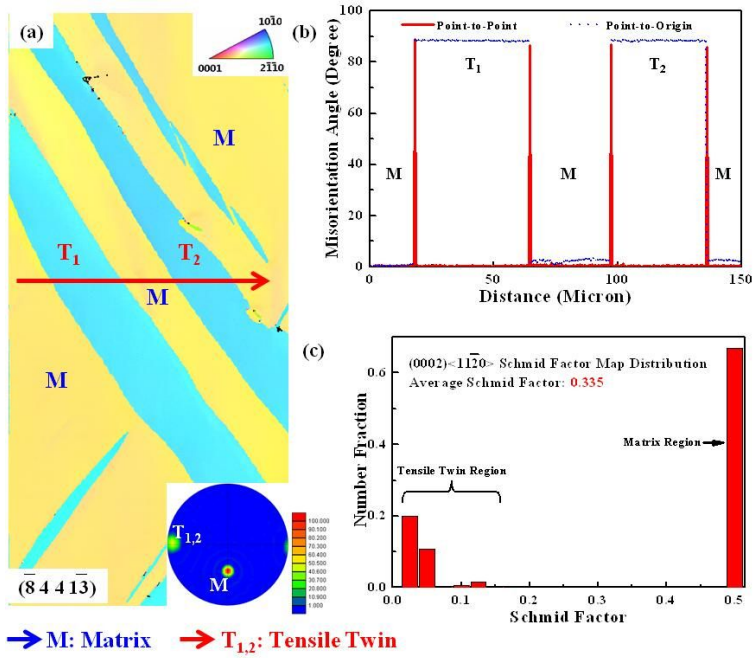

Figure 4.10 (a) Crystallographic orientation map obtained from the 10MPa pre-deformed specimen when the specimen was subjected to second loading; (b) line profile of the misorientation angle along the direction indicated as an arrow in (a). here, M, T1, T2 and T3 represent a parent matrix and twin bands, respectively. (c) SF map distribution for (0002) <11$\bar{2}$0> basal slip.

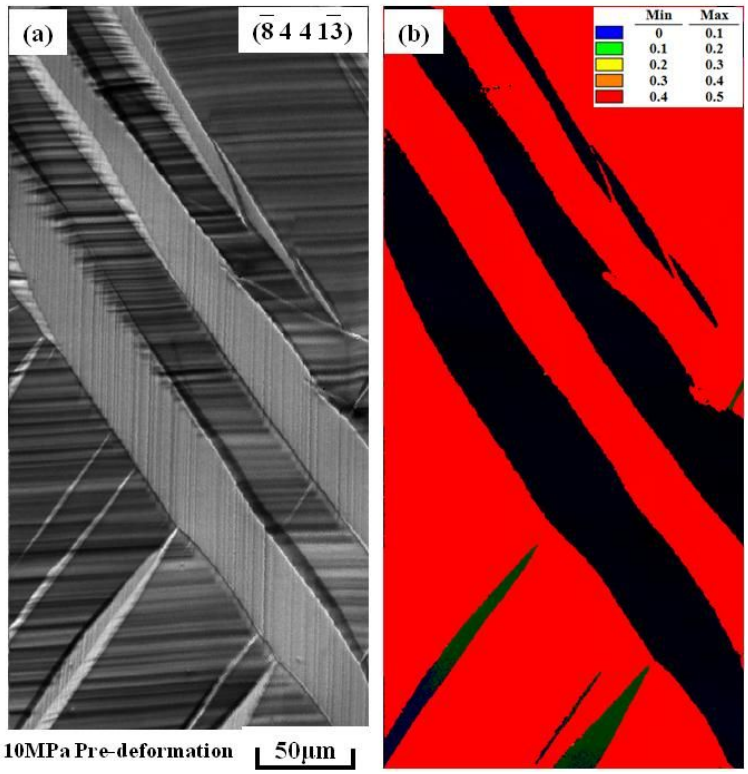

Figure 4.11 Microstructures are taken from the sections of the ($\bar{8}$ 4 4 $\bar{13}$) plane for the 10MPa pre-deformed specimen when the specimen was subjected to second loading.

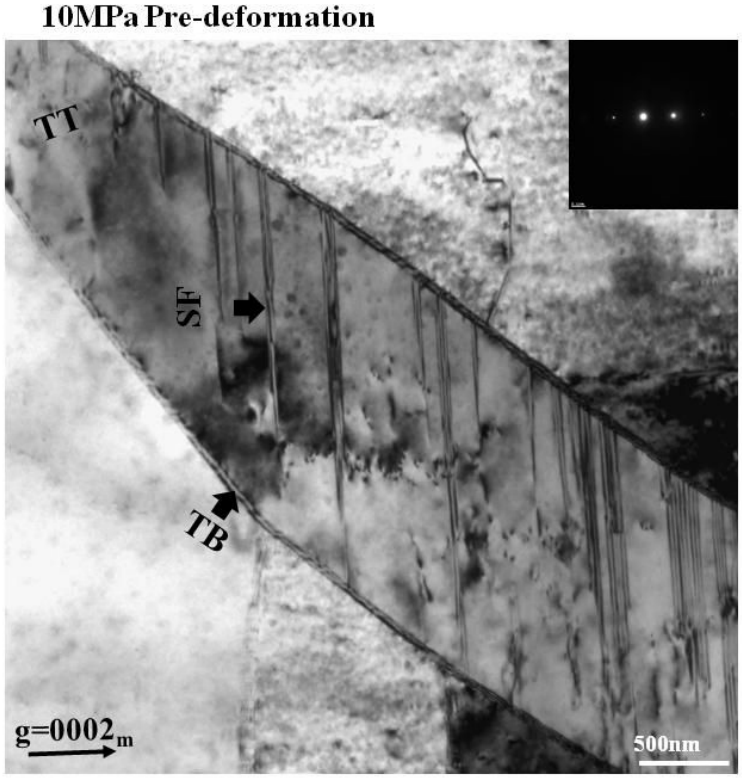

Figure 4.12 Microstructure of the 10MPa pre-deformed specimen observed with B = $[11\bar{2}0]$, g = 0002. Complicated dislocation segments and SFs within the $\{10\bar{1}2\}$ twin bands.

Table 4.3 SF values of major slip and twinning modes for reoriented regions by the $\{10\bar{1}2\}$ Twin.

Loading Direction	Basal	Prismatic	Pyramidal I	<c+a>	$\{10\bar{1}2\}$ Tensile Twin	$\{10\bar{1}1\}$ Compressive Twin
[33 90 $\overline{123}$ 5.4]	0.04	0.50	0.43	0.43	0.46	0.41

Table 4.4 Measured matrix and twin area fractions for 5MPa, 10MPa and 20MPa deformed specimens.

Pre-deformed Load (MPa)	Matrix Area Fraction (%)	Twin Area Fraction (%)
5	71.2	28.8
10	42.2	57.8
20	3.8	96.2

Table 4.5 Measured yield stress and predicted yield stress.

Pre-deformed Load (MPa)	Measured Yield Strength (MPa)	Predicted Yield Strength (MPa)
5	1.5	5.86
10	7.1	10.40
20	18.8	16.41

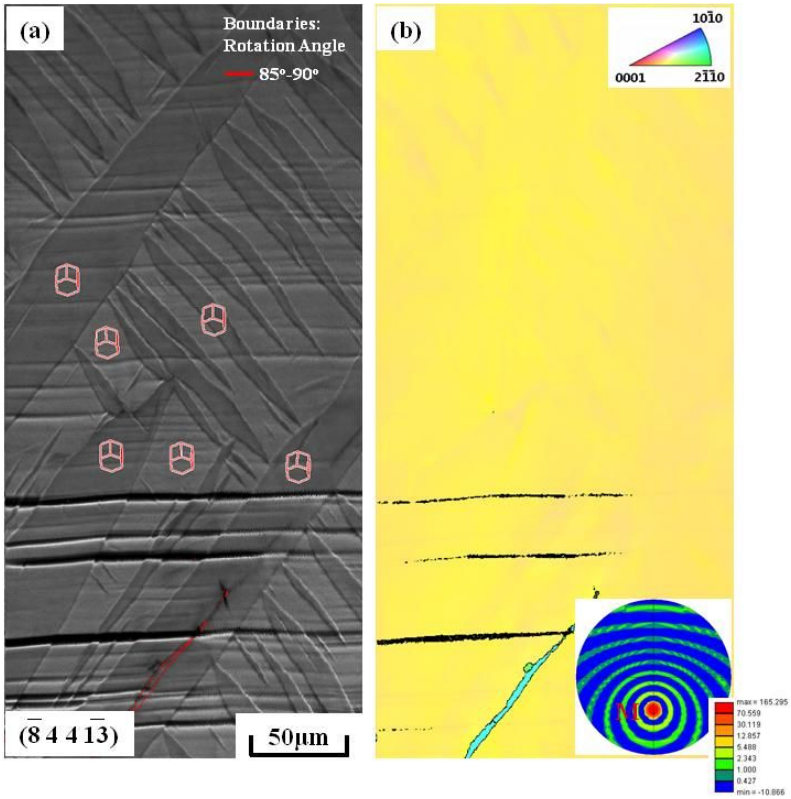

Figure 4.13 EBSD images are taken from the sections of common ($\bar{8}$ 4 4 $\overline{13}$) plane in the 20MPa pre-deformed sample when the specimen was subjected to second loading.

technique. Figure 4.8 (a) shows a crystallographic orientation map obtained from the sections of ($\bar{8}$ 4 4 $\overline{13}$) plane in 5MPa pre-deformed sample, where M and T_1, T_2 and T_3 represent parent matrix and twinned region, respectively. The line profiles of point-to-point and point-to-origin misorientation angles along the direction indicated with an arrow in Figure 4.8 (a) is presented in Figure 4.8 (b). Due to the lattice reorientation of 86.3^o caused by the $\{10\bar{1}2\}$ twinning, the misorientation angle at the boundaries between a parent matrix and twin bands were about 85-90^o. Low misorientation angle was formed within the T_1, T_2 and T_3 bands due to slip bands. Figure 4.8 (c) indicates the SF distribution histogram of (0002) <11$\bar{2}$0> basal slip of which shows two peaks: the lower one is mainly corresponding to the tensile twin region, while the higher one (SF above 0.4) is mainly corresponding to the matrix region. Figure 4.9 (a) shows the EBSD image quality (IQ) map from the sections of the ($\bar{8}$ 4 4 $\overline{13}$) plane in 5MPa pre-deformed sample. Different colors in Figure 4.9 (b) indicates the different SF value for (0002) <11$\bar{2}$0> basal slip. The twinned regions had a very low SF for (0002) <11$\bar{2}$0> basal slip, however, the basal slip was activated within tensile twin bands. Same results have been shown in Figure 4.10 and Figure 4.11 for the 10 MPa pre-deformed specimen. Both the 5MPa and 10MPa EBSD results indicate that the basal slip takes place within the primary twin bands incorporation of slip and twin boundaries. Yoo presented a comprehensive review of possible interactions of the perfect dislocations of six slip systems and the c dislocation with the several twin modes in HCP metals which have been analyzed on crystallography and elasticity theories [22-23]. Figure 4.12 image was taken with an incident electron beam direction of <11$\bar{2}$0> under the two-beam diffraction conditions, using reflections of g = 0002. It has been reported that such stacking faults are mainly observed in twins. It has been also assumed

that during deformation, twins are formed at first and then stacking faults are produced by further deformation with inter-dislocation reactions between non-basal dislocations [24-25]. As clearly seen, many stacking faults and complicated dislocation segments are also recognized within twin bands in the present study.

It is also interesting to notice that the measured yield strength is higher than the predicted one for the 20MPa pre-deformed specimen, which may be caused by the de-twinning during the second step compression. Figure 4.13 shows the image quality map and the inverse pole figure map collected from the ($\bar{8}$ 4 4 $\bar{13}$) plane and a strong indication of de-twinning process has been taken place during the second step compression. The marked area in Figure 4.13 (a) looked like twin morphology, but the boundary was not highlighted. Hexagonal unit cell orientation was indicated at the marked area and several locations. Comparison of the matrix and twinned region confirmed that the orientation of the marked areas were almost same with the initial matrix orientation, suggesting that this twin band was activated by primary loading and restored the original orientation by subsequent reloading. This provides the strong evidence that the $\{10\bar{1}2\}$ twins returns to the original orientation by de-twinning, rather than re-twinning within primary twin regions for the 20MPa pre-deformed specimen. Therefore, the basal slip traces are directly across within the twin bands without 90^{o} kink like 5MPa and 10MPa pre-deformed specimens. A Number of papers have been reported that extension twins were produced by pre-straining and progressively disappeared during reverse reloading in the Mg alloys [26-28]. It was reported that residual twins were accumulated with increasing loading cycles and the increase of residual twin boundaries caused the accumulated obstacle effect to the dislocation motion, which resulted in cyclic hardening of compressive peak stress.

Therefore, the yield stress should add the de-twinned fraction and thus equation 4.2 can be expressed as equation 4.3. The predicted value (19.97 MPa) by using equation 4.3 is higher than the measured value (18.8 MPa) with 5 MPa and 10 MPa pre-deformed specimens.

$$\sigma_Y = f^M\sigma_Y^M + f^T\sigma_Y^T + f^{DT}\sigma_Y^{DT} = f^M\frac{CRSS_{Basal}}{M_{Basal}^M} + f^T\frac{CRSS_{Basal}}{M_{Basal}^T} + f^{DT}\frac{CRSS_{Tensile\ Twin}}{M_{Tensile\ Twin}^{DT}} \quad 4.3$$

4.3 Conclusions

1) The $\{10\bar{1}2\}$ twin boundaries act as effective nucleation sites for other tensile twins.

2) The $\{10\bar{1}2\}$ twin is not an effective static recrystallization site for Mg single crystals.

3) The $\{10\bar{1}2\}$ twins act as similar effects with grain boundaries to slip dislocations and can induce a significant hardening effect. The Hall–Petch effect was observed in TSC samples.

4) Taking into account, observations from the 5MPa and 10MPa pre-deformed specimens, it can be known that slip occurs within the $\{10\bar{1}2\}$ twinned region followed by glide dislocations met with advanced twin boundaries. The intersection of glide dislocations with twin boundaries can produce basal dislocations within the primary twin bands which means twin interfaces can be the sources of dislocations.

5) The majority of the $\{10\bar{1}2\}$ twins formed during the first step compression were removed via de-twinning during the secondary step loading for the 20MPa pre-deformed specimen.

Bibliography

1. M. Hakamada, T. Furuta, Y. Chino, Y. Chen, H. Kusuda and M. Mabuchi, “Life Cycle Inventory Study on Magnesium Alloy Substitution in Vehicles”, Energy, 32 (2007), pp. 1352-1360.
2. B. Sander and D. Raabe, “Texture Inhomogeneity in a Ti–Nb-based β-Titanium Alloy after Warm Rolling and Recrystallization”, Mater. Sci. Eng. A, 479 (2008), pp. 236-247.
3. E.W. Kelley and W.F. Hosford, Jr, “Pland Strain Compression of Magnesium and Magnesium Alloy Crystals”, Trans. AIME., 242 (1968), pp. 5-13.
4. K. Ishii and H. Kibo, J. Phys. Soc. Japan, “Incorporation of Slip Dislocation in Mechanical Twins of Tin Crystals”, 18 (1963), pp. 1122-1132.
5. K. Kubota, M. Mabuchi and K. Higashi, “Processing and Mechanical Properties of Fine-grained Magnesium Alloys”, J. Mater. Sci., 34 (1999), pp. 2255-2262.
6. T. Mukai, M. Yamanoi, H. Watanabe and K. Higashi, “Effect of Grain Refinement on Tensile Ductility in ZK60 Magnesium Alloy under Dynamic Loading”, Mater. Trans., 42 (2001), pp. 1177-1181.
7. S.E. Ion, F.J. Humphreys and S.H. White, “Dynamic Recrystallisation and the Development of Microstructure during the High Temperature Deformation of Magnesium”, Acta Mater., 30 (1982), pp. 1909-1919.
8. A. Galiyev, R. Kaibyshev and G. Gottstein, “Correlation of Plastic Deformation and Dynamic Recrystallization in Magnesium Alloy ZK60”, Acta Mater., 49 (2001), pp. 1199–1207.

9. J.W. Choi and K.S. Shin, “Development of High Performance Magnesium Alloys via Microstructure and Texture Control”, Mater. Sci. Forum, 618–619 (2009), pp. 249–252.
10. Y.N. Wang and J.C. Huang, “The Role of Twinning and Untwinning in Yielding Behavior in Hot-extruded Mg–Al–Zn alloy”, Acta Mater., 55 (2007), pp. 897-905.
11. K. Lu, L. Lu and S. Suresh, “Strengthening Materials by Engineering Coherent Internal Boundaries at the Nanoscale”, Science, 324 (2009), pp. 349-352.
12. M.W. Chen, En Ma, K.J. Hemker, H.W. Sheng, Y.M Wang and X.M. Cheng, “Deformation Twinning in Nanocrystalline Aluminum”, Science, 23 (2003), pp. 1275-1277.
13. D. I. Tomsett, M. Bevis, “The Incorporation of Basal Slip Dislocations in $\{10\bar{1}2\}$ Twins in Zinc Crystals”, Phil. Mag., 19 (1969), pp. 129-140.
14. E.O. Hall, “The Deformation and Ageing of Mild Steel: III Discussion of Results”, Proc. Phys. Soc. London, 64B (1951), pp. 747-753.
15. A. Lasalmonie and J.L. Strudel, “Influence of Grain Size on the Mechanical Behaviour of Some High Strength Materials”, J. Mater. Sci., 21 (1986), pp. 1837-1852.
16. R.W. Armstrong, I. Codd, R.N. Douthwaite and N.J. Petch, “The Plastic Deformation of Polycrystalline Aggregates”, Phil. Mag., 7 (1962), pp. 45-58.
17. N. Hansen, “The Effect of Grain Size and Strain on the Tensile Flow Stress of Aluminium at Room Temperature”, Acta Metall., 35 (1977), pp. 863-869.
18. J.T. Al-Haidary, N.J. Petch and E.R. de los Rios, “The Plastic Deformation of Polycrystals I. Aluminium between Room Temperature

and 400°C", Phil. Mag., 47 (1983), pp. 869-890.

19. L.L. Shaw, A.L. Ortiz and J.C. Villegas, "Hall–Petch Relationship in a Nanotwinned Nickel Alloy", Scripta Mater., 58 (2008), pp. 951-954
20. S.M. Razavi, D.C. Foley, I. Karaman, K.T. Hartwig, O. Duygulu, L.J. Kecskes, S.N. Mathaudhu and V.H. Hammond, "Effect of Grain Size on Prismatic Slip in Mg–3Al–1Zn Alloy", Scripta Mater., 66 (2012) pp. 439–442.
21. D.V. Wilson and J.A. Chapman, "Effects of Preferred Orientation on the Grain Size Dependence of Yield Strength in Metals", Phil. Mag., 8 (1963), pp. 1543–1551.
22. M. H. Yoo, "Interaction of Slip Dislocations with Twins in HCP Metals", Trans. Trans. Metall. Soc. A, 245 (1969), pp. 2051-2060.
23. M. H. Yoo, "Slip, Twinning, and Fracture in Hexagonal Close-Packed Metals", Metal. Trans. A, 12 (1981), pp. 409-418.
24. S.R. Agnew, J.A. Horton and M.H. Yoo, "Transmission Electron Microscopy Investigation of <c+a> Dislocations in Mg and a–Solid Solution Mg-Li Alloys", Metall. Mater. Trans. A, 33 (2002), pp. 851–858.
25. B. Li, P.F. Yan, M.L. Sui and E. Ma, "Transmission Electron Microscopy Study of Stacking Faults and Their Interaction with Pyramidal Dislocations in Deformed Mg", Acta Mater., 58 (2010), pp. 173–179.
26. R.H. Wagoner, X.Y. Lou, M. Li and S.R. Agnew, "Forming Behavior of Magnesium Sheet", J. Mater. Pro. Tech., 177 (2006), pp. 483-485.
27. X.Y. Lou, M. Li, R.K. Boger, S.R. Agnew and R.H. Wagoner, "Hardening Evolution of AZ31B Mg Sheet", Int. J. Plast., 23 (2007), pp. 44-86.

28. L. Wu, A. Jain, D.W. Brown, G.M. Stoica, S.R. Agnew, B. Clausen, D.E. Fielden and P.K. Liaw, “Twinning–detwinning Behavior during the Strain-controlled Low-cycle Fatigue Testing of a Wrought Magnesium Alloy, ZK60A”, Acta Meter., 56 (2008), pp. 688-695.

Chapter 5. Orientation effects on relative activity of slip and twinning in Mg single crystals

5.1 Introductions

A strong basal texture, in which the c-axis of grains aligns parallel with the direction of compressive strain, is developed in wrought Mg and its alloys [1-2]. This result is related to the activation of the basal slip that tends to rotate the (0002) plane towards the loading direction, developing the basal texture in the conventional process [3]. Unfortunately, the strong basal texture exhibits poor formability at ambient temperature due to the limited number of active slip systems and subsequently leads to restrictions in their wide applications. Recently, many works have been performed to understand the texture evolution mechanisms because weakened or random textures are known to improve the formability [4-5]. It has been shown that several alloy elements could lead to weakening basal texture, for example, rare earth (RE) and calcium (Ca) elements [6-8]. However, there is still a lack of understanding why these elements can alter the texture drastically while other elements such as Al and Zn do not. On the other hand, several methods based on severe plastic deformation have allowed engineering of modifying textures. AZ31 shows exceptionally ductile properties at room temperature through texture control using the equal-channel angular pressing (ECAP) technique, a tilted (0002) basal texture was rotated 45° with the extrusion direction and thus the relative activity of basal slip has increased significantly [9]. Kim developed the high-speed-ratio differential speed rolling (HRDSR) technique to induce a large shear deformation during rolling. By using this technique, an

ultrafine-grained microstructure with a low intensity of basal texture could be obtained, leading to production of Mg alloy sheets with high strength and good formability [10]. Furthermore, controlling recrystallization and grain growth could also be utilized to change the harmful basal texture. From the literatures, it was reported that both static recrystallization and dynamic recrystallization mechanisms were usually used to explain the experimental observations of DRX in Mg alloys [11-12]. Both of static and dynamic recrystallization mechanisms can give rise to continuous and/or discontinuous recrystallization. While continuous recrystallization does not cause a significant alteration of the original texture, however the discontinuous recrystallization is usually associated with an appreciable modification of the texture [13-14].

To date, there are so several works that have been carried out to modify the strong basal texture, which means spreading the basal planes from sheets normal direction. However, it is still lack of understanding what kind of textures are the desired textures because systematic researches regarding the effects of the initial orientation on the mechanical behaviors have been rarely reported. In this study, 11 samples were prepared from basal plane to prismatic plane at the interval of 10°, with an additional 45°. The purpose is to characterize the effects of the initial orientation on the mechanical behaviors and subsequently evaluate the major deformation modes with corresponding orientations.

5.2 Results and discussion

In order to cover a wide range of investigations, 11 specimens with different loading orientations ranging between the [0002] and $[10\bar{1}0]$ directions were prepared, as shown in Figure 5.1. The result of the true stress-

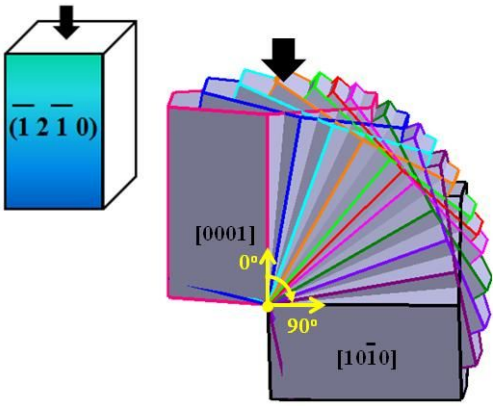

Figure 5.1 Schematic diagram showing the 11 different orientations used in uni-axial compression tests.

Table 5.1 The compression direction for corresponding rotation angles.

Rotation Angle (Degree)	Loading Direction
0	[0 0 0 1]
10	[191 0 $\overline{191}$ 1155]
20	[376 0 $\overline{376}$ 1102]
30	[549 0 $\overline{549}$ 898]
40	[706 0 $\overline{706}$ 898]
45	[777 0 $\overline{777}$ 829]
50	[842 0 $\overline{842}$ 754]
60	[952 0 $\overline{952}$ 586]
70	[1032 0 $\overline{1032}$ 401]
80	[1083 0 $\overline{1083}$ 204]
90	[1 0 $\bar{1}$ 0]

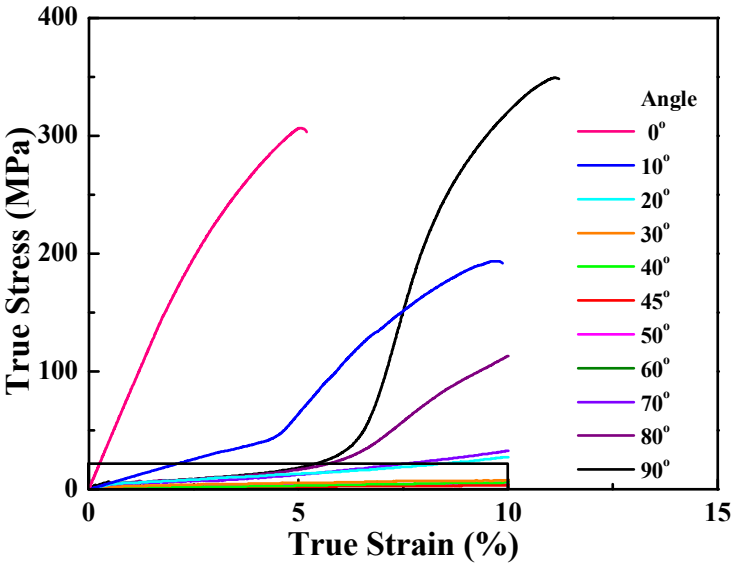

(a)

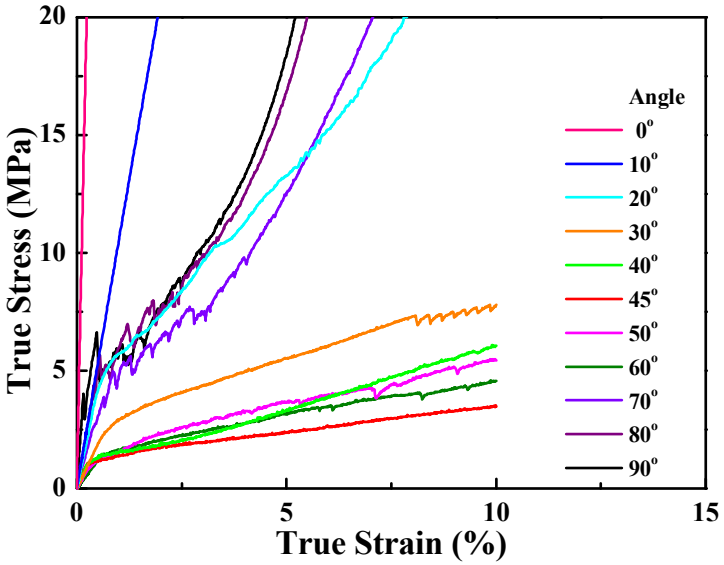

(b)

Figure 5.2 (a) True stress-strain curves for Mg single crystals deformed at room temperature. (b) Enlargement of the marked box in the bottom left corner in (a).

strain curves for 11 different orientations is illustrated in Figure 5.2.

High magnification of the rectangular box located at the bottom of the graph in Figure 5.2 (a) is shown in Figure 5.2 (b). Significant differences were observed among those specimens, indicating the contributions of deformation modes have been changed during the plastic deformation. The detailed information about the compression direction for the corresponding rotation angle is shown in Table 5.1. When the specimen was compressed along the [0002] direction, the initial flow stress rapidly increased, followed by a fracture at around 6% true strain. This is postulated to be the effects of <c+a> slip which has been reported by many researchers previously [15-17]. As the compression direction inclines 10° from the c-axis, the initial slope is much lower than 0° and the significant increase in flow stress could be observed when the deformation proceeded from 4% true strain. The flow stress drops dramatically as the rotation angle climbs to 20°. With the further increase of the rotation angle, the stress value decreases negligibly small and displays similar magnitudes, indicating the extremely low work hardening rate. Thus, suggesting that the basal slip is potentially a dominant mode in range of 30 to 60°. From 70° onwards, the flow curves exhibits a reverse trend where the flow stress increases with the rotation angle increases. When compressed along the $[10\bar{1}0]$ direction, the work hardening rate is relatively small at low strains, which is followed by a significant increase until it reaches the peak value before fracture. Such observations can be explained by the deformation process that the crystals rotate until reached about 6% strain, which is known to be a $\{10\bar{1}2\}$ twin-dominated condition. In this case, the reoriented orientation is difficult to activate a basal slip and as a consequence the material hardens dramatically [18].

After deformation, microstructures were directly taken without further

treatments including polishing and etching, since they can remove any trace of the slip steps. Surface steps were clearly presented at the $(\bar{1}2\bar{1}0)$ plane as shown in Figure 5.3. Trace predictions are based on the SF calculation and the active basal slip and $\{10\bar{1}2\}$ twin system are located in the left corner of corresponding microstructure. It is generally known that the $\{10\bar{1}2\}$ twin is easily activated by compression at the direction perpendicular to, or tension parallel to the c-axis for the geometric reason [19]. In other words, the $\{10\bar{1}2\}$ twin could not occur when the crystals were compressed along the c-axis. However, the $\{10\bar{1}2\}$ twin traces were found in the microstructure and this is presumably due to the residual stress during deformation [20]. The corresponding pole figure in Figure 5.4 indicate that the texture characteristic retains almost the same as the original one, which means the $\{10\bar{1}2\}$ twin does not play a dominant role in the deformation. The $\{10\bar{1}2\}$ twin traces were also observed for the 10° rotated sample as well as the 0^o sample. However, the texture difference between the initial and deformed samples is negligibly small. The $\{10\bar{1}2\}$ twin traces were barely shown, while fine basal slip traces were clearly observable from 20 to 80°. Overall, basal slip traces covered the entire sample surface between 40 to 50°, which implies deformation is mainly attributed to basal slip. The $\{10\bar{1}2\}$ twin morphologies only started to appear in the sample from 60° onwards and finally at 90° rough surface steps were seen. In general, only minor differences occurred between the initial and deformed samples from 0 to 60° revealing the importance of slip as a major deformation mode. In contrast, deformed samples rotated almost 90° with the initial texture for the rest of samples, due to the $\{10\bar{1}2\}$ twin, induced a crystallographic lattice reorientation.

As described above, different microstructures and textures were

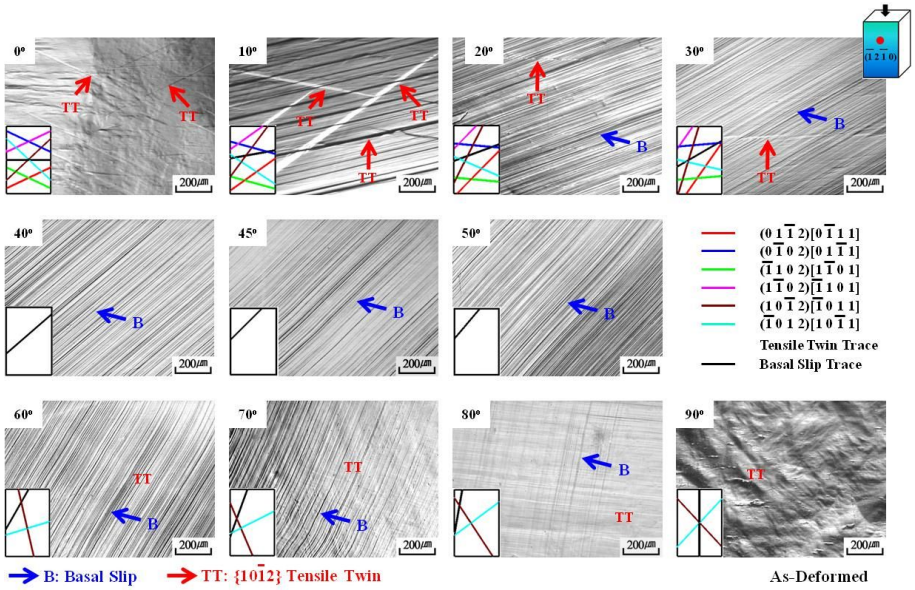

Figure 5.3 Microstructures are taken from the sections of the ($\bar{1}2\bar{1}0$) plane.

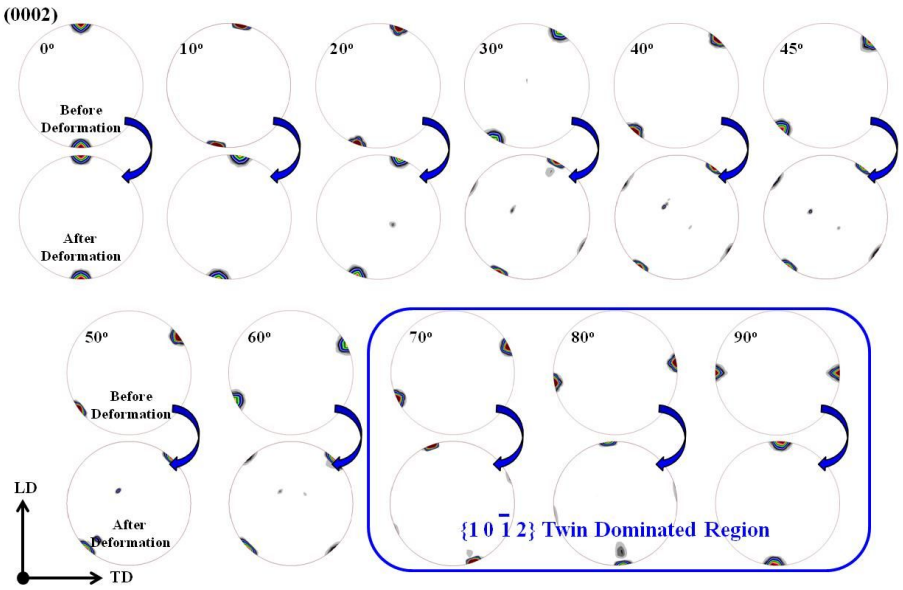

Figure 5.4 The (0002) basal pole figures for the initial and deformed samples.

evolved depending on the orientation is attributed to the different deformation modes. The SF analysis was carried out on the <a> type, <c+a> slip and twin modes, as shown in Figure 5.5. When compressed along the c-axis, the SF values for the <a> type slip modes are all 0. Therefore, the initial texture was hardly oriented for all <a> type deformations and thus the <c+a> slip and $\{10\bar{1}1\}$ twin may become favorable based upon the SF calculation. The contribution from the $\{10\bar{1}2\}$ twin is negligibly small from the pole figure data as illustrated in Figure 5.4 even with the high SF value. As an anisotropic material, the activation of each deformation mode is not only determined by the SF, but also strongly affected by the critical resolved shear stress (CRSS) value, because the CRSS value for various deformation modes differ significantly [21-22]. Figure 5.6 reveals the stress required (CRSS/SF) to activate major deformation modes. The CRSS values employed to generate these plots are derived from experimental and VPSC simulations [23]. Blue symbols are the yield strength for corresponding orientations. For the 0° rotated sample, the <c+a> slip is main deformation modes, as expected. The stress value required for the $\{10\bar{1}2\}$ twin is lower than the yield stress for 0° rotated sample. However, due to the initial orientation effects, the $\{10\bar{1}2\}$ twin does not contribute to the plastic deformation. Since the CRSS for basal slip is very low, a slight misalignment of the specimen could easily lead to the occurrence of basal slip. It is apparent that the stress required to activate the basal slip is lower than the experimental results between 10 and 60°. This fact indicates that the basal slip plays a meaningful role in the deformation. From 70 to 90°, the yield strength is well matched with the calculated value for the $\{10\bar{1}2\}$ twin. Therefore, the $\{10\bar{1}2\}$ twin is very much likely to contribute to the initial deformation range. XRD pole figure data also provides clear evidence for the abrupt orientation change due to twinning.

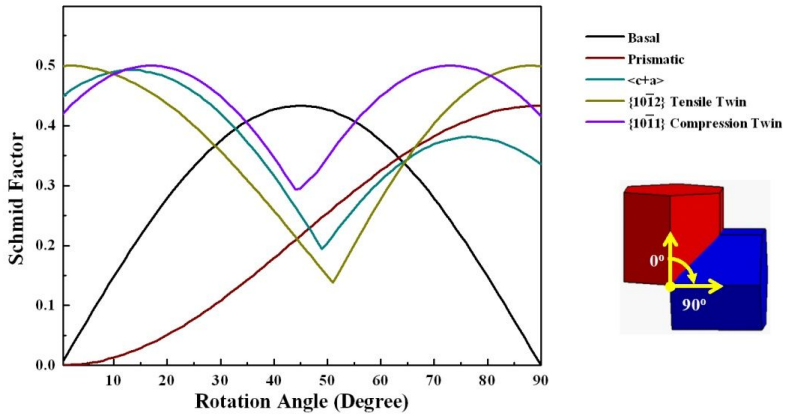

Figure 5.5 SF calculations for the <a> type, <c+a> type slip systems and twin modes.

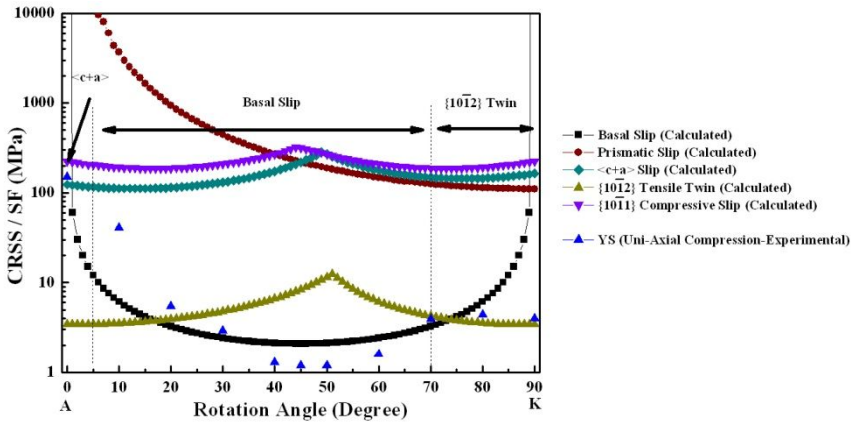

Figure 5.6 Stress (CRSS/SF) required to activate the <a> type, <c+a> type slip systems and twin modes.

5.3 Conclusions

In summary, the stresses of various deformation modes strongly rely on the direction of the applied force, particularly with respect to the c axis. Owing to the limited number of deformation modes, Mg single crystals with certain orientations present a pronounced tendency to geometrical hardening or softening. Therefore, it can be concluded that activities of slips and twinning are systematically different from the experiment results and analysis at 11 different orientations. In case of the 0° rotated samples, <c+a> slip is adapted to rationalize the high yield strength compared to other orientations. Basal slip plays an important role in the samples with rotation angles ranging from 10 - 60° with respect to the c-axis. In addition, $\{10\bar{1}2\}$ twin dominates the initial part of deformation for the 70 - 90° rotated samples. These results have given us insight into the effect of initial orientation on deformation behavior in Mg single crystals and will help us to design the desired texture in Mg and its alloys.

Bibliography

1. S.A. Farzadfar, E. Martin, M. Sanjari, E. Essadiqi, M.A. Wells and S. Yue, "On the Deformation, Recrystallization and Texture of Hot-rolled Mg–2.9Y and Mg–2.9Zn Solid Solution Alloys-A Comparative Study", Mater. Sci. Eng. A, 534 (2012), pp. 209-219.
2. X.S. Huang, K. Suzuki, Y. Chino and M. Mabuchi, "Influence of Initial Texture on Rolling and Annealing Textures of Mg–3Al–1Zn Alloy Sheets Processed by High Temperature Rolling", J. Alloy Compd., 537 (2012), pp. 80–86.
3. S.R. Agnew, M.H. Yoo and C.N. Tome, "Application of Texture Simulation to Understanding Mechanical Behavior of Mg and Solid Solution Alloys Containing Li or Y", Acta Metall., 49 (2001), pp. 4277-4289.
4. S.R. Agnew and J.F. Nie, "Preface to the Viewpoint Set on: The Current State of Magnesium Alloy Science and Technology", Scripta Mater., 63 (2010), pp. 671-673.
5. M.R. Barnett, A. Sullivan, N. Stanford, N. Ross and A. Beer, "Texture Selection Mechanisms in Uniaxially Extruded Magnesium Alloys", Scripta Mater., 63 (2010), pp. 721-724.
6. L.W.F. Mackenzie and M. Pekguleryuz, "The Influences of Alloying Additions and Processing Parameters on the Rolling Microstructures and Textures of Magnesium Alloys", Mater. Sci. Eng. A, 480 (2008), pp. 189-197.
7. R.K. Mishra, A.K. Gupta, P.R. Rao, A.K. Sachdev, A.M. Kumar and A.A. Luo, "Influence of Cerium on the Texture and Ductility of

Magnesium Extrusions", Scripta Mater., 59 (2008), pp. 562-565.

8. N. Stanford, "Micro-alloying Mg with Y, Ce, Gd and La for Texture Modification—A Comparative Study", Mater. Sci. Eng. A, 527 (2010), pp. 2669-2677.
9. T. Mukai, M. Yamanoi, H. Watanabe and K. Higashi, "Ductility Enhancement in AZ31 Magnesium Alloy by Controlling Its Grain Structure", Scripta Mater., 45 (2001), pp. 89-94.
10. W.J. Kim, H.G. Jeong and H.T. Jeong, "Achieving High Strength and High Ductility in Magnesium Alloys using Severe Plastic Deformation Combined with Low-temperature Aging", Scripta Mater., 61 (2009), pp. 1040-1043.
11. H.Y. Chao, H.F. Sun, W.Z. Chen and E.D. Wang, "Static Recrystallization Kinetics of a Heavily Cold Drawn AZ31 Magnesium Alloy under Annealing Treatment", Mater. Character., 62, (2011), pp. 312-320.
12. R. Bhattacharya, B.P. Wynne and W.M. Rainforth, "Flow Softening Behavior during Dynamic Recrystallization in Mg–3Al–1Zn Magnesium Alloy", Scripta Mater., 67 (2012), pp. 277–280.
13. S.E. Ion, F.J. Humphreys and S.H. White, "Dynamic Recrystallisation and the Development of Microstructure during the High Temperature Deformation of Magnesium", Acta Mater., 30 (1982), pp. 1909-1919.
14. F.J. Humphreys and M. Hatherly, "Recrystallization and Related Annealing Phenomena", Elsevier, 2nd Edition (2004), p. 293, 301, 417.
15. T. Obara, H. Yoshinga and S. Morozumi, "$\{11\bar{2}2\}<\bar{1}\bar{1}23>$ Slip System in Magnesium", Acta Metall., 21 (1973), pp. 845-853.
16. H. Yoshinaga and R. Horiuchi, "Deformation Mechanisms in Magnesium Single Crystals Compressed in the Direction Parallel to

Hexagonal Axis", Trans JIM., 4 (1963), pp. 1-8.

17. S. Ando, N. Harada, M. Tsushida,H. Kitahara and H. Tonda, "Temperature Dependence of Deformation Behavior in Magnesium and Magnesium Alloy Single Crystals", Key Eng. Mater., 345-346 (2007), pp. 101-104.
18. E.W. Kelley and W.F. Hosford, Jr, "Pland Strain Compression of Magnesium and Magnesium Alloy Crystals", Trans. AIME., 242 (1968), pp. 5-13.
19. Y.N. Wang and J.C. Huang, "The Role of Twinning and Untwinning in Yielding Behavior in Hot-extruded Mg–Al–Zn Alloy", Acta Mater., 55 (2007), pp. 897-905.
20. B.C. Wonsiewicz and W.A. Backofen, "Plasticity of Magnesium Crystals", Trans. AIME., 239 (1967), pp. 1422-1431.
21. A. Chapuis and J.H. Driver, "Temperature Dependency of Slip and Twinning in Plane Strain Compressed Magnesium Single Crystals", Acta Mater., 59 (2011), pp. 1986-1994.
22. P.G. Partridge, "The Crystallography and Deformation Modes of Hexagonal close-packed Metals", Met. Rev., 12 (1967), pp. 169-194.
23. M.Z. Bian and K.S. Shin, (2012), Unpublished Work.

Chapter 6. Interaction between dislocation and tensile twin in Mg single crystals

6.1 Introductions

Magnesium (Mg) alloys have a limited number of independent slip modes for dislocation glide and consequently deformation twinning plays an important role in plastic deformation at room temperature (RT) [1-3]. Deformation twinning usually takes place on the first or second order pyramidal planes in twinning directions and also provides the needed c-axis strain component for general deformation [4]. Various types of twin modes were reported in previous studies, such as the $\{10\bar{1}1\}$, $\{10\bar{1}2\}$, $\{10\bar{1}3\}$, $\{10\bar{1}5\}$, $\{11\bar{2}4\}$, $\{30\bar{3}2\}$ and $\{30\bar{3}4\}$ twin modes, which took place on pyramidal planes [5-8]. Double twinning modes of the $\{10\bar{1}1\}$-$\{10\bar{1}2\}$, $\{10\bar{1}3\}$-$\{10\bar{1}2\}$ and $\{10\bar{1}2\}$-$\{10\bar{1}2\}$ types were found to have a particular feature with the $\{10\bar{1}2\}$ twinning in the interior and preferential alignment of primary twins [9-11]. Among them, the $\{10\bar{1}2\}$ and $\{10\bar{1}1\}$ twins have been commonly observed twin modes in Mg and its alloys. The stress value for the $\{10\bar{1}2\}$ and $\{10\bar{1}1\}$ twins were reported to be 2~3MPa and 76~153MPa [12], respectively, even the shear strains produced by both twins were roughly similar (0.1289 and 0.1377) [4]. Hence, the $\{10\bar{1}2\}$ twin has the higher activation chance compared with the $\{10\bar{1}1\}$ twin, and consequently the interaction between the $\{10\bar{1}2\}$ twin and basal slip dislocations is unavoidable [13-16]. Therefore the interactions between dislocations and twin boundaries are, matters of practical interests because the deformation-induced twins may

play as barriers to further slip and the source of the slip and twin dislocations at twin boundaries. However, despite several decades of research, the mechanisms involved in the interactions between slip and twinning have poorly been understood in hexagonal close-packed (HCP) crystals because the HCP structure is more difficult and complicated compared with those of high symmetry structures.

Price [17] has observed the interaction of slip dislocations with a twin boundary and proposed possible reactions giving rise to the transmission of slip dislocations in the twinned crystal producing a residual twinning dislocation in a zinc crystal. Yoo and Wei [18] have given a formalism to transform lattice vectors into twinned crystal vectors and systematically calculated the residual twinning vector. Lay and Nouet [19] have carried out the detailed TEM and high-resolution electron microscopy (HREM) analysis of the interaction of lattice dislocations with the $\{10\bar{1}2\}$ twin interface in zinc. More recently, Serra et al. [20-23] have focused on dislocation reactions at twin boundaries by atomic-scale computer simulation techniques. They showed that when a shear stress resolved for basal slip was applied to a $\{10\bar{1}2\}$ twinned crystal, screw dislocations with Burgers vector and line direction parallel to the boundary were able to cross the twin boundary, and no residual dislocations were left behind.

The main objective is to understand the interactions between various deformation modes and $\{10\bar{1}2\}$ tensile twin in a Mg crystal. Twinning has a polar nature, which means that the twinning in magnesium can only be accommodated when the c-axis is elongated or contracted [7]. Therefore, the activation of corresponding twinning mode is highly dependent on crystal orientation (texture) [24]. Many works have been carried out to investigate the $\{10\bar{1}2\}$ twin effects by using compression tests along the extrusion direction

[25-27]. However, it could not give information about the interaction between $\{10\bar{1}2\}$ twin and specific deformation modes, since various deformation modes simultaneously contributed to the in the later stage of deformation. More intricately, due to the influence of grain boundaries, the intrinsic twin and slip interaction behavior can be rather complicated to analyze in the case of polycrystalline materials. Therefore, it is intriguing to study the twin–slip or twin-twin interaction process by using single crystals. In this study, Mg single crystals were adopted to systematically investigate the twinning effects on the mechanical properties through TSC tests. By using TSC test, twin and slip modes could be separated. Because of the low symmetry of crystal structure, application of load in one direction could activate twin only, while load in another direction could activate the slip and twinning modes. These works generally assumed the Schmid's law for the twinning, which means predominant twin modes activated for the highest Schmid factor among all other twin variants. Optical microscopy and TEM were used to observe microstructures and EBSD was employed for orientation analysis.

6.2 Results and discussion

In order to observe the interactions of the $\{10\bar{1}2\}$ twin with the various slip and twinning modes, single crystal specimens with eleven different rotation angles of the plane normal were prepared from the [0001] direction to the $[10\bar{1}0]$ direction at an interval of 10^{o} and one more orientation from 45^{o}. The TSC tests were employed to evaluate the mechanical behavior of Mg single crystals with an initial strain rate of $1x10^{-4}$/sec at room temperature. The schematic diagram of TSC test is shown in Figure 6.1. The FCD and SCD represent the first and second compression directions, respectively. It is known that the activation of twins at the onset of plastic deformation strongly

depends on the twin stress, temperature, and orientation of the crystal with respect to the loading direction [28-30]. In order to activate the $\{10\bar{1}2\}$ twin, eleven specimens were first compressed along the $[\bar{1}2\bar{1}0]$ direction up to 10MPa at room temperature. Typical stress-strain curves are shown in Figure 6.2, and stress drops are observed during deformation which is known as a characteristic of twin dominated flow curve [31]. A stress drop on the stress–strain curve corresponded to the generation of fresh twins. The careful examination of the stress–strain curve reveals that specimens started to exhibit the serrated flow behavior at a stress range of 3.45 – 6.43 MPa. Knowing that the SF of $\{10\bar{1}2\}<\bar{1}011>$ twin system is 0.37 for the compression direction along the $[\bar{1}2\bar{1}0]$ direction (Table 6.1), the onset stress for $\{10\bar{1}2\}$ twining is identified to be around 1.28 – 2.38 MPa which is close to the reported value.

After deformation, microstructures were taken directly without further treatments since they could remove trace of the slip steps and twin traces were clearly observable in Figure 6.3. Theoretically, a $\{10\bar{1}2\}$ twinning possibly occurs on six equivalent variant planes with a specific shear direction of $<10\bar{1}1>$. In the case of the FCD, four equally favored $\{10\bar{1}2\}$ twinning systems had the same Schmid factor value of 0.37 and the corresponding twin variants were activated. Detailed information about Schmid factor analysis on six variant twin modes is listed in Table 6.2. Trace predictions for six $\{10\bar{1}2\}$ twin variants are located in left corner of corresponding specimens. Horizontal twin traces $((10\bar{1}2)[\bar{1}011]$ and $(\bar{1}012)[10\bar{1}1]$ twin modes) were missing for all the specimens since Schmid factor value was 0 for both of two. From Figure 6.3, $\{10\bar{1}2\}$ twin traces showed good agreement with the theoretical geometric predictions when the compression direction was along the $[\bar{1}2\bar{1}0]$ direction.

Table 6.1. SF calculations for major slip systems and conventional twinning modes.

Compression Direction	Basal	Prismatic	Pyramidal I	<c+a>	$\{10\bar{1}2\}$ Twin	$\{10\bar{1}1\}$ Twin
$[\bar{1}2\bar{1}0]$	0	0.43	0.38	0.45	0.37	0.31

Table 6.2. SF calculations for the 6 different $\{10\bar{1}2\}$ twinning variants.

Compression Direction	$(10\bar{1}2)$ Twin	$(01\bar{1}2)$ Twin	$(\bar{1}102)$ Twin	$(\bar{1}012)$ Twin	$(0\bar{1}12)$ Twin	$(1\bar{1}02)$ Twin
$[\bar{1}2\bar{1}0]$	0	0.37	0.37	0	0.37	0.37

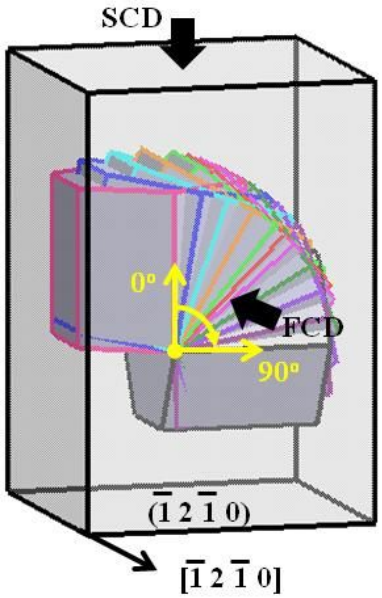

Figure 6.1. The first compression direction is along $[\bar{1}2\bar{1}0]$ direction to generate the $\{10\bar{1}2\}$ twin for all the samples. The specimens are then rotated 90°, so that the various deformation modes were activated by second compression.

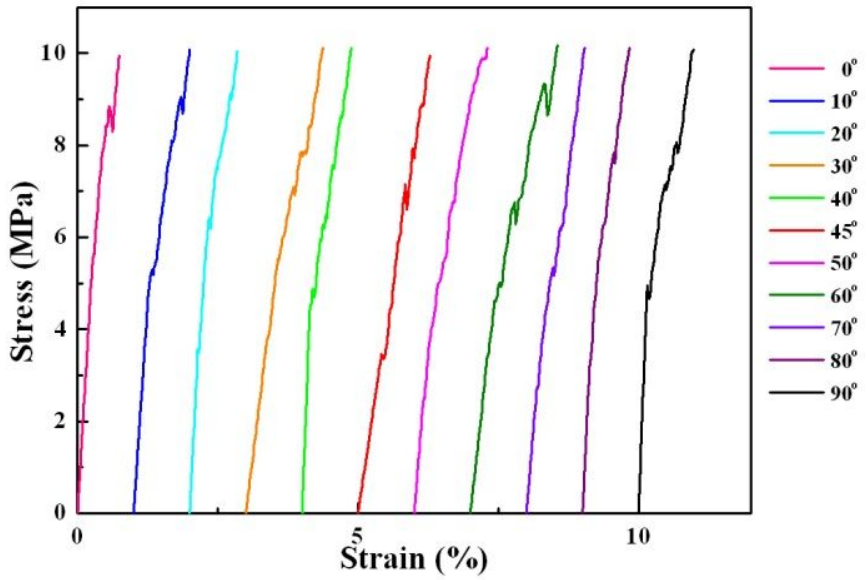

Figure 6.2. Typical compressive flow curves when specimens deformed up to 10MPa along the $[\bar{1}2\bar{1}0]$ direction.

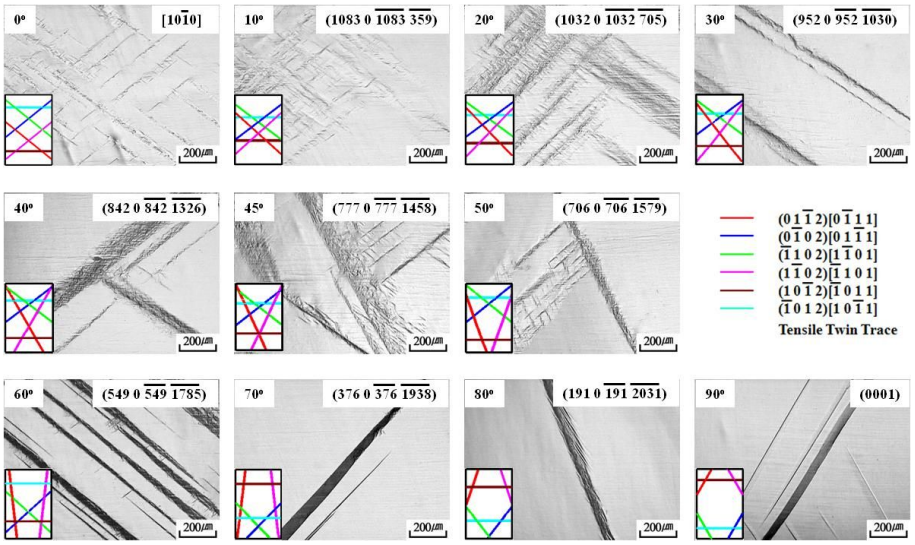

Figure 6.3. Microstructures are taken from the sections of side surface for 10MPa uni-axially deformed specimens.

Afterwards, eleven specimens were rotated 90 °, which indicates that the compression direction was changed from basal plane to prismatic plane at an interval of 10 ° and an additional orientation of 45 ° to activate various slip and twinning modes during the second compression process. Detailed information about the compression direction is shown in the left corner part of Figure 6.4 (a). The mechanical properties without pre-deformation for corresponding orientations by uni-axial compression tests have also been included in Figure 6.4 (a). High magnification of the rectangular box located at the bottom of the graph in Figure 6.4 (a) is shown in Figure 6.4 (b). It can easily be seen that the flow stress of the TSC tests is higher than that of the uni-axial compression tests for crystals with the same orientation and this indicates that twin boundaries acted as obstacles to dislocation glides and dislocations impinged at twin boundaries and gave rise to an increase in the flow stress. From the previous study [32], the dominated deformation modes for corresponding crystals have been analyzed by the uni-axial compression tests. In the case of the 0 ° rotated specimen, the <c+a> slip is adapted to rationalize the high yield strength. The basal slip plays a dominant role in the specimen with 10 – 60 ° to the c-axis and $\{10\bar{1}2\}$ twin is dominating the initial part of deformation for the 70 – 90 ° rotated specimens. Therefore, various types of dislocations must be activated through the second step compression and would encounter the pre-existing $\{10\bar{1}2\}$ twin bands. It is interesting to note that curve serration by the $\{10\bar{1}2\}$ twin is far less than that of uni-axial compression test for the 70 – 90 ° rotated specimens. This indicates that the serrated stress-strain curve with a strong drop of stress could be the result of rapid nucleation of fresh twins during the uni-axial compression test and the rapid nucleation of fresh twins were suppressed by the pre-existed $\{10\,\bar{1}\,2\}$ twin during TSC tests. Figure 6.5 shows

microstructures after the second step compression tests. Rough morphologies have been developed for the 0 ° specimen because various deformation modes contributed to plastic deformation. As expected, horizontal basal slip traces were clearly observable from the 10 – 60 ° specimens in the matrix region. In the case of the 70 – 90 ° rotated specimen, fresh $\{10\bar{1}2\}$ twin traces were observed.

In order to identify the slip and twin traces, the standard 0 °, 45 ° and 90 ° rotated specimens were chosen for further examination by EBSD technique. Local microtexture showed regions containing a mixture of matrix and twinned areas are seen in Figure 6.6. The superimposed unit cells illustrate the orientation of each location by the TSL software. The blue, green and red lines correspond to the misorientation angle between 35 ° – 40 °, 55 ° – 60 ° and 85 ° – 90 °, respectively. The marked area in Figure 6.6 (a) looked like twin morphology, but the boundary was not highlighted. A hexagonal unit cell orientation was indicated at the marked area and other several locations. A comparison of the matrix region and marked area is almost the same, suggesting that this twin band was activated by first compression and restored to its original orientation by subsequent reloading. This provides strong evidence that the $\{10\bar{1}2\}$ twins return to the original orientation by de-twinning, rather than re-twinning within primary twin regions for the 0 ° specimen. Several groups have utilized cyclic loading experiments and revealed that extension twins were produced by pre-straining and progressively disappeared during reverse reloading in AZ31 and ZK60 Mg alloys [33-36]. To summarize, the current observation from both TSCed 0 ° specimen and Mg alloys subjected to cyclic loading confirmed that the $\{10\bar{1}2\}$ twin was activated by first step compression and subsequently removed by second compression. Similar to the 45 ° specimen, a hexagonal unit cell for

the marked area in Figure 6.6 (b) is the almost same as matrix orientation as well. The marked area is the narrow $\{10\bar{1}2\}$ twin that was nucleated at the primary twin boundaries by first compression and recovered its original orientation during second compression. On the other hand, the wide primary $\{10\bar{1}2\}$ twin band still remained twinned structure, which indicated that a wide twin band was more resistant to de-twinning compared to a fine twin band. In the case of the 90 ^{o} specimen, the second direction is the $[10\bar{1}0]$ direction which is favorable for the $\{10\bar{1}2\}$ twin activation. As expected, fresh twins were formed during the second compression and slip traces were rarely seen.

Figure 6.7 (a) shows the yield strengths for same orientations in the uni-axial and TSC tests. Obviously, the yield strength of TSC test specimens is higher than that of the specimens without pre-straining (uni-axial compression specimens). The effectiveness of $\{10\bar{1}2\}$ twins in the mechanical behavior was evaluated using equation 6.1. The right Y axis indicates the rate of increase in yield strength for TSC tests. The strengthening effect is relatively small for the 0^{o} rotated specimen. However, in the case of basal slip and $\{10\bar{1}2\}$ twin dominated regions, pre-existing twins play as effective barriers to dislocation movement. The strengthening mechanism will be discussed in detail in the discussion part.

$$\text{Rate of Increse} = \frac{\sigma_{\text{Two-Step Comp.}} - \sigma_{\text{Uni-Axial Comp.}}}{\sigma_{\text{Uni-Axial Comp.}}} \text{ x } 100(\%) \qquad (6.1)$$

In contrast to the high-symmetry cubic crystals such as FCC metals, the stacking faults in the lower symmetry HCP structures have received much less attention. To our knowledge, stacking faults are less frequently formed in

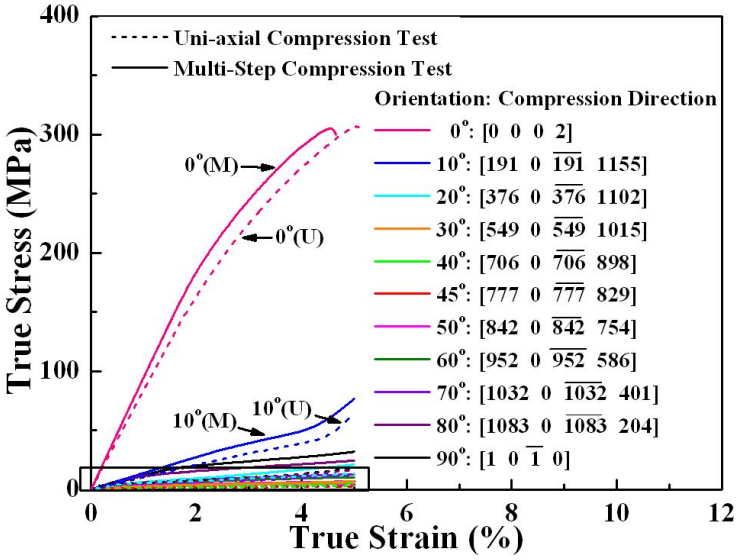

(a)

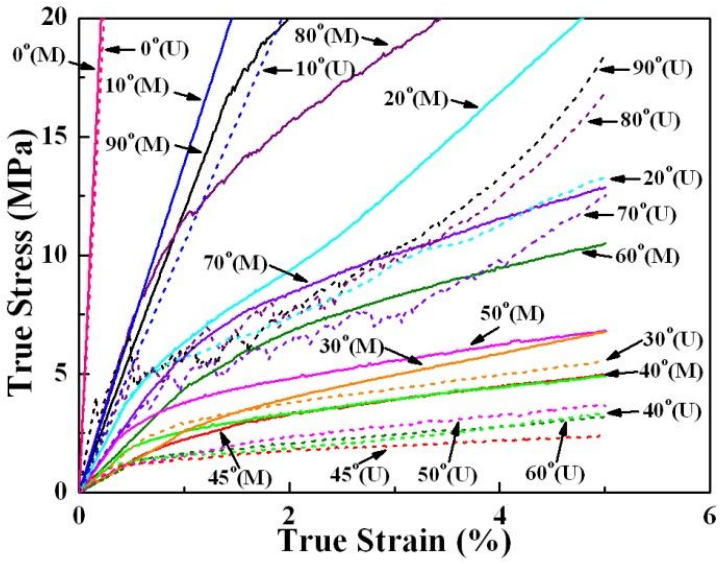

(b)

Figure 6.4. (a) Comparison between uni-axial and TSC flow curves. (b) Enlargement of the marked box in (a).

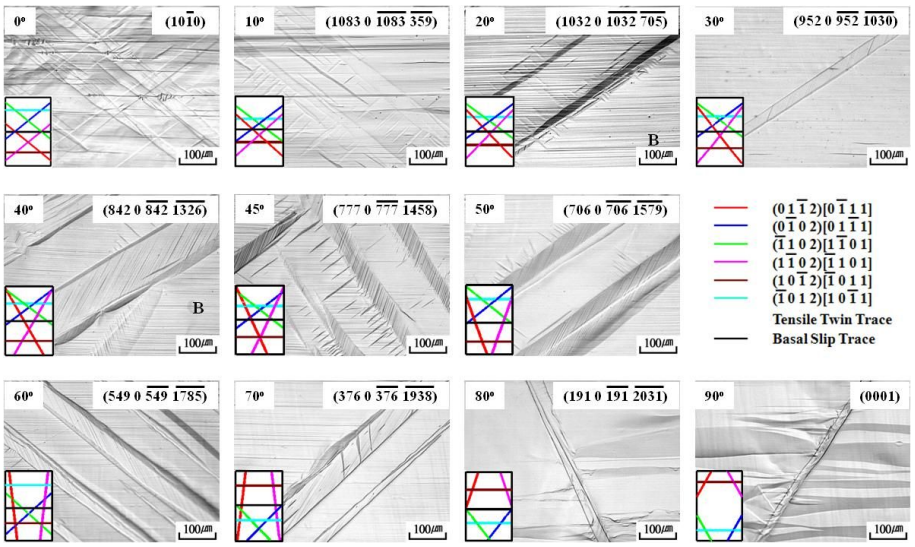

Figure 6.5. Microstructure observations after TSC tests for 10MPa pre-deformed crystals.

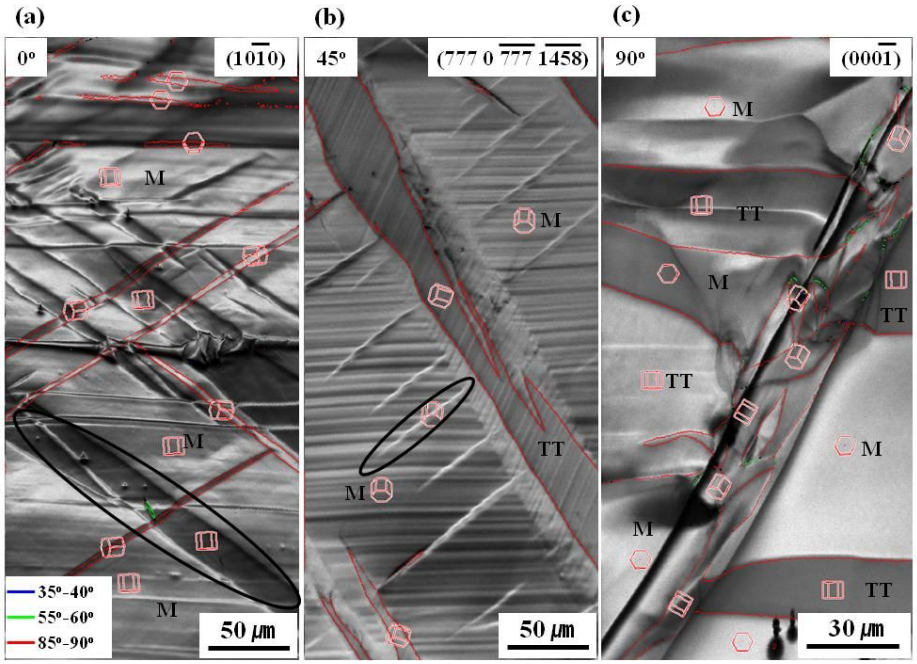

Figure 6.6. (a), (b), and (c) are Kikuchi band contrast map which corresponding 0 °, 45 °, and 90 ° rotated specimens.

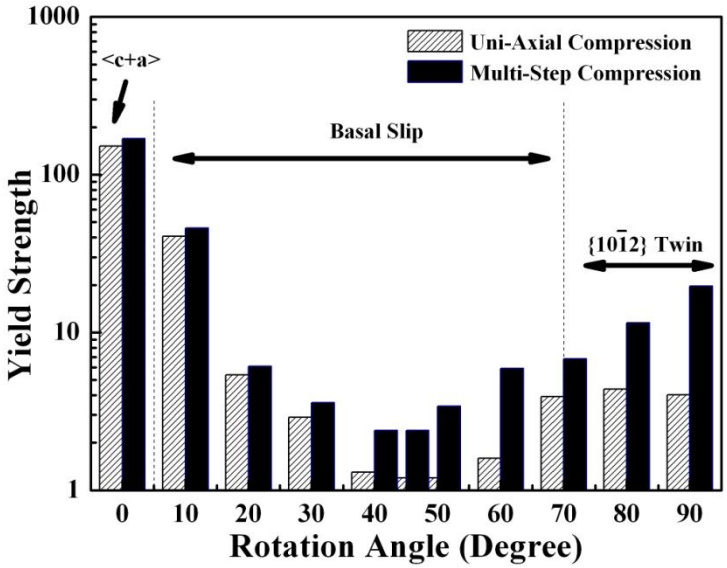

(a)

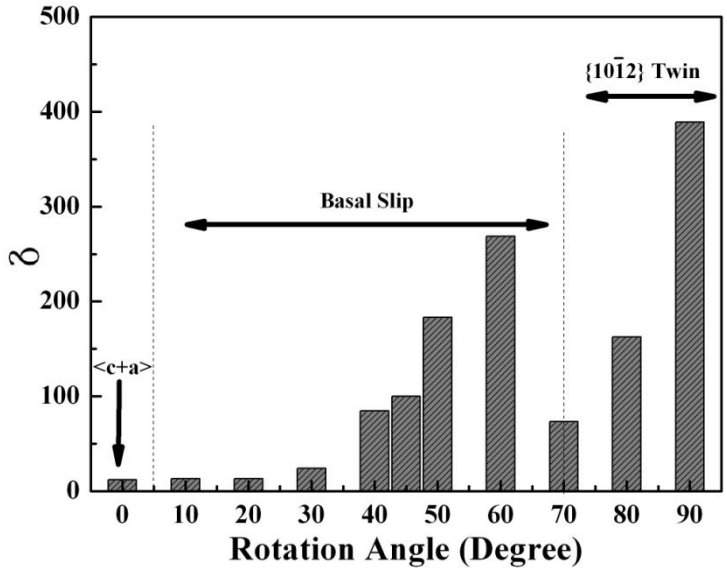

(b)

Figure 6.7. (a) Yield strength for corresponding orientations by uni-axial and TSC tests. (b) Rate of increase for yield strength between uni-axial and TSC tests.

HCP materials during plastic deformation owing to their high stacking faults energy [1]. However, stacking faults have been frequently observed in twins in HCP metals after plastic deformation [37-38]. In order to examine the internal microstructures of twined parts, TEM images were taken with an incident electron beam direction of <11$\bar{2}$0> under the bright field (BF) and STEM-HAADF conditions for 10MPa pre-deformed 45 ^{o} specimen, as shown in Figure 6.8. The microstructures have complex defect structures, including multiple possible Burgers vectors for dislocations and numerous stacking faults within the twin plates and neighbouring matrix regions. One end of the fault was usually in contact with the twin boundary and the other end terminated within the middle of the twin band, and no partial dislocations associated with these faults were observed. And those twin-induced stacking faults may also act as obstacles to subsequent dislocation glide and thus contributed to the hardening effects for all the TSC tested samples. Li et al. [39] have also investigated the stacking faults and their interaction with pyramidal dislocations in polycrystalline pure Mg, and reported that the stacking faults consisted of well-defined fringes and streaking.

The strengthening from twins has generally been attributed to the apparent grain refinement effect of deformation twinning with the twin boundaries acting as obstacles to dislocations. In addition, slip dislocations impinging against the complicated dislocations and stacking faults formed by the {10$\bar{1}$2} twin could be incorporated into the obstacle and give rise to an increase in the flow stress [40]. However, the effectiveness of the {10$\bar{1}$2} twin seems to be different for the specimens as shown in Figure 6.7 (b). For the 0 ^{o} specimen, the {10$\bar{1}$2} twin has a small rate increase of yield strength. With increasing the rotation angle, the rate increase of yield strength increased up to 60 ^{o} rotated specimen. From the previously reported research [41-42],

<c+a> slip is responsible for the 0 ^{o} rotated specimen and the CRSS value for the <c+a> slip is very high compared with other deformation modes which may lead to limited hardening effects for the 0 ^{o} rotated specimen.

Figure 6.9 (a) shows the Kikuchi map obtained from the sections of (777 0 $\overline{777}$ $\overline{1458}$) plane in the 45 ^{o} rotated specimen, where M and TT represent the parent matrix and twinned region, respectively. As expected, distinct slip bands were aligned with the plane trace of the basal slip mode in the matrix region. Figure 6.9 (b) indicates the different Schmid factor value of (0002)<11$\bar{2}$0> basal slip for the corresponding area in Figure 6.9 (a). The twinned region has a low Schmid factor for (0002)<11$\bar{2}$0> basal slip compared to the matrix region, however, basal slip traces were readily observable within tensile twin band. A careful observation indicates that the basal slip traces in the matrix were continuous across the twin boundary and the dislocations simply cross-slip onto the basal plane in the twinned crystal. It can be known that basal <a> type dislocations in the matrix transformed to basal <a> type dislocations within the {10$\bar{1}$2} twin. Yoo [4,18] presented a comprehensive review of the possible interactions of the perfect dislocations of six slip systems and the dislocation with several twin modes in HCP metals which have been analyzed on crystallography and elasticity theories. Taking into account, the observations from the 45 ^{o} rotated specimen, it can be known that the {10$\bar{1}$2} twin not only acts as a barrier, but also reorients matrix domains into orientations that may be favorable for basal slip dislocations due to twin boundary from experimental results.

An EBSD image of the microstructure obtained from (000$\bar{1}$) plane with 90 ^{o} rotated specimen after TSC test is presented in Figure 10 (a). The matrix, 4 {10$\bar{1}$2} twin variants and {10$\bar{1}$2}-{10$\bar{1}$2} twin are labeled M, $TT_{1\sim4}$ and DT, respectively. The distribution of misorientation angle in Figure 6.10 (b) shows

that high frequency peaks appear near 86 ^{o} indicating the $\{10\bar{1}2\}$ tensile twin. Figure 6.10 (c) depicts the crystallographic orientation from the parent matrix M to the orientation TT_1~TT_4 by primary $\{10\bar{1}2\}$ twin and small portion of TT_1 orientation converts to orientation DT by secondary $\{10\bar{1}2\}$ twin. The presence of $\{10\bar{1}2\}$-$\{10\bar{1}2\}$ double twins can be clearly seen in Figure 6.10 (a). From the crystallography of the $\{10\bar{1}2\}$-$\{10\bar{1}2\}$ double twinning in Mg, misorientation angles between matrix and any of the six secondary twin variants would be either 7.4 ^{o}, 59.9 ^{o} or 60.4 ^{o} with misorientation axes $<1\bar{2}10>$, $<10\bar{1}0>$ or $<8\bar{1}\bar{7}0>$, respectively [9-11]. Because the misorientation angles and axes are close to the latter two variants, it is difficult to distinguish them experimentally. Anyhow the small frequency peaks appeared near 7 ^{o} and 60 ^{o} corresponded to $\{10\bar{1}2\}$-$\{10\bar{1}2\}$ double twin in Figure 6.10 (b). In order to understand the activation mechanisms that caused specific twin variants during TSC deformation, a Schmid factor analysis was performed for 90 ^{o} specimen. According to Schmid factor analysis in Figure 6.11 (a), four twin variants have the highest SF value of 0.37, and thus TT_1 and TT_3 variants were formed during first compression. The rest of two twin variants were missing in Figure 6.10 (c) because of local area observation. The second compression direction ($[10\bar{1}0]$) is also perpendicular to the c-axis which indicates the $\{10\bar{1}2\}$ twin is the dominant deformation mode. Figure 6.11 (b) shows that two twin variants have the highest SF value of 0.5, which is corresponding to TT_2 and TT_4 variants in Figure 6.10 (c). A careful observation indicates that TT_2 and TT_4 twin variants were generated by secondary compression and encountered pre-existing twin variants (TT_1 and TT_3) and thus twin-twin interactions have been taken place. When fresh twins (TT_2 and TT_4) encountered an advanced

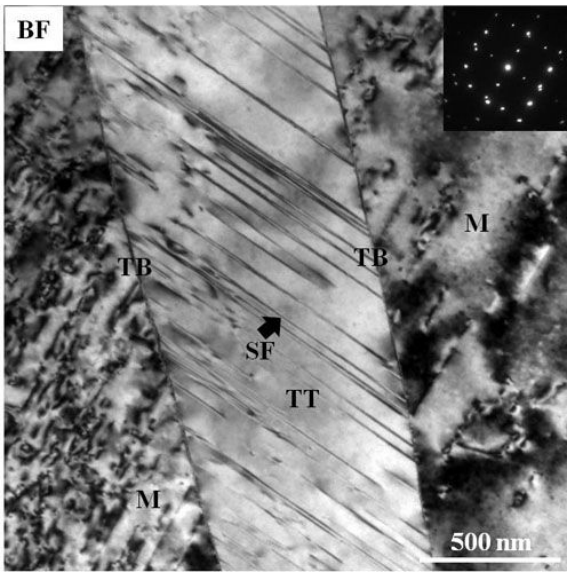

(a)

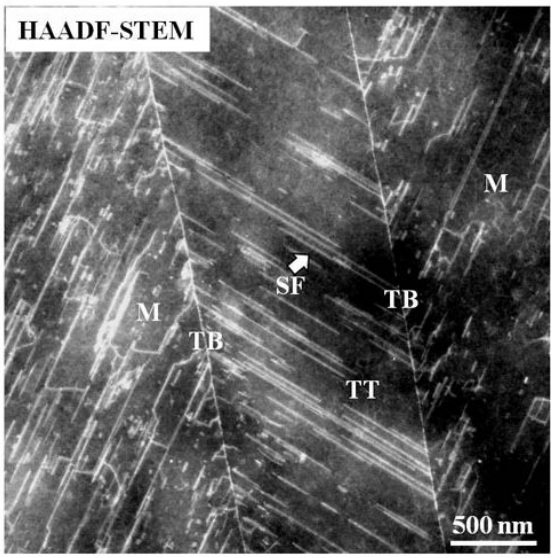

(b)

Figure 6.8. (a) Bright-field TEM micrographs of deformation twins and selected area diffraction pattern (SADP) showing reflections from both the matrix and twin. (B//$[11\bar{2}0]_{\alpha}$). (b) Corresponding areas for STEM-HAADF image.

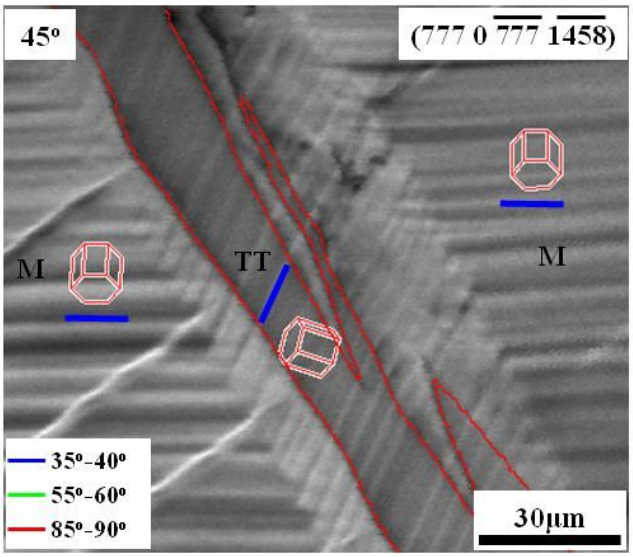

(a)

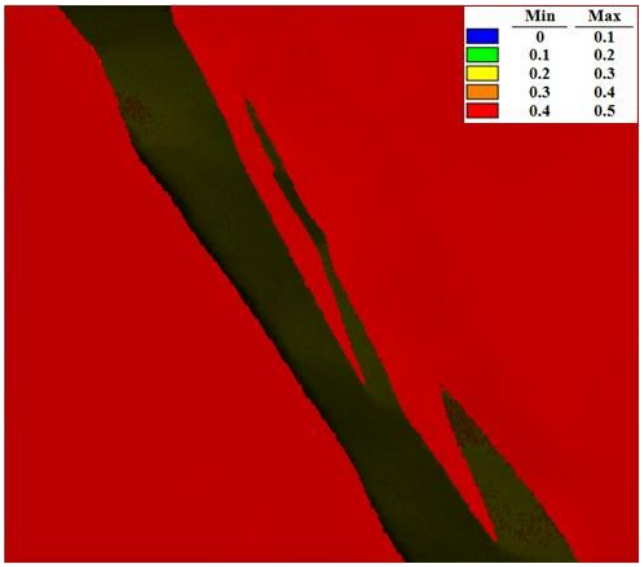

(b)

Figure 6. 9. (a) Kikuchi map obtained from sections of (777 0 $\overline{777}$ $\overline{1458}$) plane for the 45 ° rotated specimen and matrix and twinned crystal are indicated by M and T respectively. (b) Schmid factor map distribution for (0002)<11$\bar{2}$0> basal slip.

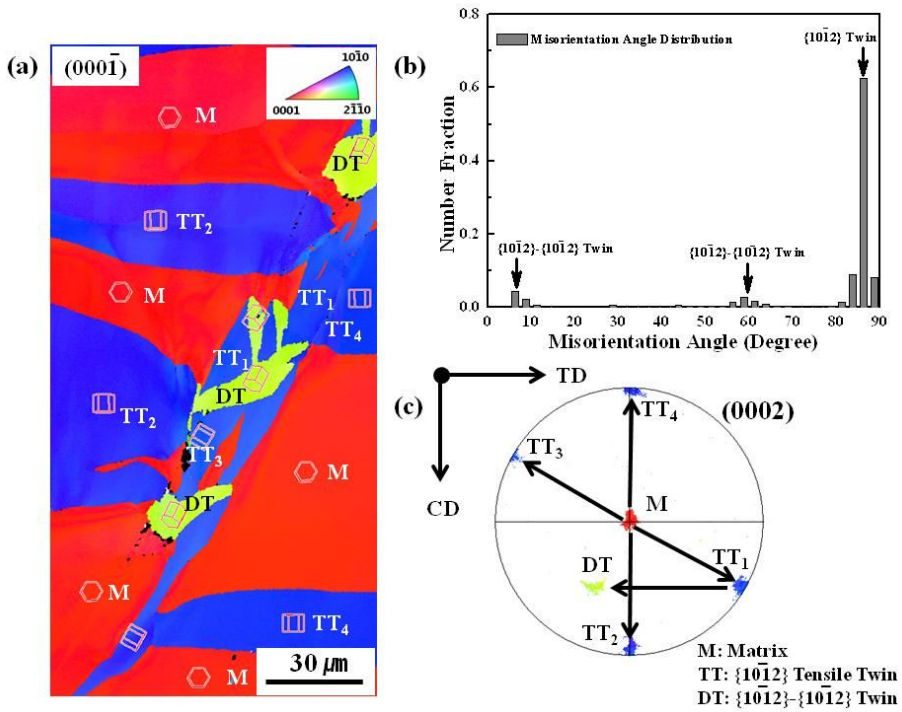

Figure 6. 10. (a) Crystallographic orientation map obtained from sections of (000$\bar{1}$) plane for the 90 ° rotated specimen. (b) Misorientation angle distribution full area. (c) crystallographic orientation of matrix and twin variants.

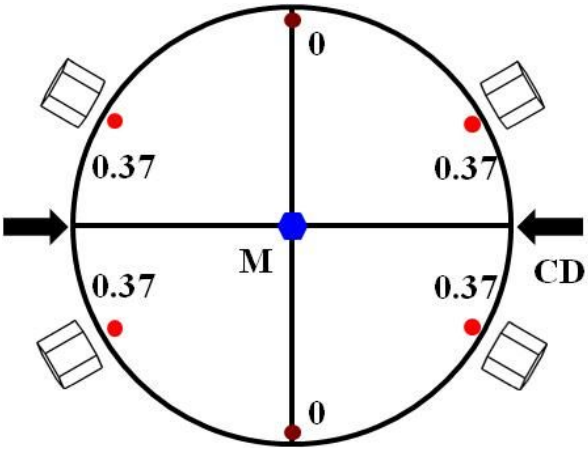

(a)

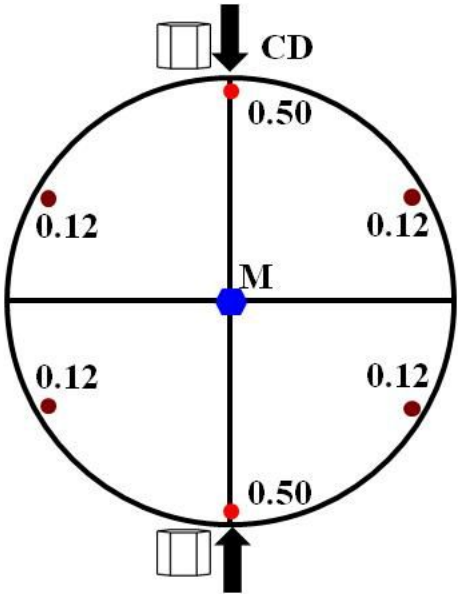

(b)

Figure 6. 11. Schmid factor analysis on $\{10\bar{1}2\}$ twinning variants for the 90 ^{o} rotated specimen. (a) First compression (compression direction along $[\bar{1}2\bar{1}0]$ direction). (b) Second compression (compression direction along $[10\bar{1}0]$ direction).

twin, no penetrated intersection of twins was observed. Since fresh twins were impinged by pre-existing twin, the second-order $\{10\bar{1}2\}$-$\{10\bar{1}2\}$ twinning within the primary TT_1 was facilitated by twin intersection. It was shown that twin interfaces could be the source of new twin dislocations.

Meyers et al. [43] have reported that it is common for the twinning stress to increase more rapidly with decreasing grain size than the stress required to activate slip, which denotes that the Hall–Petch slope for deformation twinning-mediated plasticity (k_T) is frequently greater than that for dislocation-slip-controlled plasticity (k_S). For example, Song and Gray [44] demonstrated experimentally that the Hall-Petch slope for twinning of zirconium was almost ten times higher than slip. More recently, Barnett et al. [45] have examined the influence of the grain size on compressive deformation of AZ31 alloy and reported the Hall-Petch slop for twinning dominated flow is 3.72-11.78 times higher than that of slip dominated flow at elevated temperature. As aforementioned, the second compression was twin dominated deformation process for 90 ^{o} rotated specimen and flow stress increased dramatically because single crystal was subdivided into several grains by primary twins during the first compression test. This may be responsible for the effectiveness of the $\{10\bar{1}2\}$ twin for a twin dominated flow (90 ^{o} specimen) which is higher than a basal slip dominated deformation. The region around a twin intersection may be highly strained because of the lack of continuity of the twinning shear at a twin intersection. Thus, the interaction between the twins may also account for a hardening effect of the strain compared with slip and twin interactions.

6.3 Conclusions

Plastic deformation behavior of Mg single crystals with TSC tests has been systematically studied, revealing the strengthening mechanisms of pre-straining due to extension twins. The following conclusions can be drawn:

1) It is found that the results from the activation of $\{10\bar{1}2\}$ primary twin variants are governed by the Schmid law.

2) $\{10\bar{1}2\}$ twin boundaries could act as barriers to various mobile dislocations, incorporating into the obstacle twins and give rise to an increase of flow stress.

3) An amount of the $\{10\bar{1}2\}$ twins formed during the first step compression have been removed via de-twinning during the second compression for the <c+a> slip dominated specimen.

4) $\{10\bar{1}2\}$ twins have limited hardening effects for <c+a> slip dominated specimen owing to the hard orientation with high CRSS value for <c+a> slip.

5) The intersection of glide basal dislocations with $\{10\bar{1}2\}$ twin boundaries can produce basal dislocations within the primary twin bands.

6) The effectiveness of the $\{10\bar{1}2\}$ twin for a twin dominated flow (90^{o} specimen) is much higher than other specimens because the Hall-Petch slop for twinning-dominated flow is frequently greater than that of slip-dominated one.

Bibliography

1. P.G. Partridge, "The Crystallography and Deformation Modes of Hexagonal close-packed Metals", Met. Rev., 12 (1967), pp. 169-194.
2. Y.N. Wang and J.C. Huang, "The Role of Twinning and Untwinning in Yielding Behavior in Hot-extruded Mg–Al–Zn Alloy", Acta Mater., 55 (2007), pp. 897-905.
3. M. Knezevic, A. Levinson, R. Harris, R.K. Mishra, R.D. Doherty and S.R. Kalidindi, "Deformation Twinning in AZ31: Influence on Strain Hardening and Texture Evolution", Acta Mater., 58 (2010), pp. 6230-6242.
4. M. H. Yoo, "Slip, Twinning, and Fracture in Hexagonal Close-Packed Metals", Metal. Trans. A, 12 (1981), pp. 409-418.
5. R.E. Reed-Hill and W.D. Robertson, "Additional Modes of Deformation Twinning in Magnesium", Acta Metal., 5 (1957), pp. 717-727.
6. H. Yoshinaga, T. Obara and S. Morozumi, "Twinning Deformation in Magnesium Compressed along the C-Axis", Mater. Sci. Eng. A, 12 (1973), pp. 255-264.
7. J.W. Christian and S. Mahajan, "Deformation Twinning", Prog. Mater. Sci., 39 (1995), pp. 1-157.
8. M.D. Nave and M.R. Barnett, "Microstructures and Textures of Pure Magnesium Deformed in Plane-strain Compression", Scripta Mater., 51 (2004), pp. 881-885.
9. A.G. Crocker, "Double Twinning", Phil. Mag., 7 (1962), pp. 1901-1924.
10. L. Jiang, J.J. Jonas, A.A. Luo, A.K. Sachdev and S. Godet, "Twinning-induced Softening in Polycrystalline AM30 Mg Alloy at Moderate

Temperatures", Scripta Mater., 54 (2006), pp. 771-775.

11. M.R. Barnett, Z. Keshavarz, A.G. Beer and X. Ma, "Non-Schmid Behaviour during Secondary Twinning in a Polycrystalline Magnesium Alloy", Acta Mater., 56 (2008), pp. 5-15.
12. J. Koike, "Enhanced Deformation Mechanisms by Anisotropic Plasticity in Polycrystalline Mg Alloys at Room Temperature", Metall. Mater. Trans. A, 36 (2005), pp. 1689-1696.
13. Y. Chino, K. Kimura, M. Hakamada and M. Mabuchi, "Mechanical Anisotropy due to Twinning in an Extruded AZ31 Mg Alloy", Mater. Sci. Eng. A, 485 (2008) pp. 311-317.
14. L. Jiang and J.J. Jonas, "Effect of Twinning on the Flow Behavior during Strain Path Reversals in Two Mg (+Al, Zn, Mn) Alloys", Scripta Mater., 58 (2008), pp. 803-806.
15. M.T. Tucker, M.F. Horstemeyer, P.M. Gullett, H.E. Kadiri and W.R. Whittington, "Anisotropic Effects on the Strain Rate Dependence of a Wrought Magnesium Alloy", Scripta Mater., 60 (2009), pp. 182-185.
16. B.H. Lee, S.M. Kim, M.E. Mehtedi, E. Evangelista and C.S. Lee, "Effect of Stress State on the High Temperature Workability of AZ31 Mg Alloy", Metall. Mater. Int., 16 (2010), pp. 197-203.
17. P.B. Price, "Pyramidal Glide and the Formation and Climb of Dislocation Loops in Nearly Perfect Zinc Crystals", Phil. Mag., 5 (1960), pp. 873-886.
18. M.H. Yoo and C.T. Wei, "Growth of Deformation Twins in Zinc Crystals", Phil. Mag., 14 (1966), pp. 573-587.
19. S. Lay and G. Nouet, "Interaction of Slip Dislocations with the $(01\bar{1}2)$ Twin Interface in Zinc", Phil. Mag., 70 (1994), pp. 1027-1044.
20. A. Serra and D.J. Bacon, "Computer Simulation of Screw Dislocation

Interactions with Twin Boundaries in H.C.P.", Acta Metall., 43 (1995), pp. 4465-4481.

21. A. Serra and D.J. Bacon, "A New Model for $\{10\bar{1}2\}$ Twin Growth in HCP Metals", Phil. Mag., 73 (1996), pp. 3333-3343.
22. A. Serra, D.J. Bacon and R.C. Pond, "Dislocations in Interfaces in the H.C.P. Metals-I. Defects Formed by Absorption of Crystal Dislocations", Acta Mater., 47 (1999), pp. 1425-1439.
23. A. Serra, D.J. Bacon and R.C. Pond, "Twins as Barriers to Basal Slip in Hexagonal-Close-Packed Metals", Metall. Mater. Trans. A, 33 (2002), pp. 809-812.
24. H. L. Kim and Y. W. Chang, "An Internal Variable Approach of Orientation Dependent Deformation Mechanism of Rolled AZ31 Magnesium Alloy", Metall. Mater. Int., 17 (2011), pp. 721-728.
25. G. Wan, B.L. Wu, Y.D. Zhang, G.Y. Sha and C. Esling, "Anisotropy of Dynamic Behavior of Extruded AZ31 Magnesium Alloy", Mater. Sci. Eng. A, 527 (2010), pp. 2915–2924.
26. B.S. Wang, R.L. Xin, G.J. Huang and Q. Liu, "Effect of Crystal Orientation on the Mechanical Properties and Strain Hardening Behavior of Magnesium Alloy AZ31 during Uniaxial Compression", Mater. Sci. Eng. A, 534 (2012), pp. 588–593.
27. S.H. Park, S.G. Hong, J.H. Lee and C.S. Lee, "Multiple Twinning Modes in Rolled Mg–3Al–1Zn Alloy and Their Selection Mechanism", Mater. Sci. Eng. A, 532 (2012), pp. 401–406.
28. A. Chapuis and J.H. Driver, "Temperature Dependency of Slip and Twinning in Plane Strain Compressed Magnesium Single Crystals", Acta Mater., 59 (2011), pp. 1986-1994.
29. M. R. Barnett, "A Rationale for the Strong Dependence of Mechanical

Twinning on Grain Size", Scripta Mater., 59 (2008), pp. 696–698.

30. H. L. Kim and Y. W. Chang, "Deformation Mechanism Temperature-Dependence of AZ31 Magnesium Alloy", Metall. Mater. Int., 17 (2011), pp. 563-568.
31. M. Niewczas and G. Saada, "Twinning Nucleation in Cu-8 at.%Al Single Crystals", Phil. Mag., 82 (2002), pp. 167-191.
32. M.Z. Bian and K.S. Shin, SNU, Seoul, unpublished research, 2012.
33. R.H. Wagoner, X.Y. Lou, M. Li and S.R. Agnew, "Forming Behavior of Magnesium Sheet", J. Mater. Pro. Tech., 177 (2006), pp. 483-485.
34. X.Y. Lou, M. Li, R.K. Boger, S.R. Agnew and R.H. Wagoner, "Hardening Evolution of AZ31B Mg Sheet", Int. J. Plast., 23 (2007), pp. 44-86.
35. L. Wu, A. Jain, D.W. Brown, G.M. Stoica, S.R. Agnew, B. Clausen, D.E. Fielden and P.K. Liaw, "Twinning–detwinning Behavior during the Strain-controlled Low-cycle Fatigue Testing of a Wrought Magnesium Alloy, ZK60A", Acta Mater., 56 (2008), pp. 688-695.
36. S.H. Kwon, K.S. Song, K.S. Shin and S.I. Kwun, "Low Cycle Fatigue Properties and an Energy-Based Approach for as-Extruded AZ31 Magnesium Alloy", Metall. Mater. Int., 17 (2011), pp. 207-213.
37. S.G. Song and G.T. Gray III, "Transmission Electron Microscopy Examination and Analysis of an Anomalous Stacking Fault in H.C.P. Metals", Phil. Mag., 71 (1995), pp. 263-274.
38. D. Bhattacharyya, E.K. Cerreta, R. McCabe, M. Niewczas, G.T. Gray III, A. Misra and C.N. Tome, "Origin of Dislocations within Tensile and Compressive Twins in Pure Textured Zr", Acta Mater., 57 (2009), pp. 305-315.
39. B. Li, P.F. Yan, M.L. Sui and E. Ma, "Transmission Electron

Microscopy Study of Stacking Faults and Their Interaction with Pyramidal Dislocations in Deformed Mg", Acta Mater., 58 (2010), pp. 173-179.

40. Y.C. Xin, M.Y. Wang, Z. Zeng, M.G. Nie and Q. Liu, "Strengthening and Toughening of Magnesium Alloy by $\{10\bar{1}2\}$ Extension Twins", Scripta Mater., 66 (2012), pp. 25–28.
41. B.C. Wonsiewicz and W.A. Backofen, "Plasticity of Magnesium Crystals", Trans. AIME., 239 (1967), pp. 1422-1431.
42. T. Obara, H. Yoshinga and S. Morozumi, "$\{11\bar{2}2\}$ $<11\bar{2}3>$ Slip System in Magnesium", Acta Metall., 21 (1973), pp. 845-853.
43. M.A. Meyers, O. Vohringer and V.A. Lubarda, "The Onset of Twinning in Metals: A Constitutive Description", Acta Mater., 49 (2001), pp. 4025-4039.
44. S.G. Song and G.T. Gray III, "Influence of Temperature and Strain Rate on Slip and Twinning Behavior of Zr", Metall. Mater. Trans. A, 26 (1995), pp. 2665-2675.
45. M.R. Barnett, Z. Keshavarz, A.G. Beer and D. Atwell, "Influence of Grain Size on the Compressive Deformation of Wrought Mg-3Al-1Zn", Acta Mater., 52 (2004), pp. 5093-5103.

초 록

마그네슘합금은 밀도가 1.74 g/cm^3 정도로써 현재까지 개발된 상용 구조용 합금 중에서 최소의 밀도를 가지며 또한, 비강도 및 비탄성 계수가 우수하고, 진동, 충격 등에 대한 흡수성이 탁월하며 전기 및 열전도도, 가공성, 피로, 충격 특성 및 재활용이 가능한 친환경적 소재이기에 자동차 차제 경량화의 핵심 소재로 연구 개발이 활발하게 진행되고 있다. 마그네슘합금 부품은 크게 두 가지로 분류할 수 있다. 하나는 중력주조, 다이캐스팅 등과 같은 주조 공정을 이용한 캐스팅 마그네슘합금이며, 다른 하나는 압출, 압연이나 단조와 같은 소성가공 공정을 이용한 가공 마그네슘합금이다. 현재 대부분의 마그네슘 합금 부품은 주조 공정, 특히 다이캐스팅 공정에 의해 제조되고 있으나, 주조재의 경우 낮은 강도와 인성 등에 의한 결함을 피할 수 없다는 단점을 가지고 있다. 이에 반하여 가공용 마그네슘 합금의 경우에는, 기계적 특성이 우수하며 내부 결함이 없는 제품을 얻을 수 있다. 하지만 여러 가지 기초 및 기술적인 문제로 인하여 고성능 마그네슘 합금의 광범위한 응용에 영향을 받고 있다. 예를 들어, 가공 마그네슘 합금의 경우 압연 등 가공 공정으로 인해 강한 (0002) 저면 집합조직이 발달되어 강한 이방성 기계적 거동을 나타나며 이로 인해 성형 성이 저하하게 된다. 한편 온도와 초기 방위에 따른 슬립과 쌍정의 변형거동, 변형모드간의 상호작용 및 쌍정으로 인한 재결정 현상에 대한 체계적인 연구가 미미하다.

본 연구에서는 우선 각 슬립 및 쌍정 모드의 임계전단응력을 도출하기 위하여 여러 가지 방위를 가진 시편에 대하여 기계적 특성을 평가하였다. 아울러 마그네슘 단결정의 체계적인 변형거동 분석을 위해 광학현미경 및 전자현미경 등의 평가 방법에 의해 얻어진 실험결과의 심층적이고 체계적인 변형거동 분석을 수행하였다. 이러한 단결정의 특성평가 결과를 바탕으로 Single 슬립이 일어나기에 유리한 방위는 Schmid factor 이론에 이용하여 해당되는 변형기구의 임계전단응력을 도출하였다. 한편 여러 가지 변형모드가 소성변형에 기여할 때 미소역학에 기초한 viscoplastic self-consistent (VPSC) 전사모사를 통하여 각 변형모드의 임계전단응력을 도출하였다. 전산 모사 결과로 보아 저면 슬립과 {10 $\bar{1}$ 2} 쌍정 응력은 온도의 영향에 민감하지 않으며, 반대로 prismatic, <c+a> 슬립과 {10$\bar{1}$1} 쌍정 응력은 온도의 영향을 크게 받는 것으로 관찰 되었다. 마그네슘 단결정의 현저한 변형의 이방성은 응력 방향에 따른 변형기구의 차이에서 비롯되며 이는 결정 구조로 유력하다. HCP 결정구조를 지닌 마그네슘은 저면 슬립의 임계전단응력과 {10$\bar{1}$2} 쌍정의 응력 값을 분석한 결과, 다른 변형기구 즉, prismatic 슬립, <c+a> slip, {10$\bar{1}$1} 등 쌍정 응력 값보다 훨씬 작기에 상온에서 지배적으로 나타난다. 한편 {10 $\bar{1}$ 2} 쌍정은 c축으로 변형을 수용하기에 변형거동에 큰 영향을 미치고 있으나, 큰 변형을 수용하기에는 {10$\bar{1}$2} 쌍정만으로는 부족하기에 추가적인 슬립기구를 필요로 하고 있다. 이로 인해 슬립 전위와 쌍정 경계의 상호작용은 불가피하며 또한 변형 쌍정은 전위 이동에 방해물로 작용하여 가공경화에 기여하게 된다. 두 번째 연구목적은 소성 변형

및 재결정 거동에 대한 {10 $\bar{1}$ 2} 쌍정의 영향을 체계적으로 평가하였다.

현재까지 강한 저면 집합조직을 약화시키기 위하여 많은 노력이 진행되어 왔다. 하지만 초기 방위에 따른 기계적 특성에 대한 체계적인 연구가 진행되지 않아 이상적인 집합조직에 대한 언급이 전무한 실정이다. 세 번째 연구목적은 초기 방위에 따른 기계적 특성을 체계적으로 분석하였다. 0도 회전된 시편의 경우 <c+a> 슬립이 주된 변형기구로, 저면 슬립이 10도에서 60도 회전 시편에서 주된 변형기구로, {10 $\bar{1}$ 2} 쌍정이 70도에서 90 회전 시편에서 주된 변형기구로 나타내었다. 두 번째 연구 목표는 단지 저면 슬립과 {10$\bar{1}$2} 쌍정의 상호작용에 대하여 제한되었으나 본 연구에서는 여러 가지 변형기구와 {10 $\bar{1}$ 2} 쌍정의 상호작용을 분석하였다. 0도 회전된 시편에 대한 {10$\bar{1}$2} 쌍정의 강화 현상은 미미하였으며 이는 <c+a> 슬립의 임계전단응력이 낮은 것으로 추정된다. 10도에서 60도 회전된 시편에서 저면 슬립 전위가 {10$\bar{1}$2} 쌍정 경계를 만난 다음 저면 슬립 전위가 {10$\bar{1}$2} 쌍정으로 인해 회전된 쌍정 영역을 교차 슬립으로 지나는 것을 확인하였다. 70도에서 90도까지 회전된 시편에서 {10$\bar{1}$2} 쌍정의 강화 효과는 다른 회전시편에 대하여 상대적으로 강한 것으로 나타내었다. 이는 쌍정이 지배적인 응력 곡선의 Hall-Petch 슬러프가 슬립이 지배적인 응력 곡선의 Hall-Petch 슬러프 상대적으로 높기 때문이다.

주요어: 임계전단응력, 슬립, 쌍정, 장애물, 재결정
학 번: 2006-23703

감사의 글

2006년 8월 31일 관악의 드넓은 교정에 첫발은 내디딘지도 어언 6년 반의 세월이 지났습니다. 길다면 길고 짧다면 짧은 시간 동안 20대의 열정으로 자그마한 꿈을 이루기 위해 매진한 끝에 작지만 부끄럽지 않은 결실을 맺게 되었습니다.

우선 전능하신 하나님께 감사를 드립니다. 참으로 보잘것없는 저를 만나주셨고 또한 이곳으로 인도해주셨으며 학위과정 동안 언제나 지켜봐 주시고 은총을 내려주신 하나님께 이 영광을 돌립니다. 하나님의 은총과 보살핌으로 이렇게 소박한 소망 하나를 이룰 수 있었음을 늘 기억하며 주님께서 이 세상에 보내주시면서 당신이 쓰시고자 하셨던 뜻대로 살아갈 수 있도록 늘 겸허한 자세로 살아가겠습니다.

참으로 부족한 저를 제자로 받아주셔서 오늘의 제가 있게 해 주신 평생의 스승이자 저의 지도 교수님이신 신광선 교수님께 고개 숙여 깊은 감사를 드립니다. 바쁘신 가운데 논문 심사와 지도편달을 아끼지 않으신 김영운 교수님, 한흥남 교수님, 최시훈 교수님 그리고 바쁜 회사일 속에서도 많은 가르침과 논문 심사를 해주신 이경훈 박사님께 깊은 감사를 드립니다. 제자가 늘 잘되기를 바라면서, 아낌없는 조언과 좋은 말씀해주신 존경하는 연변과학기술대학교 최재헌 교수님, 전지한 교수님, 이주성 교수님, 한길수 교수님, 이대열 교수님, 문영찬 교수님, 박순자 교수님, 박화수 교수님께 깊은 감사함을 전해 드리고 싶습니다.

처음 연구실에 발을 들일 때 서먹서먹하던 저를 따뜻이 맞아주시고 숱한 낮과 밤을 같이 보낸 여러 선배님과 동기들에게 감사드립니다. 이제는 졸업을 하고 사회에서 자기 역할을 다하고

있는, 임창동 박사님, 장우길 박사님, 유승훈 박사님, 황지훈 박사님, 송교수 박사님, 강문구 박사님, 우철이형, 재선이형, 두열이형, 종두형, 종채형, FanJun, 상근이형, 일환이, 남경이, 태규, 지형이, Tugce, HanSi, 순환에게 진심으로 감사의 말을 전하고 싶습니다. 현재 연구실의 맏형이자 힘들때마다 늘 곁에서 힘이 되어준 정화철 박사님, 연구실 책임을 맡고 있는 태일이를 주축으로 Madhan박사님, 기순형, 우영형, 정우형, 중원, 상준형, 철승형, 지권형, Kapil, Gianni, 막내 성호와 실험장비 및 시편제작으로 고생하신 정석 Eng. 전형한 사장님이 그리울 것이라는 생각이 듭니다. 짧은 시간 동안 깊은 우정을 나누고 인도로 돌아간 Khanra 박사님, Sayak, 호주에서 포닥하고 있는 Nam 박사님, 저에게 많은 힘과 용기 그리고 도움을 주었으며, 이에 깊은 감사를 드립니다. 연구실의 믿음직한 후배 그리고 선배가 되기를 약속하며, 아울러 후배들의 건투를 충심으로 빕니다. 아울러 저의 학위논문 실험을 위해 많은 도움을 주신 순천대학교의 박용범 교수님, 정병조 박사님, 명재형, 기홍이, 태양이, 재료분석센터 박주철 센터장님, 이기라 선생님, 이태우 선생님, 김은식 선생님, 문영신 선생님, 김보경 선생님, 김효선 선생님, In-situ TEM 분석을 위해 귀한 시간을 내어준 승표형, 연구관련 많은 조언을 해준 포공 병찬이형, 연대 종윤이형, 준석이형께 고마운 마음을 전합니다.

오늘의 제가 서기까지는 많은 분들의 후원이 있었습니다. 젊은 청춘을 함께한 중, 고등학교 동기들인 광명, 림연, 익철, 경복, 대욱, 송민, 령미, 영걸, 덕은, 그리고 대학 동기이며 함께 한국으로 유학 온 원룡, 영훈, 병춘, 창익, 명선에게 늘 행운이 가득하기를 기원합니다. 함께 삶을 나누고 기도로써 동역해준 사랑의 교회 중국어 예배 류영준 담임목사님, 이혜란사모님, 김경원 전도사님, 주영전도사님, 해림전도사님, 정용호 집사님, 정혜경 집사님, 이설형,

미화누나, 금화누나, 명화누나, 철환이형, 미화누나, 학철이형, 권란누나, 창후형, 해화누나, 요한이형, 민경누나, 경주누나, 신애누나, 현철이, 애련누나, 병호형, 은화누나, 혜자누나, 광철이형, 사화누나, 임림누나, 장엽형, 준명이형, 장영누나, 안나누나, 유연, 손뢰, 정령, 서만, 영숙, 려홍, 소아, 당문, 해연, 련홍, 소뢰 그리고 우리 다락방 리더로 섬기고 있는 금란이를 주축으로 유희선권사님, 심석진집사님, 미라누나, 정하누나, 영금, 푸홍, 영매, 아려, 향란에게 감사의 인사를 전합니다. 또한 기도로서 후원해준 연길교회 윤선생님, 아쉬레 지체 학민형, 성홍누나, 오철이형, 련희누나, 준동이형, 진숙누나, 철봉이형, 용진이형, 연희누나, 군화누나, 류옥, 심매, 학권이에게 감사의 말을 전하고 싶습니다.

아울러 물심양면으로 보살펴 주신 큰 이모, 작은 이모, 이모부, 작은 삼촌, 삼촌 어머니, 남길이형, 길화누나, 길순누나, 매형, 철화형, 철주형, 동철이형, 옥련누나에게 감사의 마음을 전합니다. 무엇보다도 소중한 가족들의 사랑과 믿음 그리고 격려가 없었다면, 오늘 이러한 결과는 결코 있을 수 없었을 것입니다. 한없는 사랑으로 저를 길러주시고, 어려운 형편에서도 자식을 믿고 묵묵히 지켜봐 주시고, 삶의 본을 보이신 부모님께 깊은 감사를 드리며, 동생 경철이에게도 자랑스런 형이 되기를 약속합니다. 마지막으로 학위과정 중에 저를 만나 많은 어려움이 있음에도 불구하고 무엇보다도 늘 곁에서 기다려주고 믿어줄 영원한 나의 후원자인 추나에게 진심어린 감사와 사랑의 마음을 담아 전하면서 감사의 글을 맺습니다.

2013년 2월 관악에서

边 明 哲